An observational analysis of the solar chromospheric continuum intensity

Candidatus Scientiarum Thesis

Niklas Karlsen
Institute of Theoretical Astrophysics
University of Oslo

January 2003

Acknowledgements

I would like to give my sincerest gratitude to my adviser, Mats Carlsson, for his help during the work on this thesis. He has given me direction and advice (and laughs), which has made these two years enjoyable.

I also wish to mention my friends at the institute (ITA) and my brothers and sisters at RG, which have enriched my studies with friendship and support.

Finally, my thanks go out to you my Lord, Jesus Christ, for bringing me through these years and still letting me stand in your grace.

Oslo, winter 2003.
KNK

Contents

List of Figures

List of Tables

Chapter 1

Introduction

[. . .] In them hath he set a tabernacle for the sun, Which is as a bridegroom coming out of his chamber, and rejoiceth as a strong man to run a race. His going forth is from the end of the heaven, and his circuit unto the ends of it: and there is nothing hid from the heat thereof.

The Book of Psalms 19,4-6

In this chapter I will describe the structure of the sun, and put special emphasis on the atmosphere, which is what this thesis is about. I will go into the chromosphere of the sun, and tell what makes it so special, compared to the other parts of the atmosphere of the sun. At the end of the chapter I will describe the purpose of this thesis.

1.1 The structure of the sun

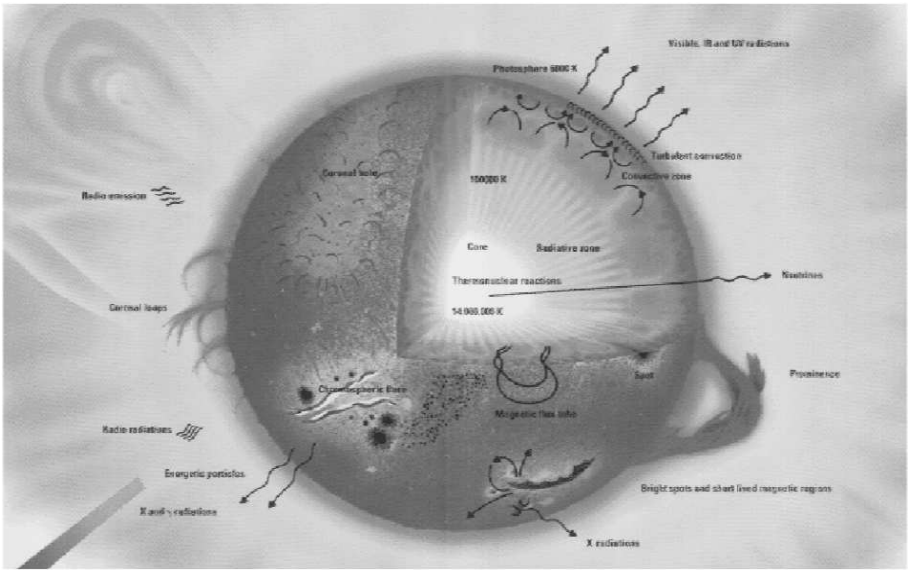

Figure 1.1: **Solar structure** The figure shows the structure of the sun. At the center is the core, where thermonuclear reactions take place. Outside the core, is the radiative zone, where the energy generated in the core is transported outwards. We then reach the convective zone, just below the surface. Then we pass the surface, and enter the photosphere. Not shown clearly in this figure, is the chromosphere, which is the gray haze above the surface. The outer parts of the atmosphere, which are almost invisible, are called the corona. The figure is taken from http://solar.physics.montana.edu/YPOP/Spotlight/SunInfo/Structure.html

1.1.1 The inner structure of the sun

In figure 1.1, is a sketch of the structure of the sun. If we begin at the center of the sun we see the core. This is a densely packed region of hydrogen and helium. The entire weight of the sun is attracted towards the core, which makes the temperature in the core reach over 14 000 000 K, enough to start fusion reactions. The fusion reactions convert hydrogen nuclei into helium nuclei, and in the process release

the equivalent of 8×10^{19} five MW nuclear power plants, which are radiated away, through what is shown as the radiative zone in the figure. In the radiative zone the temperature is about half of the core temperature, and the radiation may take over 170 000 years (ypop@mithra.physics.montana.edu 2002) to pass through this region. The radiative zone extends to about $0.8R_\odot$[1], where we enter the convective zone. The temperature is now so low, about 50 000 K, that the energy transfer is in the form of convection. Convection occurs when hot masses rise and cools down as it approaches the surface, the cool masses then sink and gets warmed up and rises again, like we see in a boiling pot of water. It is thought that the magnetic field of the sun is generated at the bottom of this region. This is roughly the inner structure of the sun. We now enter the atmosphere of the sun.

1.1.2 The outer structure of the sun

The first part we see of the sun, when looking at it in visible light, is the photosphere, "the visible sphere". This is what we define as the surface of the sun. The photosphere has a temperature of about 5800 K, which is why it radiates the most energy in the visible part of the spectrum. Another way of identifying where the photosphere is situated in the atmosphere, is by using the temperature stratification of the atmosphere of the sun. In figure 1.2 I have shown the VAL3C model of the atmosphere of the sun. The conventional wisdom described the structure of the atmosphere according to the VAL3C model. The photosphere can be seen as the temperature decline at the right of the figure, from about 0-500 km of height.

Above the photosphere is the chromosphere. This is a really interesting part of the atmosphere of the sun, and it is the focus of this thesis. From the figure we see that it extends from about 500 km up to about 2000 km. Through this stretch the atmosphere starts out as being opaque, which is why we do not see through the photosphere, i.e. no light reaches us from below the photosphere, this is the reason we must use helioseismology to probe the depths of the sun; the atmosphere then becomes less opaque as we move outwards from the photosphere through the chromosphere and into the corona, which is transparent. It is hard to see the corona, because of the glare from the rest of the sun. This is also the reason why occultations of the sun, which block the bright light of the sun, make it possible to see the corona.

But back to the chromosphere. The opacity in the chromosphere therefore is intermediate. This makes it hard to infer from the light we observe in the chromosphere, what history the light have. We can not say with certainty, how the light we observe has been created. I will go deeper into the causes behind this in the next chapter. Another thing which makes the chromosphere so exciting, is the role of the magnetic field. The dynamics of the atmosphere is dominated by gas dynamics in the photosphere. This is because the atmosphere is very dense, and the convection just below releases all the energy created in the core, which needs to be transported

[1] $R_\odot$ = solar radii

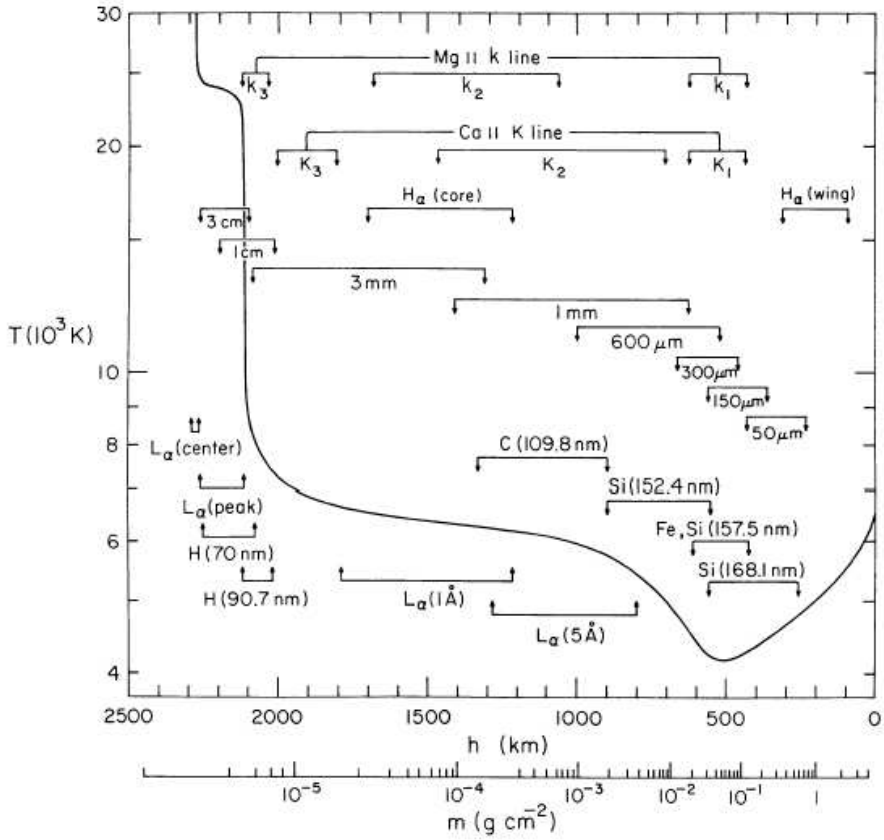

Figure 1.2: **The standard quiet sun atmosphere temperature stratification**. Derived from the EUV continuum, the Lα line and other observations. The approximate depths where the various continua and lines originate are indicated. The chromosphere start at temperature minimum (about 500km), and end at about 2000km of height. (Vernazza et al. 1981)

through this dense region. But as we go further out into the atmosphere, the density decreases and the magnetic field begins to dominate the dynamics. When we reach the corona, the magnetic field is by far the most dominant factor in the dynamics of the atmosphere. And again, the transition from gas dominated dynamics to magnetically dominated dynamics happens in the chromosphere. This intermediate case is also difficult to describe physically, which is why most solar physics people work either with corona physics or in helioseismology. But we dare to enter the unknown.

I will now continue the description of the atmosphere of the sun. We have reached about 2000 km, and if you look at figure 1.2, you can see that we have now reached a high temperature gradient. The temperature actually goes from about 50 000 K to about 1 000 000 K over a very short height range. This region is

the transition region. If you refer back to figure 1.1, you will see some of what is going on in this part of the atmosphere.

Finally, there's the corona. The corona is a very hot, but not very dense, region which extends into space. The temperature is over a 1 000 000 K. The dynamics are dominated by the magnetic fields, because the magnetic pressure is much higher than the gas pressure.

1.2 The purpose of this thesis

We have now roughly seen how the structure of the sun is described. I have also indicated some elements which make the chromosphere an interesting and challenging part of the sun to study. I will now give you some of the background for the specifics of this thesis.

The idea for this paper came from some observations of numerical simulations done by Mats Carlsson. The simulations calculated the conditions in the atmosphere of the sun, or more specifically the chromosphere. The results from the simulations showed good correlation with actual observations done with SUMER, but indicated that an offset of the average intensity was needed for a perfect match. The idea was that a temperature increase could be supplied by the magnetic field in a two component model, where the oscillations are provided by the photospheric motions, and the basic temperature was set by the magnetic field. As the results in this thesis show, this hypotheses does not seem to be entirely correct.

I will now give a brief outline of this thesis. All the information I have used in this thesis, was created at one point by the atmosphere of the sun. To give a deeper understanding of how the radiation we observe was created and how observations of the continuum radiation can be used to diagnose the solar plasma, I have written a chapter about the solar continuum, chapter 2. The radiation coming from the sun was recorded by SUMER and MDI, two instruments on board the SOHO spacecraft. In chapter 3, I have described these instruments and the data they have recorded. The chapter also gives a thorough description of how I analysed the observational data. Chapter 4 presents the results of the analysis. It shows the continuum radiation and its connection with the magnetic field, which is the central purpose of this thesis. I then go on to discuss the results in chapter 5, where I also give the conclusion.

Chapter 2

The solar continuum

Apply thine heart unto instruction, and thine ears to the words of knowledge.

The Proverbs 23,12

The continuum radiation is what we measure with our instruments at earth orbit, but what can it tell us about the physics of the chromosphere, where it comes from? In this chapter I will describe the continuum processes that create this radiation, and I will describe how we understand radiation and its transport through an atmosphere. This chapter roughly follows Rutten (1991 and 2000).

2.1 The solar continuum processes

The solar continuum is a result of continuum processes that take place in the solar atmosphere. The observations I use are in the ultraviolet range, which therefore are of most interest to us. See for example figure 2.1 for details of the solar extreme UV continuum as observed by SUMER. The elements that are important in the ultraviolet spectrum formation, are Al, Mg, Si, C and Fe. In the far UV the spectrum is dominated by the H and He I Lyman continua (chapter 8.2 ,Rutten 1992). The basic processes that create the solar spectrum are:

- free-free transitions. These are electrons which interact with the electric field of a nucleus. This causes the electrons to accelerate and emit electromagnetic radiation, so-called *bremsstrahlung*. This radiation dominates the infrared and longer wavelengths (mm to m).
- bound-free transitions. This happens in three ways.
    1. Either a photon knocks the electron free from its orbit around the nucleus (photoionization).
    2. Or a free electron can be caught by a nucleus (spontaneous photorecombination), which then sends out a photon.
    3. A free electron interacts with a passing photon. Because of this disturbance, the electron may be caught by a nucleus and emit a photon with the same wavelength as the initial photon (induced photorecombination).
- cyclotron radiation, synchrotron radiation, plasma radiation. These are caused by interactions with the magnetic field of the sun. Contributes only to the far ends of the spectrum.
- Thomson scattering. These are collisions between free electrons and photons. It causes the solar K corona.
- Rayleigh scattering. This happens when an electron interacts with EM-radiation of a very long wavelength (relative to the electrons resonance frequency), almost like a boat bobbing on top of waves in the ocean. Important in sunspot umbrae which are cool enough to contain many molecules. Also appreciable in the near ultraviolet, especially in cool components of the chromosphere where hydrogen is not ionised.

- line haze. Lines are formally not a source of continuum extinction/emission, but in practice they represent one in the solar violet and ultraviolet, where the line haze is so crowded that it acts as quasi-continuous extinction.

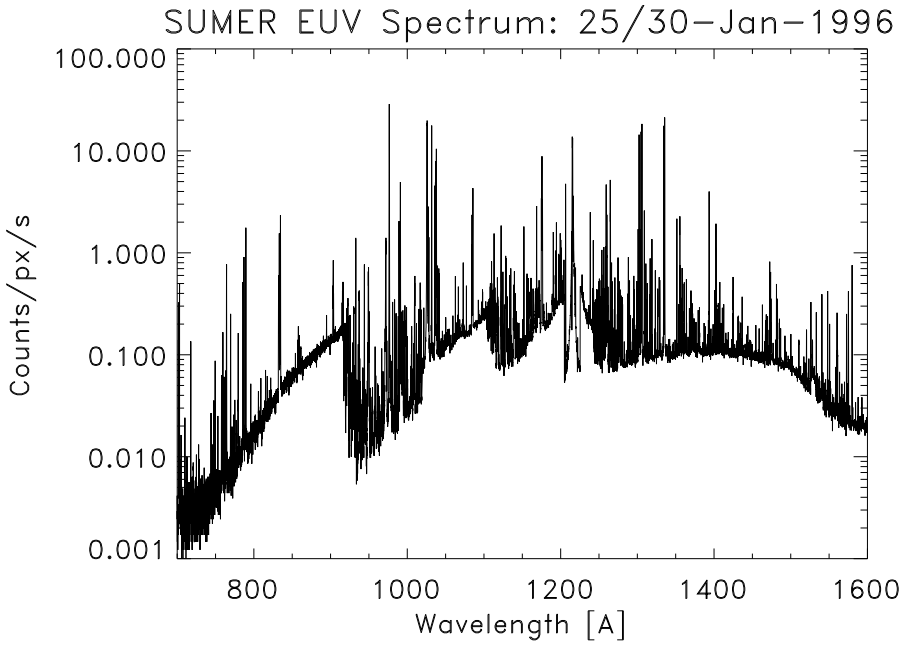

Figure 2.1: The Solar EUV Spectrum (790 - 1600 Å) from SUMER The figure shows the number of photons observed at different wavelengths in the EUV. (Brekke 2002)

2.2 Radiative transport

In the previous section, I described several reactions between electrons, nuclei and photons, which create the solar continuum. That was a very low level description of the underlying physics. In this chapter I am going to do a more statistical approach. By using the equations of radiative transfer and the laws of thermodynamical equilibrium (TE), we can describe how the emitted radiation will look. When we interpret the observations, we of course go the other way round, we describe why the observed intensity looks like it does. See figure 3.1 for an example of how the observed intensity may look. The scrabbled areas in the figure are the continuum intensity.

2.2.1 The equations of radiative transfer

In section 2.2.3 I will describe different kinds of equilibrium, which represent the state of the atmosphere where the radiation was emitted. Together with the equations of radiative transfer and the equations of thermodynamical equilibrium in section 2.2.2, we will then be able to understand the physics of radiative transport.

The optical path length

We begin by considering the distance the photons have travelled, since their creation. This measure is called the optical path length:

$$d\tau_\nu(s) = \alpha_\nu(s)ds$$

where ν is the frequency of the photon, α is the extinction coefficient and ds is the thickness of the slab, which the photon pass through.

The source function

The source function is a measure of how much radiation is emitted and how much is extincted, through the processes given in the previous section. The source function is:

$$S_\nu = \frac{j_\nu}{\alpha_\nu}$$

where j_ν is the emission coefficient and α_ν is the extinction coefficient.

The equation of radiative transport

The source function is useful to get the equation of radiative transport:

$$\frac{dI_\nu}{d\tau_\nu} = S_\nu - I_\nu$$

where I_ν is the intensity we observe. This equation describes how the intensity change when it interacts with a medium. The interaction is of the form described in section 2.1. The transport equation is essential to understand how the radiation we see has been changed by local conditions.

2.2.2 The equations of thermodynamical equilibrium

The Planck function

The Planck function describes how a blackbody radiates at different wavelengths, when it has a given temperature. Often we assume thermodynamical equilibrium (section 2.2.3). This means that the source function equals the Planck function. The Planck function is:

$$B_\nu(T) = \frac{2h\nu^3}{c^2}\frac{1}{e^{\frac{h\nu}{kT}} - 1} \tag{2.1}$$

where T is the temperature, h is the Planck constant, c is the speed of light, k is the Boltzmann constant and ν is the frequency of the observed light.

When we later on talk about the radiation temperature, we mean the temperature we use in the Planck function to get the observed intensity.

Distribution laws

To describe the velocity distribution of matter, we use the Maxwellian velocity distribution. For each component of the velocity:

$$\frac{n(v_x)}{N}dv_x = \Big(\frac{m}{2\pi kT}\Big)^{1/2} e^{-(1/2)mv_x^2/kT} dv_x$$

and for the speed:

$$\frac{n(v)}{N}dv = \Big(\frac{m}{2\pi kT}\Big)^{3/2} 4\pi v^2 e^{-(1/2)mv^2/kT} dv$$

where $n(v_x)$ is the number of particles with a velocity-component in the x direction per unit volume, $n(v)$ is the number of particles with the speed v per unit volume, N is the total number of particles of this type per unit volume and m is the mass per particle.

To describe how many atoms are in a given excitation level we use the Boltzmann law:

$$\Big[\frac{n_{r,s}}{n_{r,t}}\Big]^{TE} = \frac{g_{r,s}}{g_{r,t}} e^{-(\chi_{r,s}-\chi_{r,t})/kT}$$

where $n_{r,s}$ is the number of atoms per cm^3 in level s of ionization state r, $g_{r,s}$ is the statistical weight of level s of ionization state r, $\chi_{r,s}$ is the excitation energy of level s of ionization state r, measured from the ground state $(r, 0)$. Thus $\chi_{r,s} = E_{r,s} - E_{r,0}$, and $\chi_{r,s} - \chi_{r,t} = h\nu$ for a radiative transition between states (r, s) and (r, t) with the level s "higher" (has more internal energy) than level t.

For the similar case, but in ionization, we use the Saha law. Shown are only the version for the ground level:

$$\Big[\frac{n_{r+1,0}}{n_{r,0}}\Big]^{TE} N_e = \frac{2g_{r+1,0}}{g_{r,0}} \Big(\frac{2\pi m_e kT}{h^2}\Big)^{3/2} e^{-\chi_r/kT}$$

where N_e is the electron density and m_e the electron mass, $n_{r+1,0}$ and $n_{r,0}$ are the populations of the ground states of two adjacent ionization levels, $g_{r+1,0}$ and $g_{r,0}$ are their statistical weights, and χ_r the ionization energy of level r, i.e. the minimal energy necessary to remove an electron from an atom in state $(r, 0)$. The factor 2 for the statistical weight $g_{r+1,0}$ is the statistical weight of the freed electron; each has $g_e = 2$ on account of two possible orientations of its spin.

Together, they describe the populations of any element, and are called the Saha-Boltzmann distribution.

2.2.3 Types of equilibrium

To solve the equations of radiative transfer, we often assume that some conditions are fulfilled. The typical assumption is some kind of equilibrium. This is necessary to be able to calculate the equations either by hand or numerically.

TE

The simplest kind of equilibrium is thermodynamical equilibrium (TE). The source function then equals the Planck function. The populations are given by the Saha-Boltzmann distribution and the kinetic energy distribution follows the Maxwell law, with the same temperature in all distribution laws. There is "detailed balancing" between each process and its opposite, at each frequency and for each bundle.

Since it is "detailed balancing", which means that any photons created are later absorbed and do not reach our detectors, i.e. we do not observe anything(!), this approximation is not very helpful when doing real astrophysics, which means we will have a hard time evaluating energy fluxes and interpret spectral lines. We therefore often use the concept of local thermodynamical equilibrium (LTE).

LTE

The assumption is that the matter is in equilibrium with the ambient kinetic temperature, but the radiation may deviate from the temperature, or vary slowly through the medium. The essence of LTE is that the energy distribution of matter is more locally determined and maintained by collisions than that of radiation, so that the radiation but not the matter can depart greatly from the local conditions.

LTE is helpful only in the most simple cases, like the treatment of a single spectral line without being concerned with other transitions and wavelength regions. When these assumptions do not hold, we need to assume statistical equilibrium (SE).

SE and NLTE

The assumption is that the transitions in and out of different levels in an element is static over time. The averaged state is unaltered, but the microstate are unknown. The result is a system of nonlinear coupled equations, often quite large, that must be simultaneously solved for each place in the medium, for all frequencies and along all bundles that participate in the population process. This is often also called NLTE or non-LTE, that is the assumption of LTE is not valid. One also assumes that the Maxwell distribution holds and that complete redistribution (CRD) occurs. Then the populations can differ from the local Saha-Boltzmann values. What this ends up in, is that the source function can differ from the local Planck function, which is the case when we consider the chromosphere. See for example Carlsson (1986) for a numerical treatment of the NLTE case in a moving or static atmosphere.

Chapter 3

Observations and analysis

But the God of all grace [. . .] after that ye have suffered a while, make you perfect, stablish, strengthen, settle you.

The First General Epistle of Peter 5,10

This chapter describes the instruments that have been used to collect the data. It then lists all datasets and observables. I end the chapter by describing the methods I have used to analyse the data.

3.1 Observations

The observations were taken with the SUMER[1] and MDI[2] instrument on board the SOHO[3] spacecraft. SOHO observes the sun continuously in a halo orbit around the L1 Lagrangian point. It was launched on the 2nd of December 1995. The observables are listed in table 3.1.

3.1.1 SUMER

The SUMER (Wilhelm et al. 1995) instrument was used to observe the continuum intensity at 1319Å, 1199Å, 1037Å and 910Å.

The SUMER website gives the following description of the SUMER objectives:

> "The SUMER experiment is designed for the investigation of plasma flow characteristics, turbulence and wave motions; plasma densities and temperatures; structures and events associated with solar magnetic activity in the chromosphere, the transition zone and the corona. Specifically, SUMER will measure profiles and intensities of extreme ultraviolet (EUV) lines emitted in the solar atmosphere ranging from the upper chromosphere to the lower corona; determine line broadenings, spectral positions and Doppler shifts with high precision and accuracy; provide stigmatic images of selected areas of the Sun in the EUV with high spatial, temporal and spectral resolution and obtain full images of the Sun and the inner corona in selectable EUV lines, corresponding to a temperature range from 10 000 to 2 000 000 K." (Dammasch 2001)

The specifications of the instrument are:

> "The SUMER instrument is a normal incidence stigmatic spectrograph. The diffracted light is recorded by a micro channel plate detector of size 1024×360 pixels. The spatial resolution is $1'' \times 2''$ ($1''$ slit width, $1''$ sampling along the slit). The spectral resolution is about 40 mÅ in first order and 20 mÅ in second order." (Carlsson 1999)

[1] Solar Ultraviolet Measurements of Emitted Radiation

[2] Michelson Doppler Imager

[3] Solar and Heliospheric Observatory, *"SOHO is designed to study the internal structure of the Sun, its extensive outer atmosphere and the origin of the solar wind, the stream of highly ionized gas that blows continuously outward through the Solar System"*

3.1.2 MDI

The MDI instrument was used to observe the photospheric line of sight magnetic field and doppler velocity.

The MDI instrument is described at the SOI[4] (Scherrer et al. 1995) website:

> "SOI and the MDI Team form an international collaboration to study the interior structure and dynamics of the Sun. The primary objective of the SOI investigation is to investigate the solar interior using the tools of helioseismology.
>
> [The] observations were taken using the high-resolution mode, which is a focused image of an 11 arcmin square field of the Sun with a plate scale of 0.625 arcsec per pixel and a (diffraction-limited) resolution of 1.25 arcsec." (jeneen@quiver.stanford.edu 2001)

3.1.3 Datasets

I obtained the datasets in the following manner; first all SUMER observations 1996-2002 were searched for timeseries using the following three criteria: did they have simultaneous MDI observations, rasters[5] and decent count rates, i.e. good signal-to-noise ratio?

The data extracted from the timeseries are listed in table 3.1. The selected timeseries are listed in table 3.2.

Observable	Instrument	FOV ($x \times y$)	PX ($''$)	Cad. (s)	Reg./Hgt. (Mm)	Diagnostic of ...
$B_{\|\|}$ (gauss)	MDI	420×420	0.6	60	Ph/0.2	LOS mag field
$V_{\|\|}$ (m/s)	MDI	420×420	0.6	60	Ph/0.2	LOS velocity
1319Å κ	SUMER	$0.3 - 1 \times 120 - 300$	1	20-30	Ch/0.7	Ch dynamics
1199Å κ	SUMER	$0.3 - 1 \times 120$	1	20-22	Ch/0.7-1.2	Ch dynamics
1037Å κ	SUMER	1×300	1	15	Ch/0.9-1.4	Ch dynamics
910Å κ	SUMER	1×120	1	20-22	Ch/1.8	Ch dynamics

Table 3.1: **Overview of timeseries data.** FOV is the field of view in arcseconds, i.e. size of the area observed. PX is the pixel size of the instrument detector ($1''$ corresponds to 0.725Mm on the Sun). Cad(ence) is the time between consecutive exposures. Reg./Hgt. (Region/height) is the region of the atmosphere we observe together with the approximate height of formation for the given observable. The height is estimated from $\tau_{5000} = 1$. Notation: $B_{\|}$ = LOS magnetic field strength; $V_{\|}$ = LOS doppler velocity; κ = continuum; LOS = line of sight; Ph = photosphere; Ch = chromosphere.

[4] Solar Oscillations Investigation

[5] "images" made by stepping the SUMER slit. The rasters are used to align the SUMER observations with the MDI observations

Wavelength (Å)	Slit	Date (1996)	Start Time (UT)	Exposure (s)	TSD (min)	Pointing	Rotcmp
	1.0×300	30 Jul (B)	17:05:30	30.0	125	(29,5)	No
	1.0×300	30 Jul (D)	22:47:44	30.0	125	(86,3)	No
	1.0×300	31 Jul (B)	17:05:35	30.0	125	(30,2)	No
1319 κ	1.0×300	31 Jul (D)	22:47:51	30.0	92	(83,0)	No
	0.3×120	10 Sep (A)	17:14:59	22.0	59	(-6,-4)	No
	1.0×120	02 Oct (B)	17:19:36	20.0	74	(-27,2)	Yes
	1.0×120	04 Oct (A)	20:25:23	20.0	71	(19,-9)	Yes
	1.0×120	10 Sep (C)	22:20:40	22.0	59	(-6,-2)	No
1199 κ	1.0×120	02 Oct (A)	03:36:58	20.0	71	(-4,8)	Yes
	0.3×120	04 Oct (B)	22:01:16	20.0	119	(37,-4)	Yes
	1.0×300	30 Jul (C)	19:43:20	15.0	150	(54,1)	No
1037 κ	1.0×300	31 Jul (A)	14:01:10	15.0	150	(8,-5)	No
	1.0×300	31 Jul (C)	19:43:24	15.0	150	(54,-1)	No
	1.0×120	10 Sep (B)	19:48:20	22.0	59	(-4,-12)	No
910 κ	1.0×120	02 Oct (C)	19:27:09	20.0	66	(-21,0)	Yes
	1.0×120	05 Oct (A)	00:22:55	20.0	69	(35,-17)	Yes

Table 3.2: **Details of SUMER observations.** Wavelength is the wavelength in Ångström of the continuum κ. Slit is the size of the slit in arcseconds. Date is the observation date of the timeseries. The alphabetical indexing is used to separate datasets taken the same day. Start time is the start of the observation run in universal time (UT). Exposure is the duration of an exposure. TSD is the time series duration. Pointing is the approximate position of the center of the SUMER slit relative to Sun center in arcseconds (as seen from SOHO in nominal attitude, north at the top) (if rotcmp is on, the solar rotation has been added to give the position at t = TSD/2). Rotcmp tells whether compensation for solar rotation was used or not.

An evaluation of the datasets

In this section, I wish to address some issues which I faced when dealing with the datasets.

Most of the work I have done, was concerned with the 1319Å datasets. Later on, when we felt confident that our routines were stable enough, we extended the analysis to the rest of the wavelengths (1199, 1037 and 910Å). Accordingly, most of our focus in this thesis, has been on the 1319Å continuum.

The datasets were taken from three months: July, September and October. Only the October datasets have rotation compensation on the SUMER data. Only the July datasets use slits with a width of 300″. Sadly, we could not use the entire slit in the July datasets, since we wished to compare the SUMER data with the MDI data. The overlapping region between the data from the two instruments is about 130″ wide. Accordingly, all datasets have slitwidths of about 120-130″.

Some of the MDI data from July, have large gaps of missing data, cf. the black

bands in the July figures in section 4.1.1. On the other hand, the July data also have the longest timeseries. Due to the combination of missing rotation compensation and lacking MDI data, I consider the July data to be less than optimal.

The September datasets are the ones with the least obvious problems. They all have overlapping regions with SUMER and MDI, no missing MDI data and reasonably sized timeseries (in time and space). Only one of the datasets, 10 Sep A, has a narrow slit ($0.3''$), which results in a low signal-to-noise ratio. Generally, the September datasets are rather nice.

The October datasets suffered somewhat from the problems encountered with the SUMER stepping mechanism. This led to large deviations in the coordinates returned by the instrument. Fortunately, due to the copointing method we devised, we are able to circumvent this problem, and achieve good alignment with the SUMER and MDI datasets. (There are for example some rasters which are stretched, this is obvious when blinking the MDI magnetograms against the SUMER rasters.) Since the October data also have rotation compensation, I consider the October data to be the best datasets I have worked with on this thesis.

3.2 Data analysis

This section describes how I got the results in chapter 4. A short summary; First I find which SUMER data contain observations of the selected wavelengths, and have simultaneous MDI observations. Then I reduce the SUMER data. The reduced data is then used to coalign the SUMER and MDI observations. The MDI data is also averaged to get a better signal-to-noise ratio. Then a magnetic field extrapolation is made to get an idea of the magnetic field configuration. Finally, I make an analysis of the data, which involves plotting the timeseries and corresponding scattergrams. The programs which were developed for the analysis are available at Karlsen (2003).

3.2.1 Selecting the datasets

I have selected four wavelengths to study; they are listed in table 3.1 under observables. The SUMER data is stored in the FITS[6]-format, which have headers with information on the contents of the files. The header information was extracted and I then searched them for observations at the selected wavelengths. Additional criteria in the search were a photon count of at least 2 per second.

Since I intend to also use MDI observations, I needed to verify that the selected datasets had simultaneous MDI observations. The existence of magnetograms (and dopplergrams) were checked at Bogart (2002), the SOI data central, and downloaded. The MDI observations were to be coaligned with the SUMER observations, so SUMER also had to have rasters[7]. I therefore searched the extracted

[6] Flexible Image Transport System

[7] Images obtained by stepping the slit

FITS-data for datasets which seemed to have rasters, and then verified by looking at the solar x-coordinates of the SUMER slit during the timeseries.

The raster search showed that rasters were taken mainly in 1996. This was due to problems with the rastering mechanism which were detected in October of that same year. Therefore, few rasters exist after that date. This is the reason that all datasets selected in this thesis are from 1996.

The chosen datasets are listed in table 3.2.

3.2.2 Reducing the SUMER data

When the SUMER instrument observes the chromosphere, the observations become tainted because of varying sensitivities in the detector. To remove, or at least reduce as much as possible the influence from the instrument on the observations, the data is processed with reduction software. The tools used to reduce the SUMER data, are from the SUMER reduction package available at Carlsson (2002). See also Carlsson (1999) for an overview of the artifacts introduced into the data by the SUMER instrument.

The reduction steps are as follows (see also Carlsson (2002)):

1. get the FITS files containing the observations
2. make an index of the FITS files
3. link the FITS files into a working directory
4. make index of the files in your working directory
5. concatenate data of the same item, item being one of the following:
    - 0. raster region
    - 1. full detector exposure
    - 2. time sequence with fixed slit
    - 3. full detector exposure
    - 4. raster region
6. flat-field the data
7. perform geometric correction

The flat fielding is done with options, “nearest” and /shift_obs (Carlsson et al. 1997). The shift_obs option is intended to align the flat field with the data, since flat fields are taken about once a month to not saturate the instrument, and may not coalign with the data from the observations due to the detector “walking”. If the shift is greater than 3 pixels, then option /shift_obs is not used. Finally, I select the continuum and line windows, which are used by other SUMER procedures later on. Line identification was made using the SUMER red book. See figure 3.1 for an example of an observation set by SUMER.

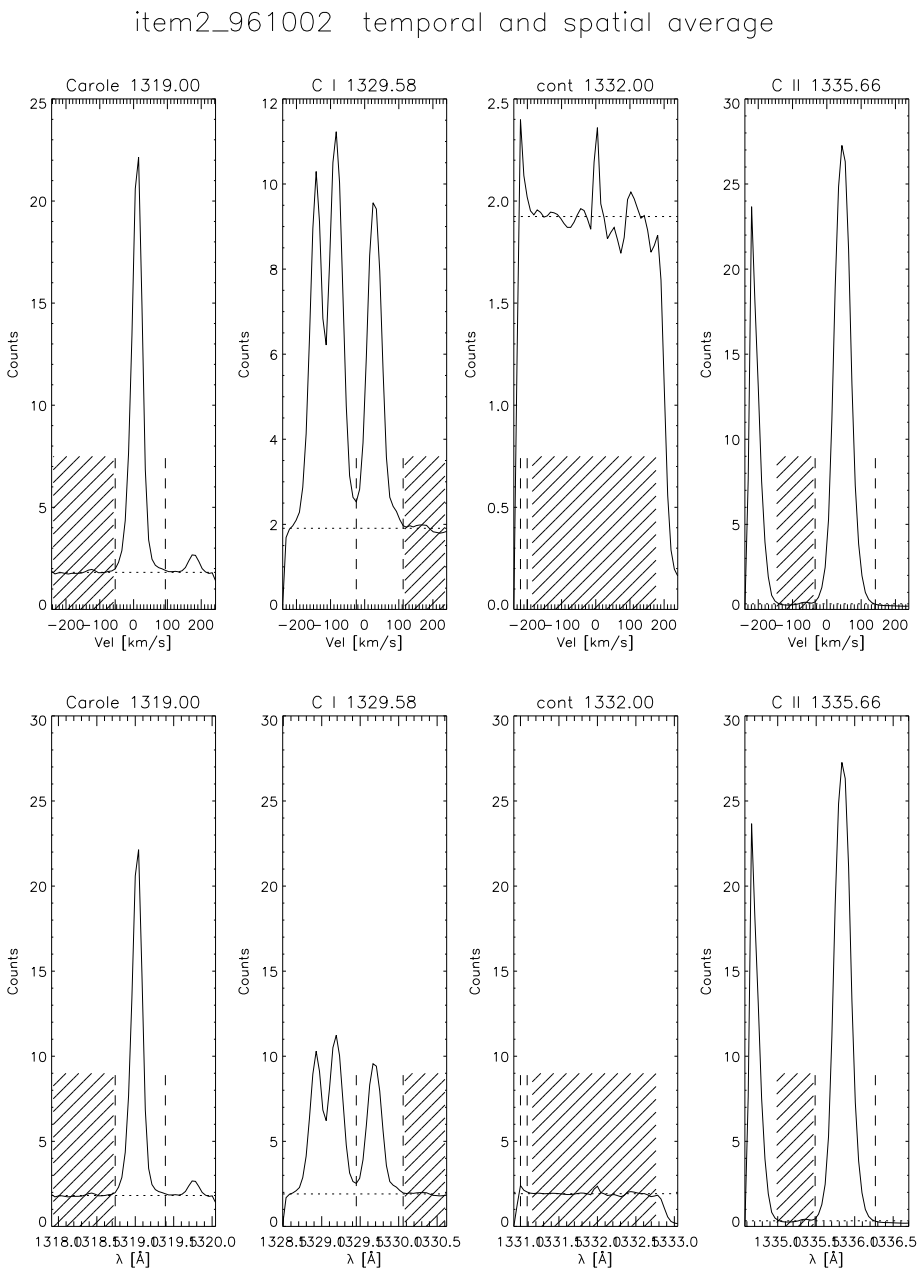

Figure 3.1: **Line profiles for 02 Oct (B).** The dashed lines show the selected line, and the scrabbled area shows the selected continuum. The upper panels shows the photon count for each line with relative axis and doppler shift along the x-axis. The lower panels shows the photon count with absolute axis for comparison, and wavelength along the x-axis. The title of each panel shows the element and wavelength of that particular line. Carole designates an unknown element, investigated by Carole Jordan.

3.2.3 Aligning the SUMER and MDI instruments

To compare the SUMER and MDI datasets, they need to be aligned, i.e. have a common origo. I chose the MDI coordinates as the reference coordinate system. The copointing is done by comparing two sub images of the SUMER and MDI data, and aligning them, as shown in figure 3.2. The resulting alignment coordinates are shown in table 3.3 (given with corrections to the SUMER coordinates).

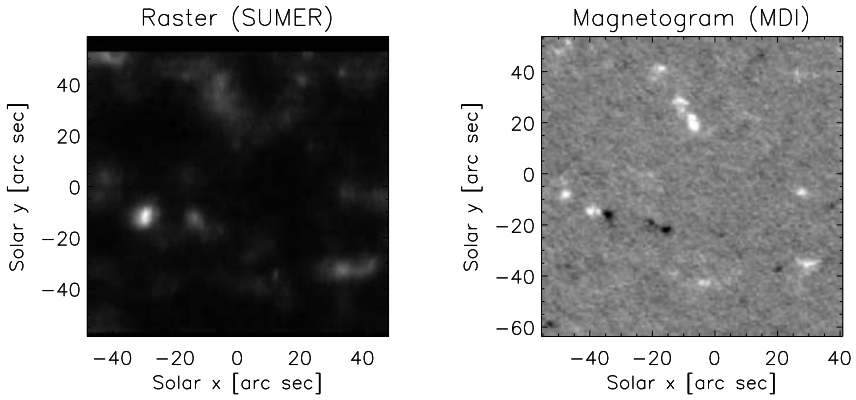

Figure 3.2: **SUMER and MDI copointing.** The figure to the left is a raster obtained at λ1319Å with SUMER. The figure to the right is a magnetogram from MDI of the same region and time. Such images are used to coalign the SUMER and MDI data. This dataset is 10 Sep (B).

Some remarks on the coalignment

This section describes the difficulties with coaligning the two instruments.

The initial guess of the shift was made based on a correlation function in Fourier space, see e.g. Gonzalez & Woods (1993). This gave an acceptable correlation, but manual corrections were necessary to achieve very good correlation.

A note about the precision of the coalignment. The automatic correlation function could give a good match, but was biased towards very bright features. This could sometimes give a shift of an arcsecond or so relative to the optimal coordinate shift. With manual alignment I could consider all the features of the data, including weak features and correct for loops where the intensity in SUMER was brightest, between for example two magnetic areas of opposite polarity.

In the July data the rasters were 300″ tall, which made it hard to coalign with the MDI images, which were under half of that in height. The two sub images overlapped only over about 100” in height. Probably because of this the coalignment of the rest of the image had deviations of up to 4”. I therefore chose to align with features at the origo of the MDI magnetograms.

Date (1996)	SUMER and MDI copointing			Timeseries (± 0.7)	Relative shift of SUMER origo
	Pre-raster (± 0.7)	Post-raster (± 0.7)	Mean		
30 Jul (B)	(0.5, 5.9)	(1.3, 5.6)	(0.9± 1.1, 5.7± 1.0)	(0.9, 8.2)	(0.9± 1.2, 5.7± 1.6)
30 Jul (C)	(0.3, 6.6)	(1.0, -2.8)	(0.7± 1.1, 1.9± 4.8)	(0.7, 1.9)	(0.7± 1.2, 1.9± 3.0)
30 Jul (D)	(2.4, 2.5)	(2.2, 4.0)	(2.3± 1.0, 3.2± 1.3)	(2.3, 5.7)	(2.3± 1.2, 3.2± 1.5)
31 Jul (A)	(N/A)	(2.1, -5.3)	(N/A)	(2.1, -5.3)	(2.1± 1.0, -5.3± 1.0)
31 Jul (B)	(1.2, -0.3)	(1.1, 4.3)	(1.1± 1.0, 2.0± 2.5)	(1.1, 5.0)	(1.1± 1.2, 2.0± 2.1)
31 Jul (C)	(1.1, 5.3)	(0.3, -6.4)	(0.7± 1.1, -0.6± 6.0)	(0.7, -2.6)	(0.7± 1.2, -1.2± 3.7)
31 Jul (D)	(0.0, 0.0)	(N/A)	(N/A)	(0.5, 3.5)	(0.0± 1.0, 0.0± 2.1)
10 Sep (A)	(-5.9, -3.9)	(-7.4, -5.0)	(-6.6± 1.2, -4.5± 1.1)	(-4.6, -4.0)	(-6.6± 1.5, -4.5± 1.2)
10 Sep (B)	(-4.1, -11.8)	(-4.2, -13.6)	(-4.1± 1.0, -12.7± 1.6)	(-4.1, -12.7)	(-4.1± 1.2, -12.7± 1.4)
10 Sep (C)	(-4.1, -2.3)	(-7.1, -2.3)	(-5.6± 2.3, -2.3± 1.0)	(-6.1, -4.3)	(-6.1± 1.6, -2.3± 1.2)
02 Oct (A)	(-3.5, 7.3)	(2.7, 9.1)	(-0.4± 4.5, 8.2± 1.6)	(-2.5, 8.2)	(-2.5± 2.6, 8.2± 1.4)
02 Oct (B)	(-72.5, 2.5)	(-67.8, 2.6)	(-70.1± 3.4, 2.5± 1.0)	(-72.0, 2.5)	(-72.0± 2.2, 2.5± 1.2)
02 Oct (C)	(-86.5, -0.3)	(-87.2, -0.8)	(-86.9± 1.1, -0.6± 1.1)	(-86.9, -0.6)	(-86.9± 1.2, -0.6± 1.2)
04 Oct (A)	(0.0, -8.7)	(19.7, -9.3)	(9.9±13.9, -9.0± 1.1)	(2.0, -9.0)	(2.0± 7.7, -9.0± 1.2)
04 Oct (B)	(12.2, -4.8)	(4.5, -4.0)	(8.4± 5.5, -4.4± 1.2)	(7.0, -4.4)	(7.0± 3.1, -4.4± 1.2)
05 Oct (A)	(-0.6, -17.4)	(-20.6, -16.9)	(-10.6±14.1, -17.1± 1.0)	(-20.6, -17.1)	(-20.6± 8.3, -17.1± 1.2)

Table 3.3: **The displacement of SUMER origo relative to MDI origo.** The SUMER and MDI copointing column shows the coordinates from pre-raster, i.e. before the timeseries, and post-raster, after the timeseries. The timeseries column shows the best fit during the timeseries with figures such as the left side of figure 4.10. The adopted shift in SUMER origo is shown in the final column. It is the (x,y) coordinates used in the data analysis. *A note about the errors: the errors in the SUMER and MDI copointing was estimated visually and set to* $\pm 0.7''$ *for all datasets, the errors in the mean comes from alignment errors and coordinate errors. Timeseries errors are estimated to be equal to the copointing error, but the corresponding coordinates do not give very good agreement with the mean from mdi_copoint. The errors in the relative shift is the summed errors from all the above contributions.*

The SUMER instrument had problems[8] with its rastering mechanism as noted in the previous section. This is probably the cause for the very large deviations ((-60)–(-80)") in the x-coordinates observed on the 2nd of October.

3.2.4 Preparing the MDI data for analysis

Now that I have the coalignment coordinates, I can prepare for the data analysis. First, I want to look at the magnetic field configuration at the position of the SUMER slit. The MDI magnetogram measures the z-component of the magnetic field. To get a better signal-to-noise ratio, i.e. better estimation of the magnetic field at low heights, we average the images to reduce the noise. This is done over an one hour period centred at the slit position halfway through the timeseries. A potential field extrapolation is made to get an approximation of the magnetic field at a given height. The extrapolation procedure is described in McIntosh et al. (2001).

The error introduced by averaging the magnetograms

We wanted to use the MDI magnetograms to extrapolate the magnetic field. We observed that using only a single magnetogram, with a low signal to noise ratio, led to uncertainties in the size and configuration of the magnetic field (at altitudes up to about 0.6Mm). We therefore decided to average several magnetograms, observed over an hour, to improve the signal to noise ratio.

The magnetic field is dynamic, and therefore changes over time. But for our purpose, which is a statistical correlation between the magnetic field and wave propagation in the chromosphere, averaging several magnetograms does not alter the overall pattern. If we were interested in how the changes in the magnetic field, affects the radiation intensities, we would take the time evolution into consideration.

3.2.5 Comparing the SUMER and MDI data

The purpose was to compare the SUMER continuum with the magnetograms *at the SUMER slit*. I have achieved a good enough precision in my coalignment to start this comparison. I use a routine that extracts the magnetic field at the position of the SUMER slit, and creates a timeseries of the magnetograms. I then have two timeseries I can compare, as in figure 4.12.

Aligning to a higher order using the timeseries

I can use the two timeseries to adjust the copointing. The timeseries contain only the (y,t) information, i.e. spatial position along the slit and observing time. But by varying the x-coordinate I can move features in and out of the slit to get the best fit; see for example figure 4.7. This may lead to different coordinates than the

[8] Some screws were to tight

method in section 3.2.3, see table 3.3 for a summary of the coordinates given by both methods. If I insert the coordinates found by the timeseries method into the copoint method, I often get a poor overlap between the sub images. I therefore give most weight to the copoint method, with some corrections given by the timeseries method.

For the October data, with rotation compensation and raster problems (see section 3.2.3), this step is *necessary* due to variations in x of up to $20''$. I then give this method the most weight, when I select the coordinate shifts.

Measuring the correlation between the continuum radiation temperature, magnetic field and intensity oscillations

The next step is to quantify the things we see in figures such as figure 4.7, i.e. the connection between the continuum intensity and the photospheric magnetic field. We want to measure radiation temperature, the strength of the magnetic field and the intensity oscillations. The magnetic field strength is obtained by calculating the mean along each slit position. The intensity oscillations are calculated by taking the standard deviation along each slit position. The time series that do not have rotation compensation, are divided into 20 minute segments. The quantities are labeled as follows:

- $min[T_{rad}]$, this quantity represents the radiation temperature. This quantity is selected to get a sample of the atmosphere as it is unaffected by waves, waves which are typically characterised by short bright increases in radiation temperature. I have median filtered the data and selected the minimum value at each slit position as this quantity.
- $|<B_z>|$, this is the mean magnetic field at each slit position.
- $\sigma[I]$, this is the standard deviation of the continuum intensity at each slit position
- $\frac{\sigma[I]}{<I>}$, this is $\sigma[I]$ divided by the mean intensity at each slit position; this quantity is mostly independent of instrumental factors and can be compared across datasets

Before calculating the values, I filtered the SUMER data with a high pass filter at 4.5mHz. 4.5mHz is the acoustic cutoff frequency, so this should remove any standing waves, i.e. I analyse only the propagating waves. The filtering should also remove any trends introduced by the suns rotation, i.e. as in the data without rotation compensation.

Frequency and coherence

For completeness I have included frequency and coherency analysis. For a description of the method see Lites et al. (1993). I have analysed the coherency between the doppler velocities in the photosphere and the continuum intensity in the

chromosphere. I have also analysed the frequency components of the continuum intensity in the network and internetwork.

Chapter 4

Results

No man, when he hath lighted a candle, covereth it with a vessel, or putteth it under a bed; but setteth it on a candlestick, that they which enter in may see the light. For nothing is secret, that shall not be made manifest; neither any thing hid, that shall not be known and come abroad.

The Gospel According to Saint Luke 8,16f

This chapter begins with a description of the fundamental observational results: the radiation temperature calculated from the observed intensity as a function of position and time, and the magnetic field configuration. An analysis of the correlation between these observables follows, and the chapter ends with an analysis of the correlation between the observed intensity variations and the photospheric velocity field.

4.1 Continuum radiation temperature and magnetic field configuration

This section shows the observational data in timeseries format, along with the results of the magnetic field extrapolation. All datasets are shown in figure 4.2 to figure 4.17. They are sorted on wavelength chronologically. The figures shows one hour segments of the timeseries. They also show the magnetic field directly above the SUMER slit, extracted from the potential field extrapolation, and the photospheric magnetic field in the area around the slit. The radiation temperature range and magnetic field range have been fixed for each wavelength in order to facilitate comparisons within each wavelength. For example in the plots for the 1319Å continuum, the range for the radiation temperature is set to 4200-4800K and the magnetic field strength is from 0-25G. All the figures show approximately the same duration in time ($\sim 3600s$) and width of the slit ($\sim 120''$), so that we can compare the datasets directly by comparing the figures. This means that the scale in the timeseries plots, is the same for all figures also. Note that the spatial positions in the SUMER displays, are numbered from north to south.

4.1.1 Overview of the observations

1319Å

I will now walk you through the datasets[1], beginning at the deepest level in the chromosphere, i.e. the lowest opacity, which is the 1319Å observations. Figure 4.2 shows the first dataset of the analysed timeseries at this wavelength, designated 30 Jul (B). The upper left panel shows the continuum radiation temperature as a function of spatial position and time. The spatial positions are from 60 to about $190''$. I set this width, such that I can compare the observed intensity, with the observations of the magnetic field strength. Notice the grain structure, first noted by Carlsson (1999). These quasi-periodic fluctuations have periods of about 3 minutes, and show an assymetry in their shape, in that they have a steep increase, they get bright fast, and have a long tail, i.e. the intensity decreases slowly. These grains appears in the 1319 and 1199Å observations.

The lower right panel shows the region, which was delimited by the MDI field of view. The dotted lines show the area covered by the SUMER slit during the

[1]The order I present the datasets in, is the same order as in table 3.2

observation period. In the lower left panel, I have shown the resulting time series of the absolute magnetic field strength. Due to lacking observations by MDI, the magnetic field data begins at about 5000s into the time series. The most striking feature we see, when comparing the left side panels, is the correspondence between the strong magnetic fields and bright intensities, like those at 180″ and 6000s. In the upper right panel the extrapolated B_z is shown. The dark line at 190″ correspond to the strong magnetic field at 30″ in the west-east direction and 190″ spatial position, in the lower right panel. Also notice that the β-contour ($\beta = 1$), the white horizontal line in the B_z plot, has a dip where the strong magnetic field occur.

We have four datasets in July at 1319Å. The next one is shown in figure 4.3, 30 Jul (D). This set is very similar to the previous set, 30 Jul (B), in fact all the July sets are quite similar in appearance. The MDI observations also lack some data during the time series, which is seen in the lower left panel as dark bands. Perhaps the most exciting difference, is the somewhat altered magnetic field configuration. This set is about 6 hours later than 30 Jul (B), and the time-averaged magnetic field, lower right panel, has not changed too much. You can still recognise the similarity between the magnetic field in 4.3 and 4.2. It is quite possible that these two datasets were supposed to be of the same area of the sun. Anyway, previously we had one strong magnetic field component, we now identify four, at 60, 80, 170 and 190″. The reason seems to be that the solid line, which is the region where the B_z plot is extracted above, has moved closer to the network elements in this set, as in 30 Jul (B), it is situated in between the network elements.

The next set at 1319Å, is 31 Jul (B), shown in figure 4.4. This dataset was taken the next day, and the magnetic field at the surface of the sun has changed. The continuum radiation temperature and magnetic field plots on the left side, are still very similar to the previous two sets. Again, the largest changes can be seen in the magnetic field on the right side of the figure. There seems to be more black network elements, than in the previous two sets, which had an even distribution between black and white network elements. Also worth mentioning is the extreme dip in β at 100″. It goes down to 1Mm. We estimate the formation height for the 1319Å continuum to be at 0.7Mm, so it should not influence the intensity characteristics. We also observe the reason for this extreme dip, being that the slit (solid line in the lower right panel), lies directly above the center of a network element, where the magnetic field is at its strongest.

Turning to the final dataset in July of the 1319Å continuum, 31 Jul (D). The data is plotted in figure 4.5. This set also has a dip in the β contour down to about 1Mm, and the reason is again that B_z is calculated directly above the center of a network element.

Figure 4.6 shows the dataset of 10 Sep (A). I was able to include the whole slit this time, since the width only was 120″ and did not extend beyond the MDI magnetogram coverage. The detector on SUMER is responsible for the dark bands at either side of the plot of the continuum radiation temperature in the upper left panel. The white band in the lower left panel, is due to saturated data points. The slit used in this dataset, had a width of 0.3″, as opposed to the July datasets, which

used a slit width of 1.0″. The result is a more noisy plot of the continuum radiation temperature. This is clear if you for example compare the upper left panel with the upper left panel of figure 4.3. This time we observe two strong magnetic field components at about 40 and 100″ in the upper right panel. These strong magnetic fields can also be seen at the same locations in the left panels, as white stripes throughout the time series.

The final month with data on the 1319Å continuum is October. The first set is 02 Oct (B), shown in figure 4.7. All the October sets I use in this thesis, have rotation compensation turned on. This means that the instrument tracks one location on the sun throughout the entire time series. The magnetic field in this set, is relatively weak, which can also be seen in the plot of the β-contour, which lies at a height of about 2Mm for the entire slit. As we will see later on, the magnetic field is weakest in the October datasets. The reason is that the slit is situated at a fixed spot, with no strong magnetic fields, which we track due to the rotation compensation. The continuum radiation temperature is similar in appearance to the July datasets.

The final dataset for the 1319Å continuum is 04 Oct (A), see figure 4.8. This set does not differ significantly from the others I have already mentioned.

1199Å

We now turn to the observations of the 1199Å continuum, which is created at a height from 0.7 to 1.2Mm. The height is estimated from $\tau_{5000} = 1$. The first set is 10 Sep (C), shown in figure 4.9. This dataset was taken 5 hours after 10 Sep (A), and you may recognise some features in the magnetic field in both of the lower right plots of these datasets. For example, the three dark network elements at -10″ arcseconds in the west-east direction and around 30″ spatial position in figure 4.6, has moved to 30″ west-east position and the same spatial position in figure 4.9. Also notice that the network elements have changed slightly, with the middle network element now being considerably larger. This set uses the 1.0″ slit, and not the 0.3″ slit that 10 Sep (A) uses, and the continuum radiation temperature is, qualitatively, quite similar to the 1319Å datasets. We also notice that the correspondence between the magnetic field and the continuum radiation temperature still is very good, as shown in the time series plots on the left side.

The next dataset of 1199Å, is the 02 Oct (A) set, see figure 4.10. This set also uses rotation compensation as mentioned before for the other October datasets. This time series has perhaps the weakest magnetic field of all the datasets. This is also clear from the lower left panel, which has no bright blobs indicating the presence of a magnetic field. The exception is the white blob at about 80″ and 2800s, but not considering this, the time series plot of the magnetic field is nothing else but noise. This is also the reason for flat β-contour and its high altitude (upper right panel). Looking at the lower right panel we also see that the slit is situated away from any network elements, the closest being about 10″ away. The result of all this, is the very clear grain structure of the time series plot of the continuum radiation temperature (upper left panel). Also the contrast in the plot is very low.

This is evidently the closest we have been to a magnetic free dataset, yet as we will see, this set also exhibit the same characteristics as the other datasets, when comparing the continuum radiation temperature with the magnetic field strength in section 4.2.

The last dataset at 1199Å is 04 Oct (B), see figure 4.11. This dataset covers the same area on the sun as 04 Oct (A), which can be seen when comparing the time-averaged magnetic field plots in this figure with figure 4.8. This time series is the second dataset which uses the 0.3″ slit of the SUMER detector. This results in the very noisy image of the continuum radiation temperature (upper left panel). The network element at position 55″ east-west direction and 60″ spatial position, protrude more clearly in this dataset, and the β level goes down to ca. 1.2Mm.

1037Å

We know turn to the 1037Å continuum. The intensity at this wavelength comes from 0.9 to 1.4 Mm height in the atmosphere, and lies about at the height where the $\beta = 1$ level is, which would make this a very interesting wavelength to observe at, cf. McIntosh & Judge (2001). Unfortunately, the datasets are very poor and contains much noise, the main reason being the short exposure time leading to a low signal to noise ratio. The first set is 30 Jul (C) shown in figure 4.12. 30 Jul (B), 30 Jul (C) and 30 Jul (D) (figures 4.2, 4.12 and 4.3 respectively), all observe almost the same area of the sun. If you compare the plots of the time-averaged magnetic field (lower right panel), you can see how close they are. Therefore the magnetic field configuration is quite similar for these three datasets, so I will refer you back to those descriptions for more on the magnetic field.

The two final datasets of the 1037Å continuum was taken at the 31th of July. These observe the same areas as the datasets at 1319Å in July at the 31th (the datasets 31 Jul (A,B,C and D)). The first set is 31 Jul (A), see figure 4.13. I will refer you to the descriptions of the magnetic field at this date for more on the magnetic field. The radiation temperature plots in 31 Jul (A and C), are somewhat similar to the 1319Å datasets at this time, but lack the grain structure, at least it is hard to see it in the plots, because of the high noise signal in the data.

The last dataset for 1037Å is 31 Jul (C). The same things I said for 31 Jul (A), can be said for this set.

910Å

The last wavelength we have data for, is at 910Å. This continuum is created at 1.8Mm, well into the $\beta = 1$ layer. The first set is 10 Sep (B), shown in figure 4.15. The observations of this dataset are taken from a position on the sun, which is between the positions of 10 Sep (A) and 10 Sep (C). In time, it lies about 2 hours after 10 Sep (A), and 3 hours before 10 Sep (C). The continuum radiation temperature differs significantly from the datasets at the other wavelengths. Much less grain structure is seen, and the variations are more smooth. The contrast is

stronger, with dark stripes at 95″ spatial position, and bright bands at 65″ spatial position (upper left panel). The bright radiation temperature bands correspond well with the strong magnetic field lines, but the magnetic field structure is very narrow, compared to the width of the continuum radiation temperature at the same locations.

The second dataset is 02 Oct (C), see figure 4.16. The observations in this set uses rotation compensation, and are taken close to the position which was observed in 02 Oct (B). This can be seen when comparing the lower right panels of this figure and figure 4.7. The continuum radiation temperature in this set does not have as large contrast as 10 Sep (B), it lacks the darkest intensities shown at position 95″ spatial position in figure 4.7 (upper left panel). It exhibits some interesting fine structure (thin horizontal lines), on the other hand, at spatial positions 50 to 65 during the entire time series. Also interesting is the three magnetic stripes at 80-100″ spatial position in the lower left panel. If we compare those with the continuum radiation temperature time series (upper left panel), where we see only one bright stripe at those coordinates, it seems as if the magnetic fields have closed in on themselves.

The final dataset is 05 Oct (A), shown in figure 4.17. This datasets was taken near to the observations performed at the 4th of October (04 Oct (A and B)). It has a very interesting β-contour, with two dips at 35 and 55″ spatial position, very like a *W*.

4.1.2 The 1319Å and 1199Å continuum

In this section I have summarised the qualitative characteristics of the observations of the continuum at 1319 and 1199Å given in the previous section.

The datasets at 1319Å can be grouped in two. Qualitatively *and* quantitatively the datasets in July are similar to each other (figs. 4.2 - 4.5). The same goes for the October datasets (figs. 4.7 and 4.8). Comparing the months though, shows that the contrast in the continuum radiation is larger for the October sets than for the July sets, cf. figure 4.7 and figure 4.3.

We can also observe the bright grains in the continua clearly, e.g. figure 4.7. When comparing the continuum with the magnetic field we also see that the brightest intensities align with the strongest magnetic field, see figure 4.3.

The 1199Å continua are similar to the 1319Å continua, compare for example figures 4.10 and 4.7.

4.1.3 The 1037Å and the 910Å continuum

In this section I have summarised the qualitative characteristics of the observations of the continuum at 1037 and 910Å.

The continua at 1037Å and 910Å differ markedly from the 1319Å and 1199Å continua. They have fewer grains and more smooth variations, compare figure 4.16 with figure 4.7 and figure 4.13 with figure 4.4.

The 1037Å data were taken at the bare part of the SUMER detector, which is why they have a low signal-to-noise ratio, the data is noisy, e.g. figure 4.13. They also exhibit low contrast, similar to the 1319Å datasets in July, compare figures 4.13, 4.4 and 4.6. The 910Å data, on the other hand, show quite strong contrast, e.g. figure 4.16. The contrast is a measure of the range of the radiation temperature. We will have values for those in the next section, when we consider the scatterplots.

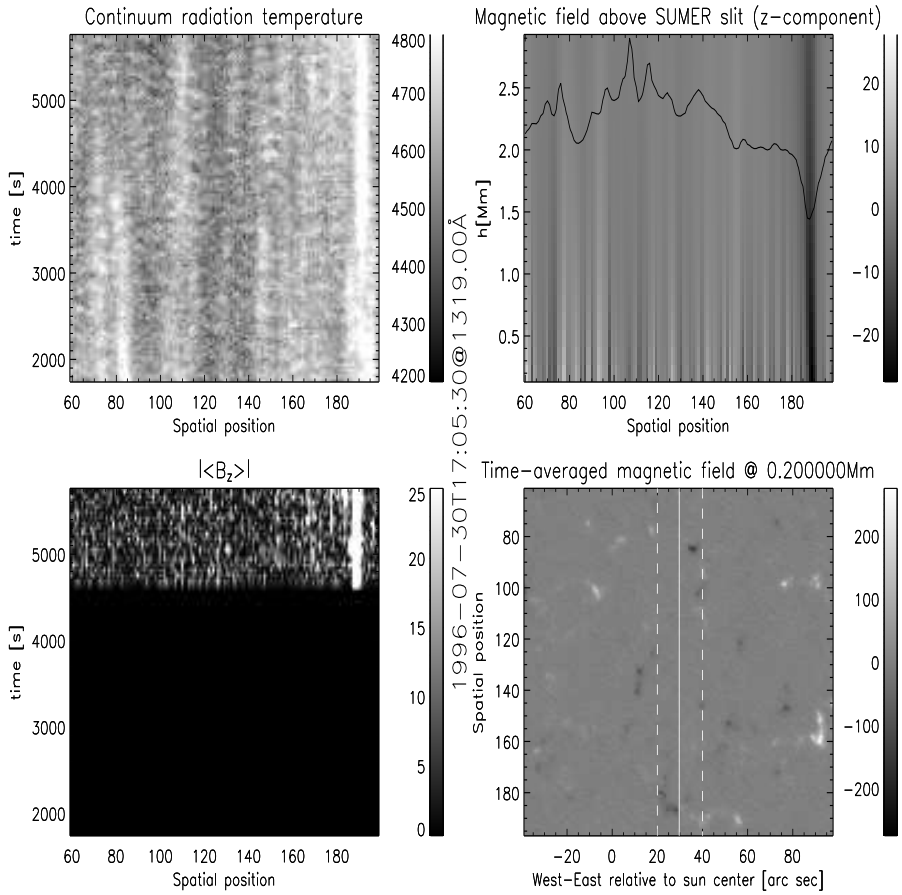

Figure 4.1: **Example figure of the continuum observations at 1319Å.** (This figure is made from the same dataset as in figure 4.2). Shown are the radiation temperature (upper left panel) and the absolute value of the magnetic field vertical component (lower left) as functions of slit position and time. The radiation temperature is given in kelvin and the magnetic field in gauss. The black areas of the magnetic field timeseries plot, are gaps in the data. The lower right panel shows the magnetic field strength as function of position on the sun with the position of the SUMER slit marked as vertical lines for the middle (solid line) of the time series. The dashed lines shows the span covered by the timeseries. The 0.2Mm height reference in the title, refers to the height where $\tau_\nu = 1$ for the Ni I 6768 Å line, i.e. 0.2Mm above $\tau_{5000} = 1$. The upper right panel shows the height profile of B_z along the slit of a potential field extrapolation of the magnetic field with the height of $\beta = 1$ marked. White and black indicate opposite polarities.

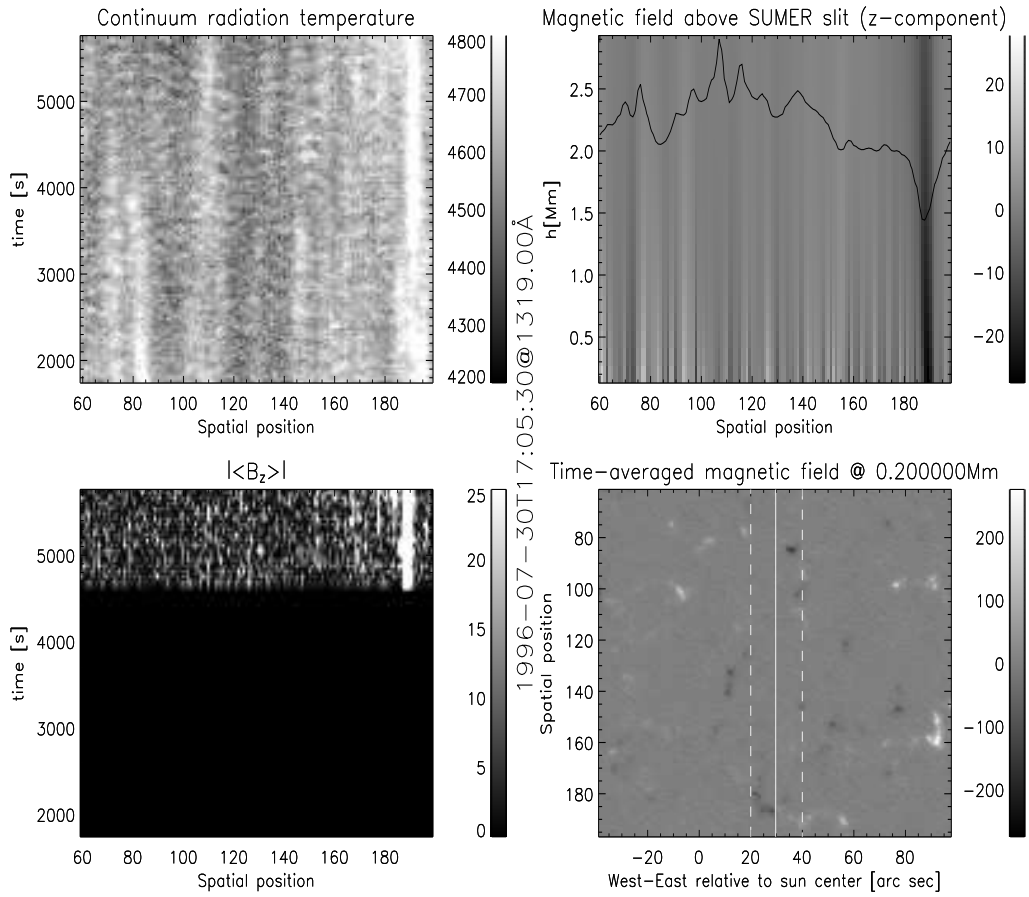

Figure 4.2: **Continuum observations at 1319Å.** (30 jul (B)) See the figure text to figure 4.1 for explanations.

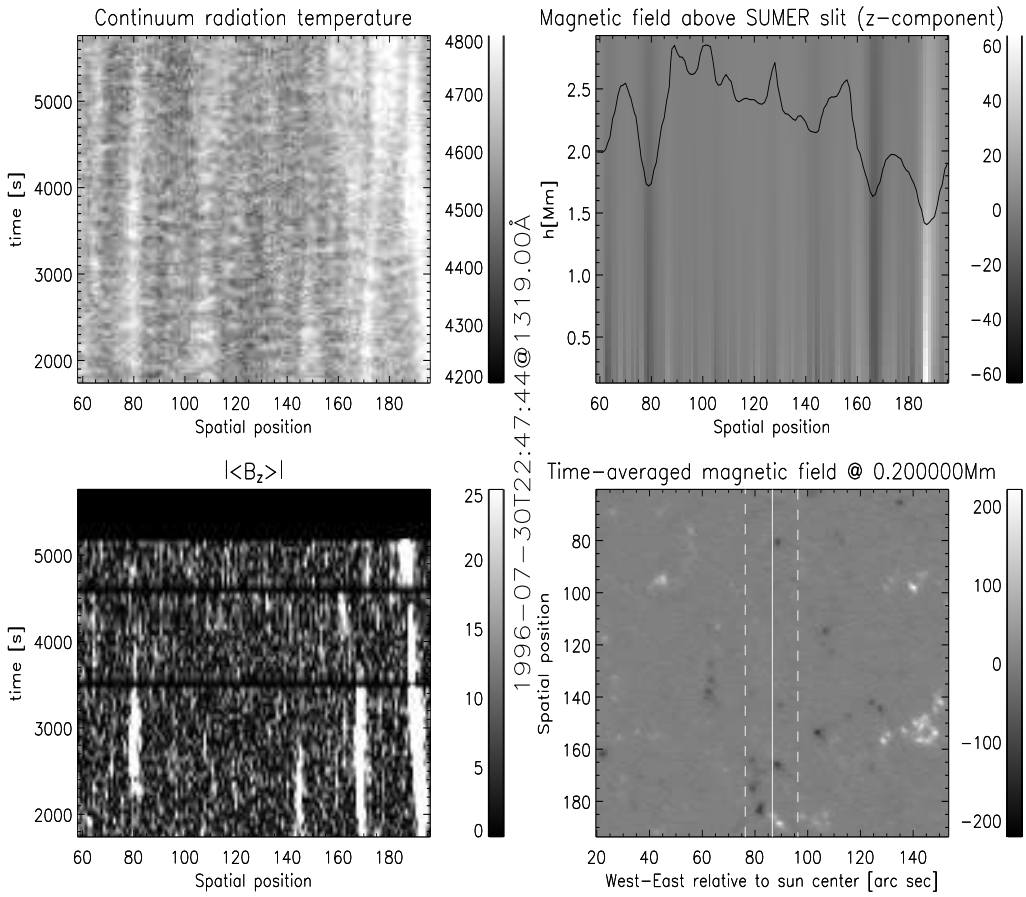

Figure 4.3: **Continuum observations at 1319Å.** (30 jul (D)) See the figure text to figure 4.1 for explanations.

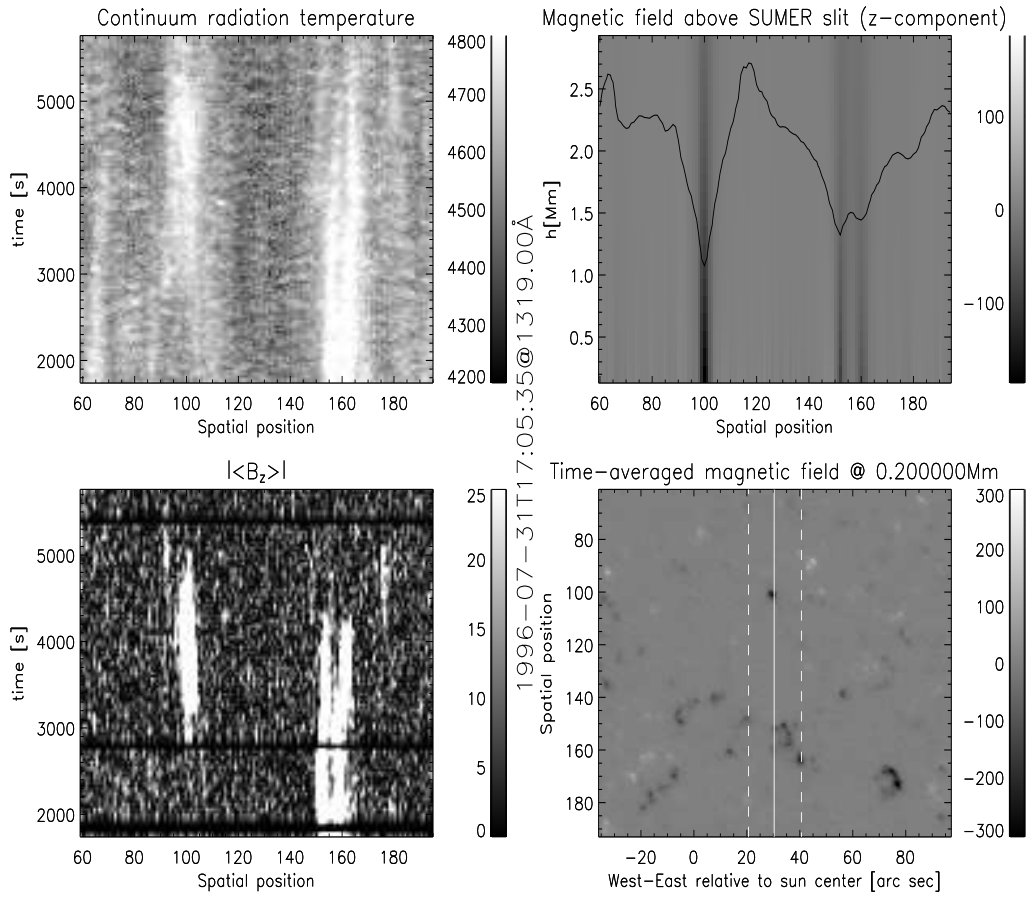

Figure 4.4: **Continuum observations at 1319Å.** (31 jul (B)) See the figure text to figure 4.1 for explanations.

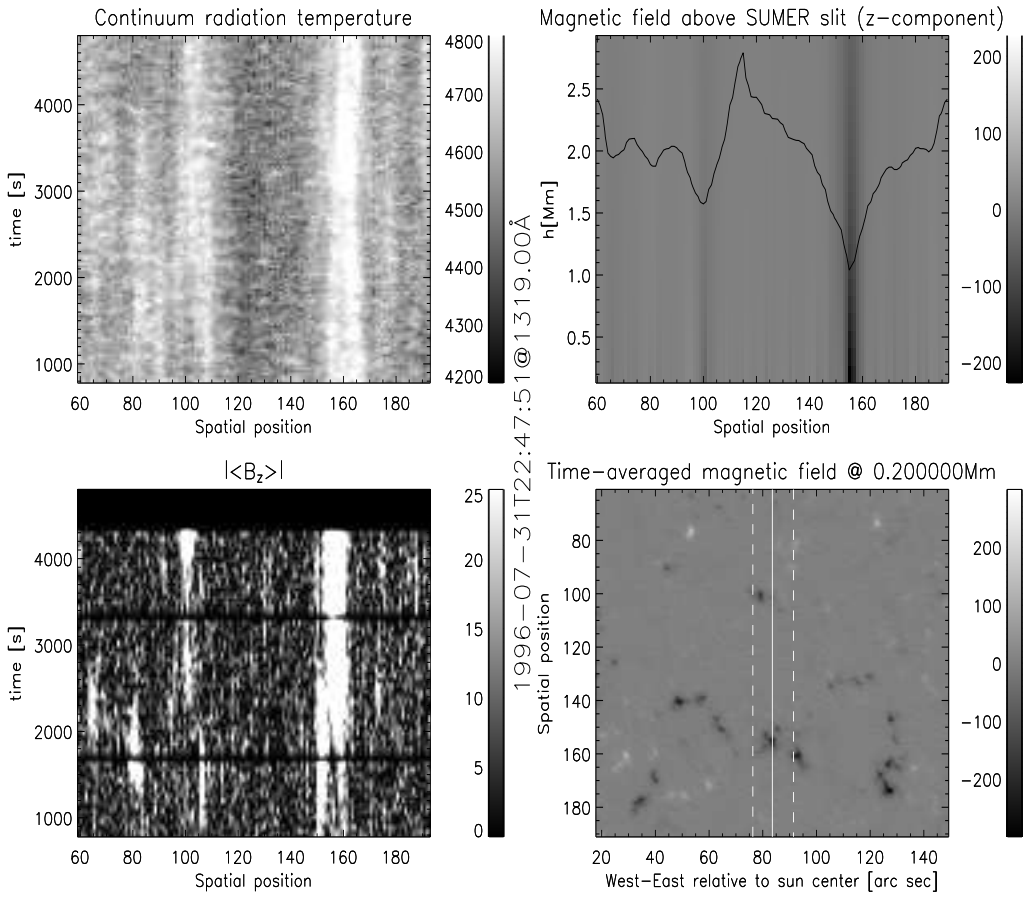

Figure 4.5: **Continuum observations at 1319Å.** (31 jul (D)) See the figure text to figure 4.1 for explanations.

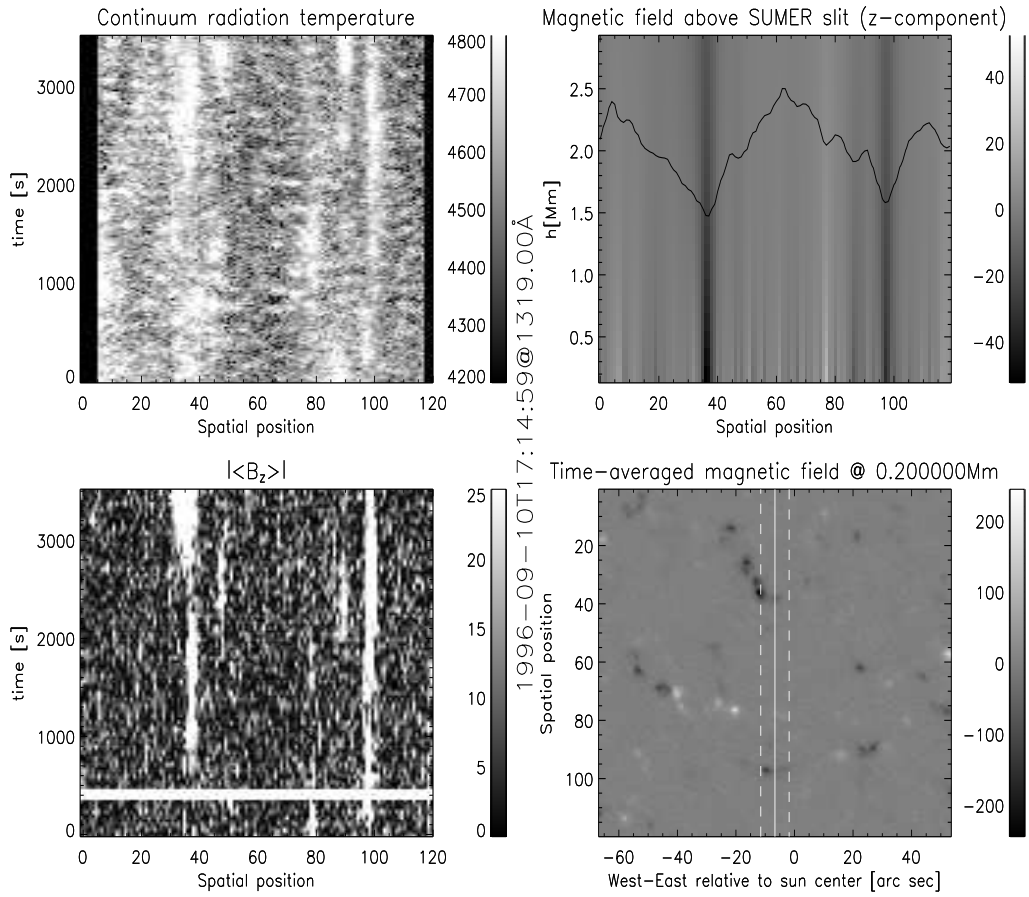

Figure 4.6: **Continuum observations at 1319Å.** (10 sep (A)) See the figure text to figure 4.1 for explanations. The white band in the lower left panel is due to saturated data points. The black stripes at the left and right of the upper left panel, are areas with no signal.

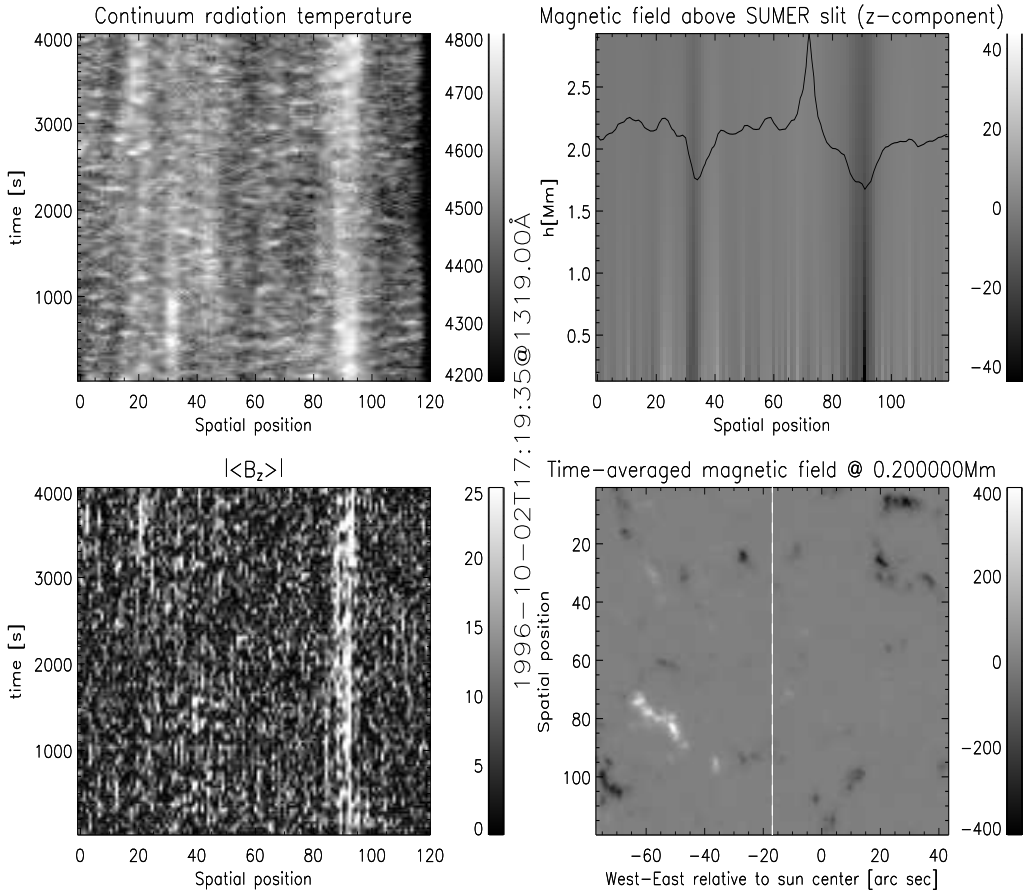

Figure 4.7: **Continuum observations at 1319Å.** (02 oct (B)) See the figure text to figure 4.1 for explanations. This set lacks the dashed stripes in the lower right panel, since it uses rotational compensation to follow the suns rotation.

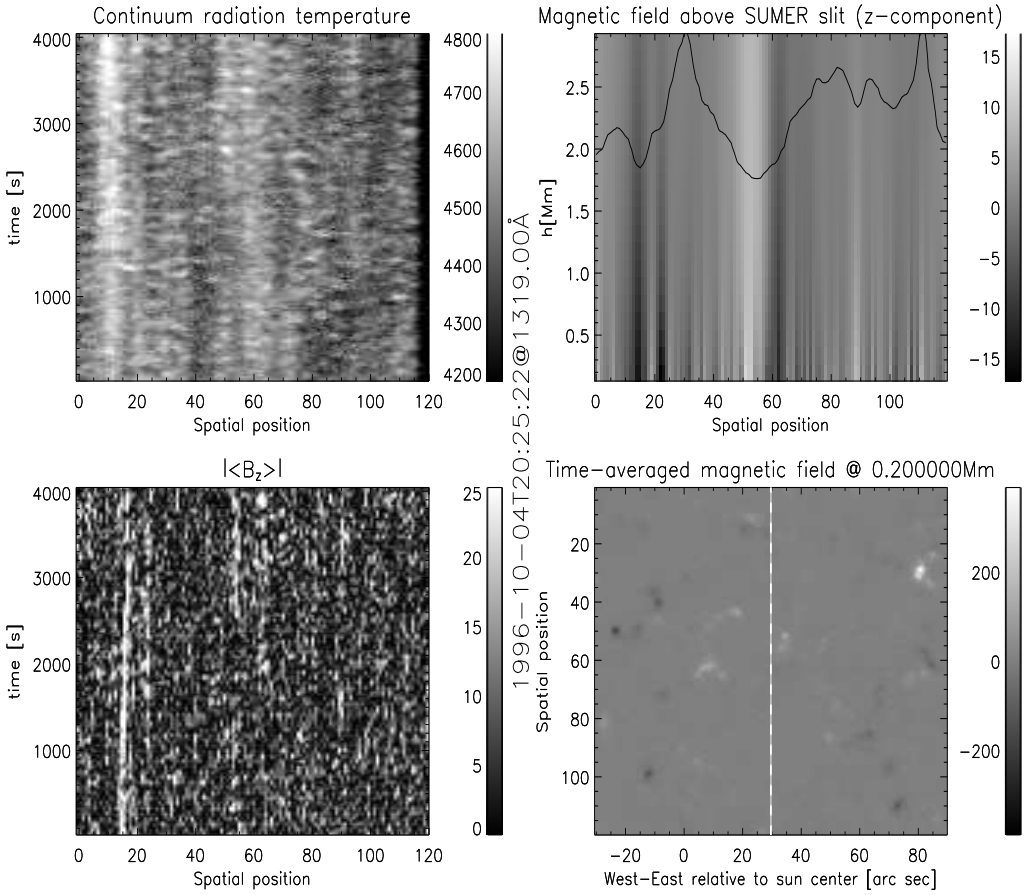

Figure 4.8: **Continuum observations at 1319Å.** (04 oct (A)) See the figure text to figure 4.1 for explanations. This set lacks the dashed stripes in the lower right panel, since it uses rotational compensation to follow the suns rotation.

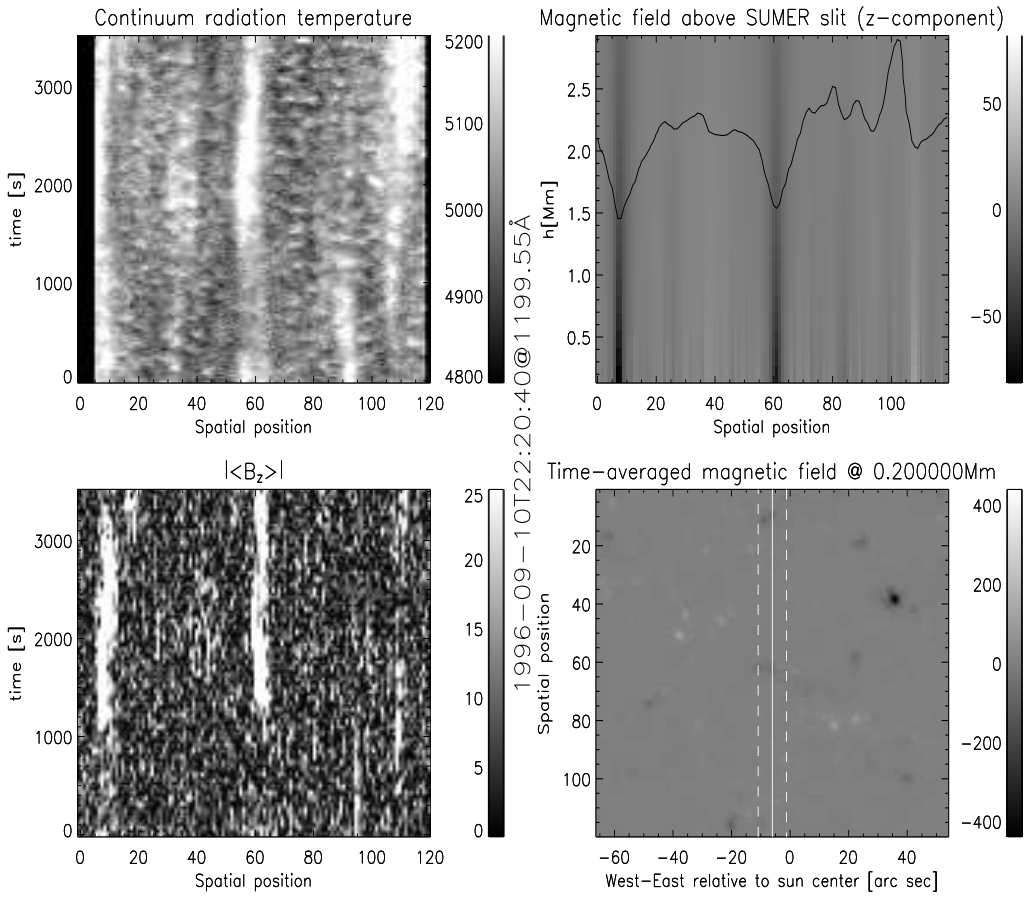

Figure 4.9: **Continuum observations at 1199Å.** (10 sep (C)) See the figure text to figure 4.1 for explanations.

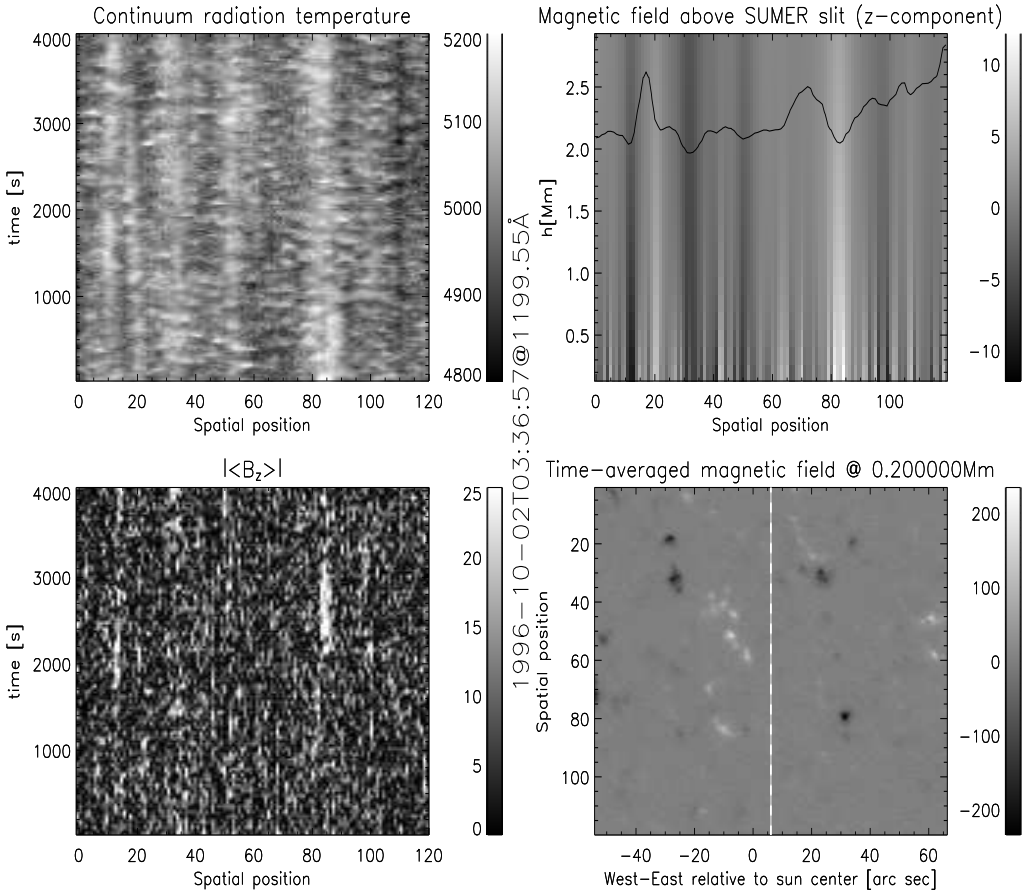

Figure 4.10: **Continuum observations at 1199Å.** (02 oct (A)) See the figure text to figure 4.1 for explanations. This set lacks the dashed stripes in the lower right panel, since it uses rotational compensation to follow the suns rotation.

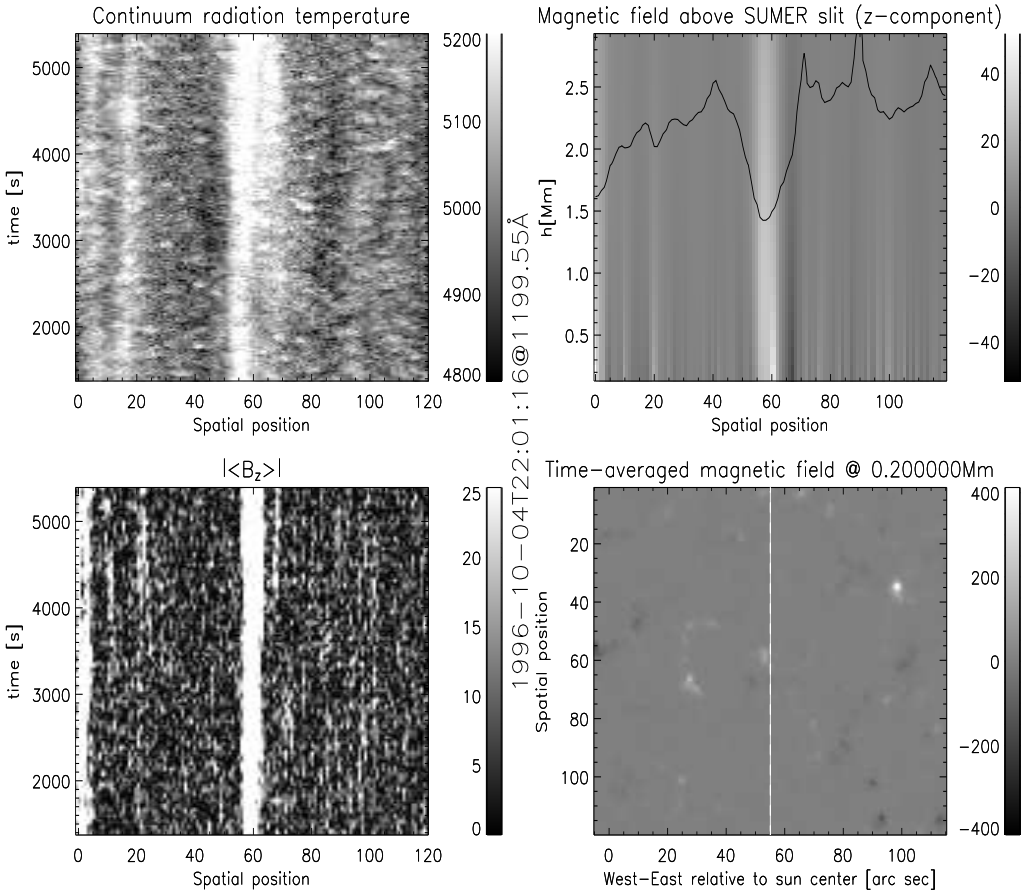

Figure 4.11: **Continuum observations at 1199Å.** (04 oct (B)) See the figure text to figure 4.1 for explanations. This set lacks the dashed stripes in the lower right panel, since it uses rotational compensation to follow the suns rotation.

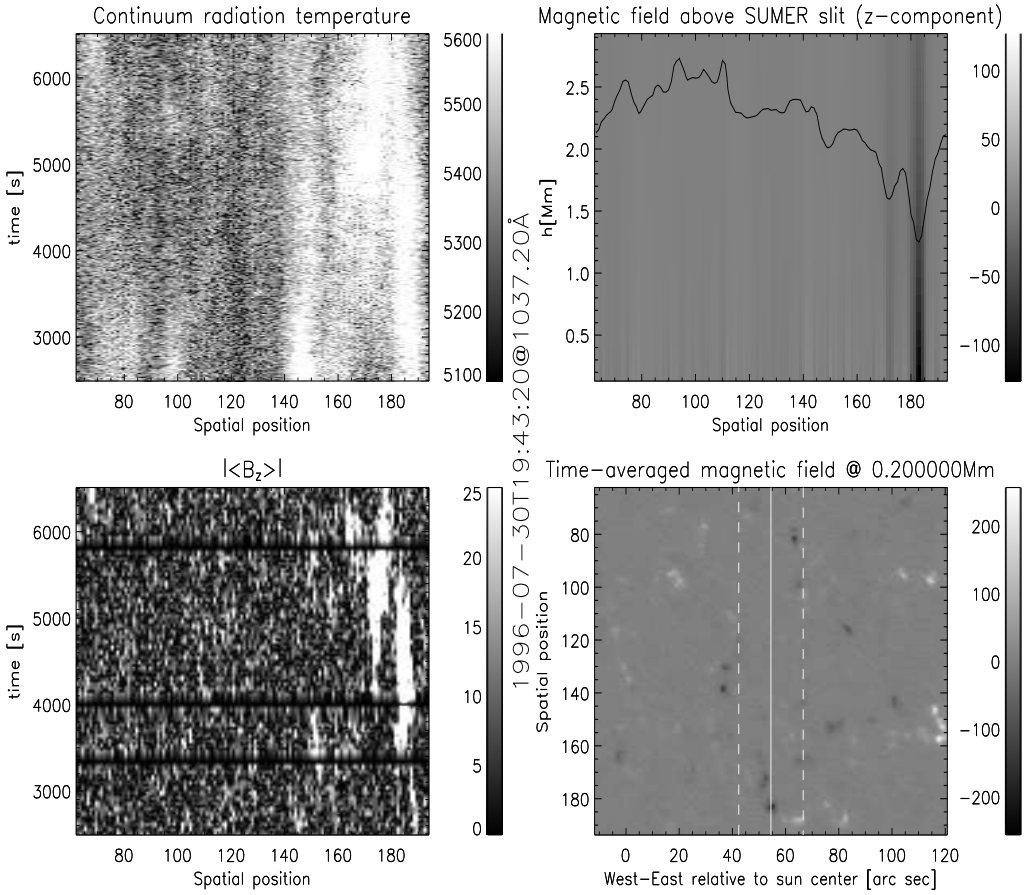

Figure 4.12: **Continuum observations at 1037Å.** (30 jul (C)) See the figure text to figure 4.1 for explanations. Notice the black bands in the magnetic time series, which are due to missing data.

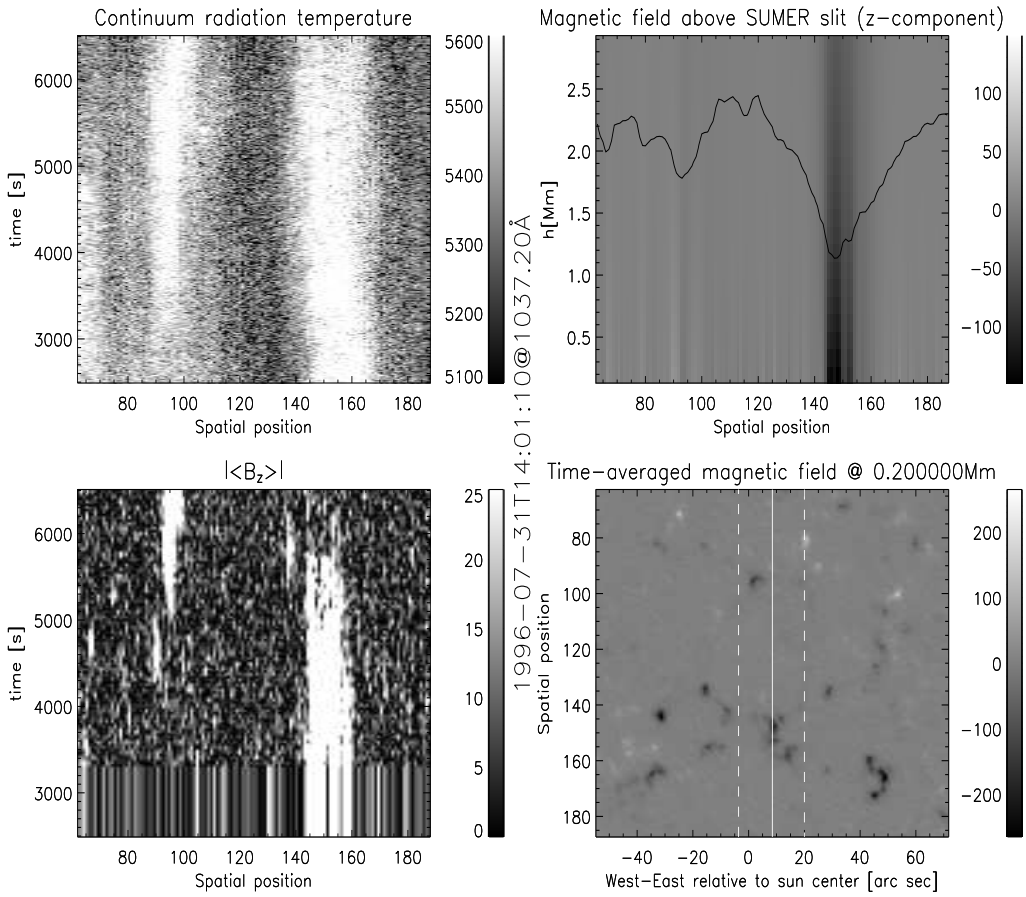

Figure 4.13: **Continuum observations at 1037Å.** (31 jul (A)) See the figure text to figure 4.1 for explanations. The gray stripes in the lower left panel are made by the plotting procedure.

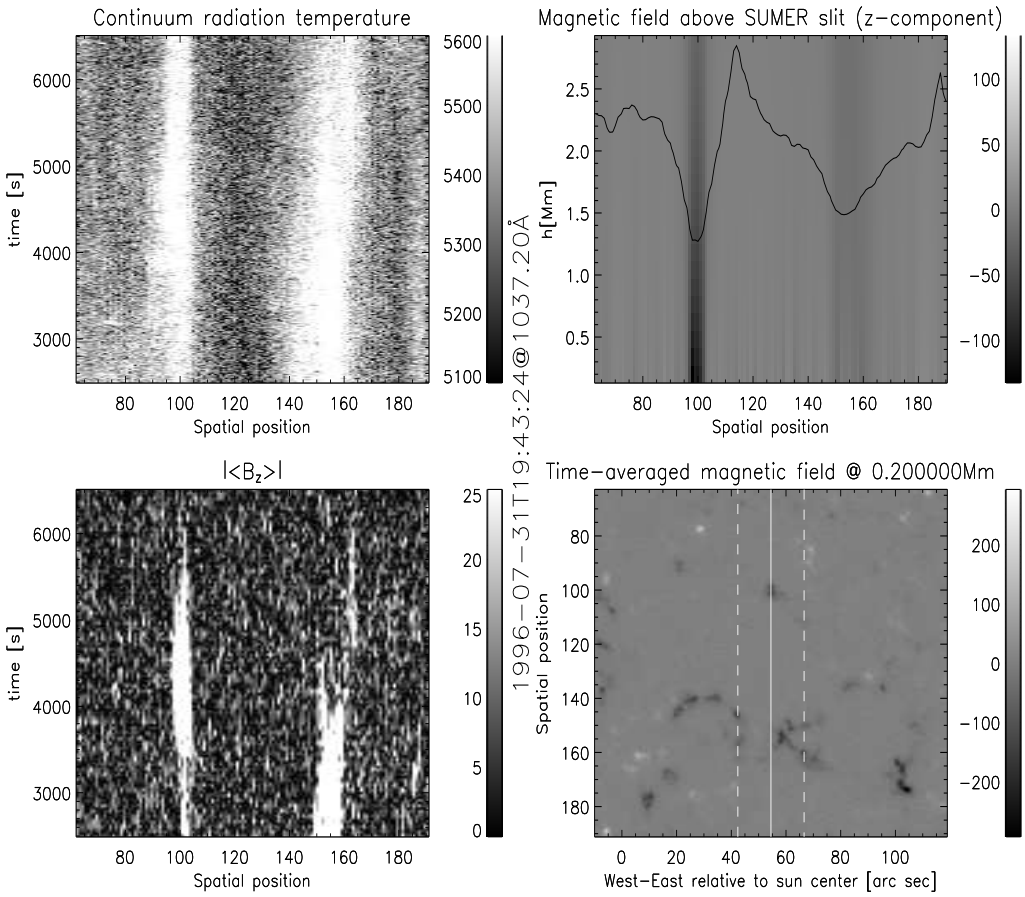

Figure 4.14: **Continuum observations at 1037Å.** (31 jul (C)) See the figure text to figure 4.1 for explanations.

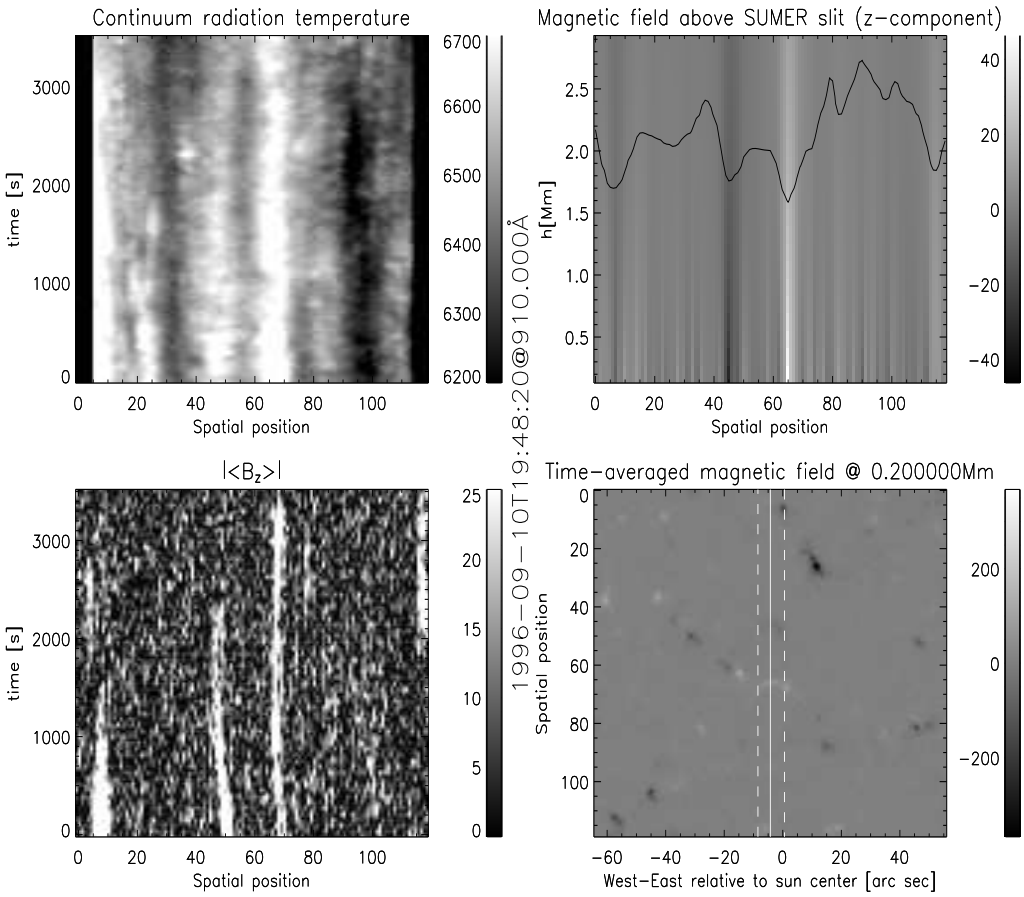

Figure 4.15: **Continuum observations at 910Å.** (10 sep (B)) See the figure text to figure 4.1 for explanations.

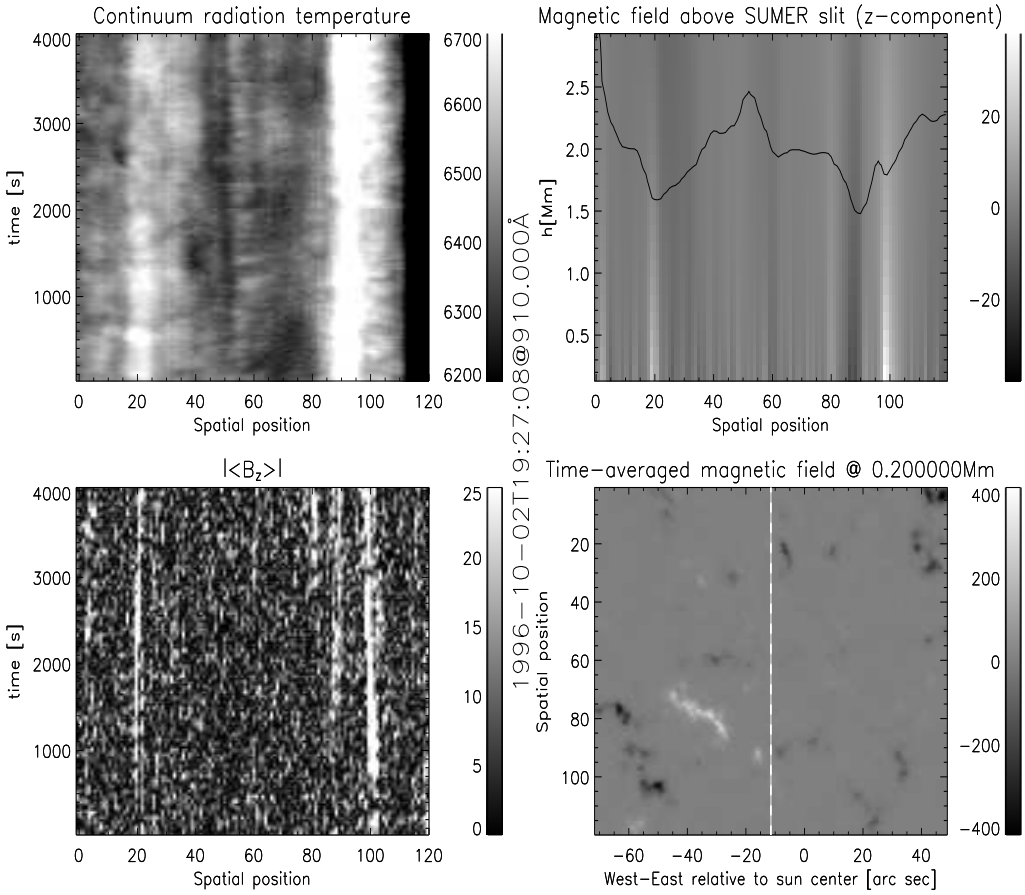

Figure 4.16: **Continuum observations at 910Å.** (02 oct (C)) See the figure text to figure 4.1 for explanations. This set lacks the dashed stripes in the lower right panel, since it uses rotational compensation to follow the suns rotation.

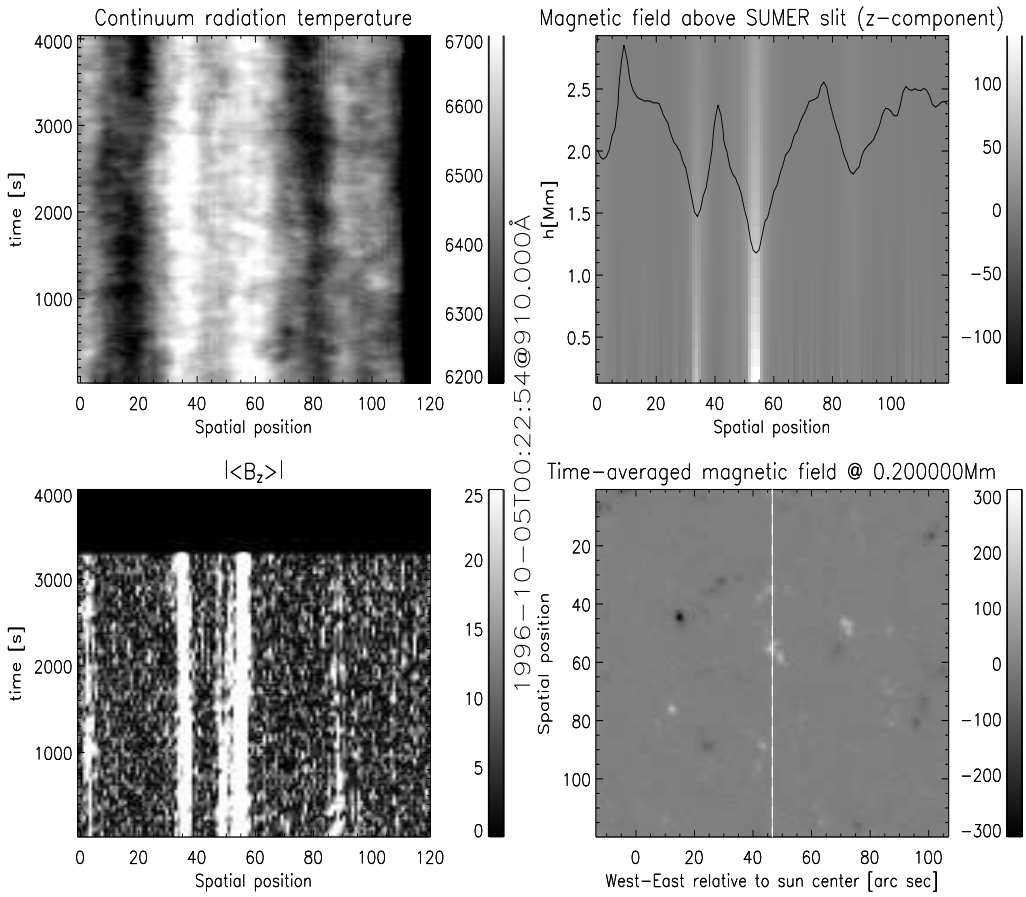

Figure 4.17: **Continuum observations at 910Å.** (05 oct (A)) See the figure text to figure 4.1 for explanations. This set lacks the dashed stripes in the lower right panel, since it uses rotational compensation to follow the suns rotation.

4.2 Correlations between the radiation temperature and magnetic field

In the previous section we looked at the visual correlation between the continuum radiation temperature and the magnetic field. Let us now see if we can quantify that data. The data are analysed with the help of scatterplots, using the methods described in section 3.2.5. The plots are shown in figures 4.19 to 4.34. Each cross is the measured value at one slit position. In the series which does not have rotation compensation, each cross corresponds to 20 minute segments along each slit position. The vertical line in the magnetic field strength plots, corresponds to $3\sigma_{B_z}$. This value was obtained by calculating the standard deviation for the spatial positions where the magnetic field was weakest[2]. I then choose the median value from the standard deviations as σ_{B_z}, and multiply by 3 to get $3\sigma_{B_z}$. The little boxes show the mean and stddev for the points around its vicinity. They are obtained by dividing into four regions. All datapoints which have x-values below a quarter of the maximum x-value in the dataset, are assigned to region 1, the ones which have values above this, but below half is assigned to region 2, and so on. Then I calculate the mean of the x-values and y-values, and the standard deviation of the y-values.

The data are presented on tabular form in table 4.1. See also figure 4.35 for a scatterplot of all the datasets in one figure.

4.2.1 Overview of scatterplots

The data are presented in the same order as in section 4.1.1.

1319Å

The first dataset analysed with observations in the 1319Å continuum is from 30 July 1996, designated 30 Jul (B), shown in figure 4.19. The lower left panel shows the radiation temperature versus the magnetic field strength. This panel shows the connection between dark and bright areas in the left side panels of figure 4.2. This dataset does not use rotation compensation, which means that the slit passes over changing magnetic features during the time series. To reduce this effect when analysing the data, I have subdivided each timeseries at each spatial position into 20 minute segments. Each cross in the plots show the value of one of these 20 minute segments. From the lower left panel we see that most points lie at $|<B_z>| < 10G$, with radiation temperatures from 4400 to 4600K. These points are representative of the dark regions in the plots from the previous section. Notice that the correlation is not one-to-one, as there are several points with high radiation temperatures, but low magnetic field strengths. We will return to this point later in this chapter. You may also notice that there are only high radiation temperatures, where there are high B_z.

[2]By weakest I mean that I chose the spatial positions, where the magnetic field was less than 5 percent of the mean value of the magnetic field

This panel shows what we indicated in the previous section, that the high intensity regions correspond with strong magnetic fields, and the low intensity regions does not correspond with strong magnetic fields.

If we look at the upper left panel, it shows the relative standard deviation of the observed intensity versus the magnetic field. This is a measure of the oscillations, the "grains", we see in figure 4.2. We notice that $\frac{\sigma[I]}{<I>}$ varies over a great range where there is very weak magnetic fields, approximately below 10G. On the other hand the oscillations get smaller as we increase the strength of the magnetic field. The upper right side panel shows this in another way. Here we plot $\frac{\sigma[I]}{<I>}$ versus the radiation temperature, but since the relation between the radiation temperature and the magnetic field is strong, the trend in the datapoints show the same downward slope as the left side panel did. As we see from the plot, the amplitudes of the oscillations are small, when the radiation temperature is large, and vice versa. When the radiation temperatures are low, the oscillations vary over a larger range. The final panel (lower right), show the absolute standard deviation ($\sigma[I]$) versus the radiation temperature. We now see that there is an increase in the amplitude of the oscillations at increased radiation temperature, the *relative* intensity oscillations thus decrease with increased intensity/magnetic field strength, while the *absolute* intensity oscillations increase.

Remember that the datapoints in the right side panels, only use data extracted from the SUMER observations, i.e. the upper left panel of figure 4.2, and therefore does not suffer from any copointing errors.

The next dataset is 30 Jul (D), shown in figure 4.20. The results are similar to that of 30 Jul (B). In fact, all the scatterplots for the July datasets in 1319Å, 30 Jul (B and D) and 31 Jul (B and D), show the same trends and data values.

The September datasets, 10 Sep (A), are shown in figure 4.23. This dataset is noisy, because of the combination of narrow slit and short exposures. In figure 5.2 (upper left panel), I have plotted the temperature distribution of the radiation temperatures. The dotted vertical line indicates the lowest detectable radiation temperature with the instrument settings used in the current dataset. You will see that this is 4300K. This means that the datapoints in figure 4.23, which lie below 4300K are artifacts of the reduction procedure employed in the preprocessing, specifically the geometric correction. If we neglect those data points, we see that the trends are the same as in the July datasets of the 1319Å continuum. The values on the axis are somewhat different, and they are summarised in table 4.1.

The final month of observations is October. For these observations rotation compensation was used, so all the datapoints are calculated for each slit position and the entire duration of the time series. The first dataset is 02 Oct (B), shown in figure 4.24. You notice immediately that there are fewer crosses, there should be about 120 crosses, each corresponding to one slit position in the 120″ wide slit. The October datasets have weaker magnetic fields, and the strongest in this particular dataset is at about 25G. Still we recognise the trends we saw in the other datasets. In the lower left panel, we see that the highest radiation temperatures correspond to relatively strong magnetic fields, while the radiation temperatures

are lower and vary more, where there are weak or no magnetic fields (<~ 3G). The amplitude oscillations, $\frac{\sigma[I]}{<I>}$ (upper left panel), are smaller when magnetic fields are stronger. On the right hand side, the relative (upper panel) and absolute (lower panel) intensity oscillations, decrease and increase, respectively, with increasing radiation temperatures, as we have seen in the other datasets.

The last dataset of the 1319Å observations, are 04 Oct (A), see figure 4.25. In the panels on the left hand side, there is more scatter than is observed in the other datasets. Especially the points with radiation temperatures around 4600K, which lie in regions with magnetic fields below 5G. This probably corresponds to the regions at slit position 10″ in figure 4.8, left hand side. You may notice that at 3000 to 4000s, the continuum radiation temperature is very high, but that the magnetic field is weak and slants to the right. This would show up as points with high radiation temperatures, but low magnetic fields, as we observe in the scatterplot. It is harder in the upper left panel in figure 4.25, to see the trends I see for the other datasets. The points seem to lie scattered around the entire window, with no clear trend seen anywhere. This is perhaps an artifact of the magnetic field not being directly connected to the continuum radiation temperature.

1199Å

We now turn to the 1199Å continuum. The first dataset is 10 Sep (C), shown in figure 4.26. If we consider the lower left panel, we can see the trend we also saw in the 1319Å datasets, that the radiation temperature is larger where there are strong magnetic fields. This is in fact, evident in all of the datasets, independent of wavelength. There is a cluster of points at about 10G and 5200K in this panel. If we compare with figure 4.9, we see that there are some areas of the time series plots, where the continuum radiation temperature is high, but the magnetic field is weak, like at slit position 110″ and time 3000s. This should explain such clusters, as we also saw in the previous section on the 1319Å scatterplots. On the right side panels we see some outliers with high $\sigma[I]$ equal to 0.005 and $\frac{\sigma[I]}{<I>}$ equal to 0.25. If we compare with the upper left panel, we see that these points lie in regions with weak magnetic fields, in fact below the vertical line ($= 3\sigma$), which indicates that there is no detectable magnetic field. If we compare with figure 4.9, we see in the upper left panel at slit position 70-80″ grains with high contrast. This is an indicator of large amplitude variations, i.e. a large value for $\sigma[I]$. We also see that the same area in the lower left panel, where we see the magnetic field time series plot, has no magnetic field present, or at least it is very weak. This is the plausible reason for these outliers. We see that the rest of the points follow the same trends we have observed in the 1319Å data.

The next dataset is 02 Oct (A), shown in figure 4.27. This plot has fewer datapoints, since it uses rotation compensation, which means that I did not subdivide the time series into segments for analysis. This dataset has the weakest magnetic fields, below 12G.

The final dataset at 1199Å, is 04 Oct (B), see figure 4.28. The right side panels

look very nice. They indicate a linear relationship between the intensity oscillations and radiation temperatures.

1037Å

We now proceed to the next dataset, which is 30 Jul (C), see figure 4.29. The first thing we notice is the larger number of datapoints. This is due to the length of the time series, and that we have data from MDI during the whole of the time series. This dataset is, as I already have mentioned, a very noisy dataset. A little remark is in place on the lower limit at 5100K on the radiation temperatures. Take a look at figure 5.2, which is a histogram of the radiation temperature. In the upper right panel, which shows the radiation temperature distribution for the 1037Å datasets, you will see a vertical line at 5100K. This is the lowest radiation temperature, which the detector is able to measure at the given wavelength, with the given choice of slit, cf. table 3.2. If the data contains radiation temperatures below this, it is a result of the reduction process we use when preparing the data, specifically the geometric correction. I have therefore removed the datapoints below 5100K in the scatterplots of the 1037Å continuum. Now, if we consider the data, we see that it shows the same trends that 30 Jul (B) did. Its worth mentioning the high $\sigma[I]$ in the lower right panel. At about 5300-5400K we see large values for $\sigma[I]$. This corresponds to large variations in intensity in the brightest segments of figure 4.12 (upper left panel).

The next dataset is 31 Jul (A), shown in figure 4.30. Qualitatively, this plot is similar to the previous 1037Å dataset. This dataset has a magnetic field with a maximum of about 150G.

The last dataset set at 1037Å is 31 Jul (C). The scatterplots are shown in figure 4.31. Consider the lower left panel, which show the radiation temperature and the magnetic field strength. We see that below the 3σ level (the vertical line), the radiation temperature varies between 5000 and 5400K. This is equivalent to no magnetic field in that area. When we go above $3\sigma \approx 10G$, we see that the radiation temperature increase to about 5600K. Also, notice in the upper left panel, that the oscillation amplitudes are much smaller for high B_z, than for low B_z.

910Å

Finally, we have the observations highest in the atmosphere, at 910Å. The first dataset is 10 Sep (B), shown in figure 4.32. The results are similar to what we have already seen in the other datasets.

The next dataset is 02 Oct (C), which is plotted in figure 4.33. See also section 5.2.1 for a comment on the lower left panel.

The last dataset is 05 Oct (A), shown in figure 4.34. This figure is what we maybe can call a “typical” set, in that it clearly shows how the correlation between the values behave. As we now have tracked the datasets up through the chromosphere, we have now reached a radiation temperature of about 6500K. The data

show a clear increase in radiation temperature, from 4400K at its lowest, up to about 6500K in the 910Å datasets.

4.2.2 Summary of scatterplots

I have compacted all the figures of the previous section into one figure shown in figure 4.35. We see that the data show the same trends for all datasets. The scatter in $\frac{\sigma(I)}{<I>}$ decreases with increasing magnetic field strength. $\frac{\sigma(I)}{<I>}$ has an downward slope with increasing radiation temperature while $\sigma(I)$ shows an upward slope with increasing radiation temperature. The scatter in radiation temperature decreases with increasing magnetic fields, and have larger values where there are strong magnetic fields. The datasets also show an increase in radiation temperature with decreasing wavelength, cf. lower left panel of figure 4.35 and table 4.1. We see that the radiation temperature goes from 4400K to 6600K over a height range of about 1Mm.

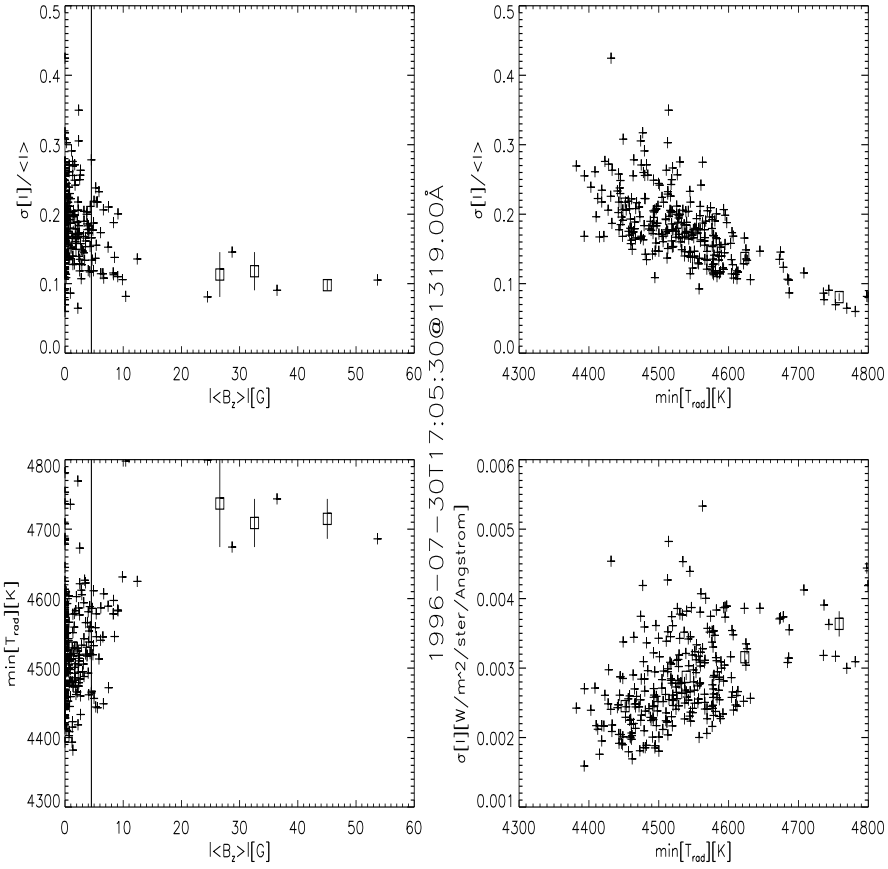

Figure 4.18: **Example scatterplots at 1319Å.** (This figure is made from the same dataset as in figure 4.19). The scattergrams show the correlation between the relative intensity amplitude and the magnetic field strength (upper left), the relative intensity amplitude and minimum intensity at a given slit position, given as radiation temperature (upper right), the minimum radiation temperature as a function of magnetic field strength (lower left) and absolute intensity amplitude as function of minimum intensity, given as radiation temperature (lower right). The little boxes show the mean and stddev for the points around its vicinity.

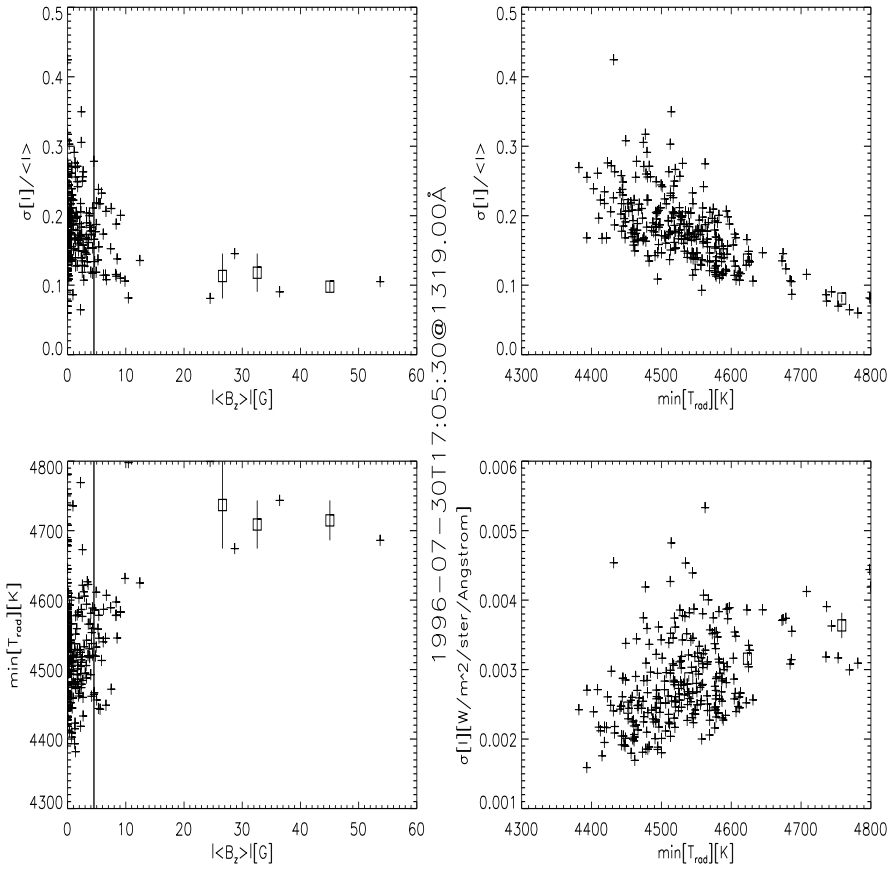

Figure 4.19: **Scatterplots at 1319Å from 30 jul (B).** See the figure text to figure 4.18 for explanations.

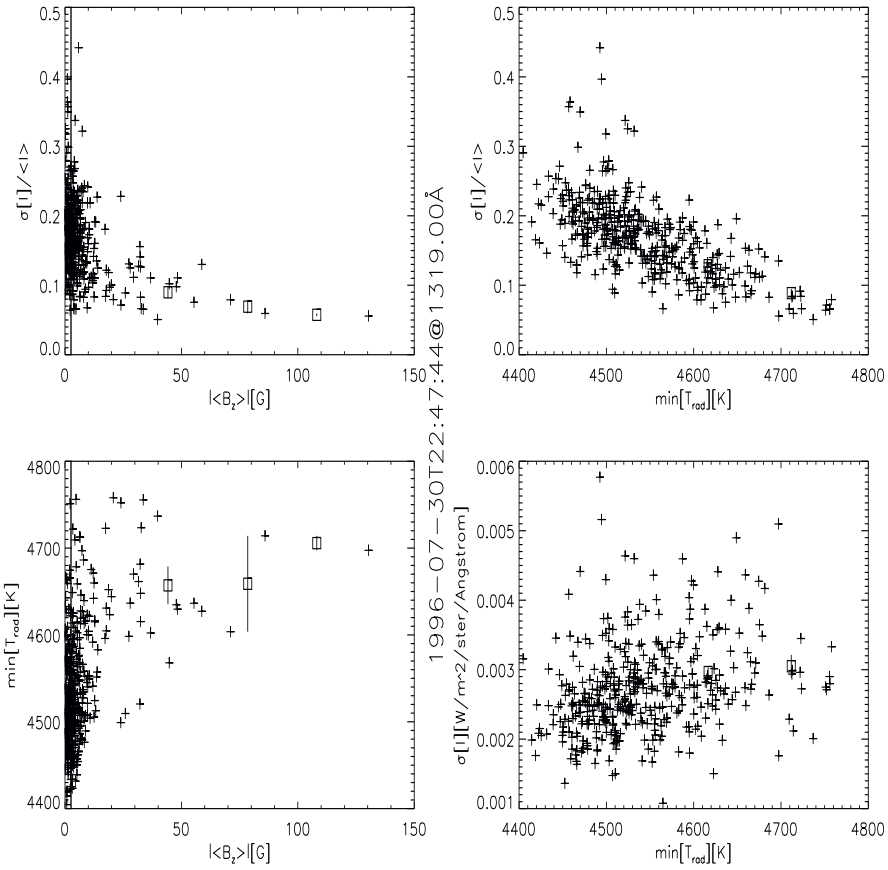

Figure 4.20: **Scatterplots at 1319Å from 30 jul (D).** See the figure text to figure 4.18 for explanations. Since this series does not have rotation compensation, each cross corresponds to 20 minute segments along each slit position.

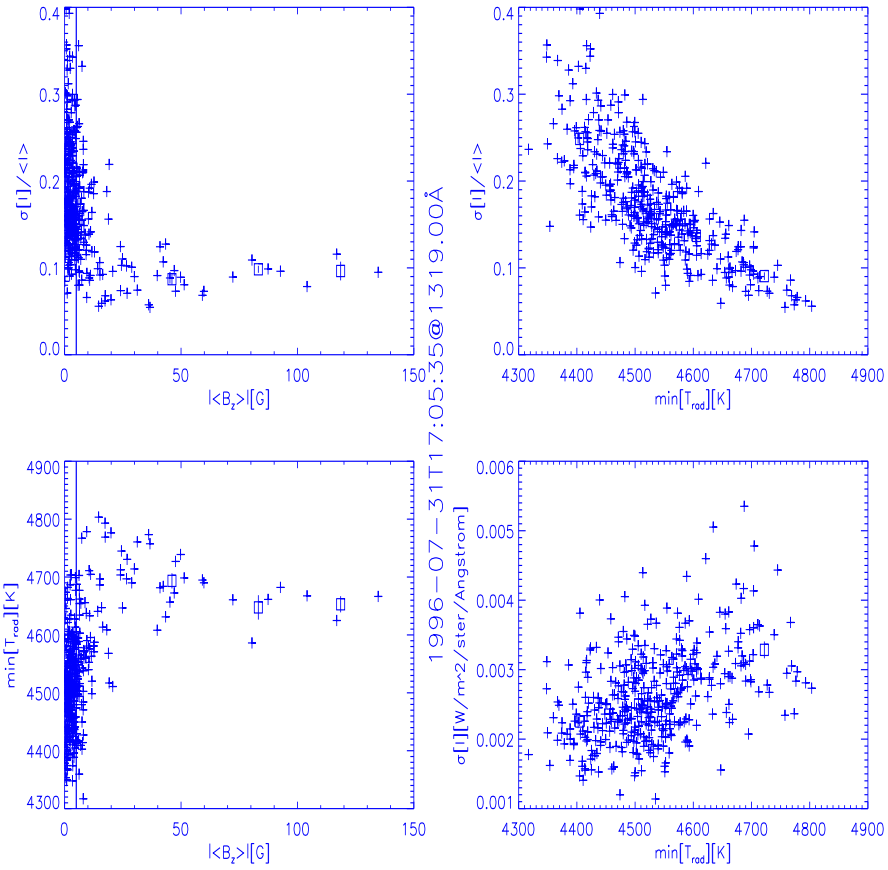

Figure 4.21: **Scatterplots at 1319Å from 31 jul (B).** See the figure text to figure 4.18 for explanations. Since this series does not have rotation compensation, each cross corresponds to 20 minute segments along each slit position.

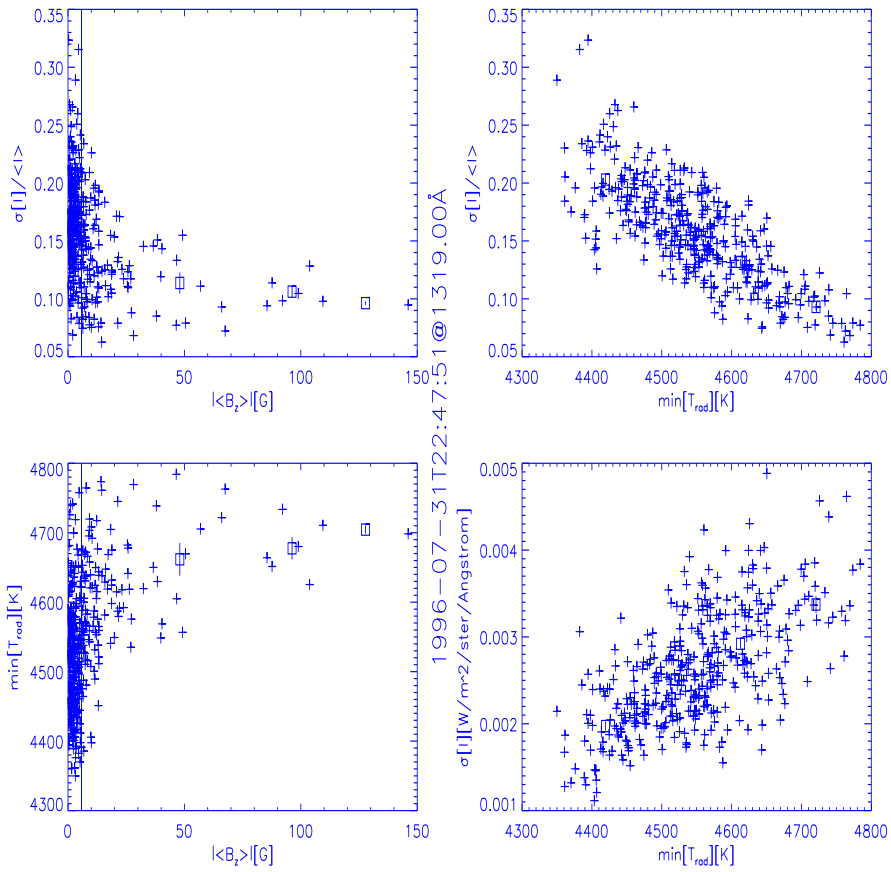

Figure 4.22: **Scatterplots at 1319Å from 31 jul (D).** See the figure text to figure 4.18 for explanations. Since this series does not have rotation compensation, each cross corresponds to 20 minute segments along each slit position.

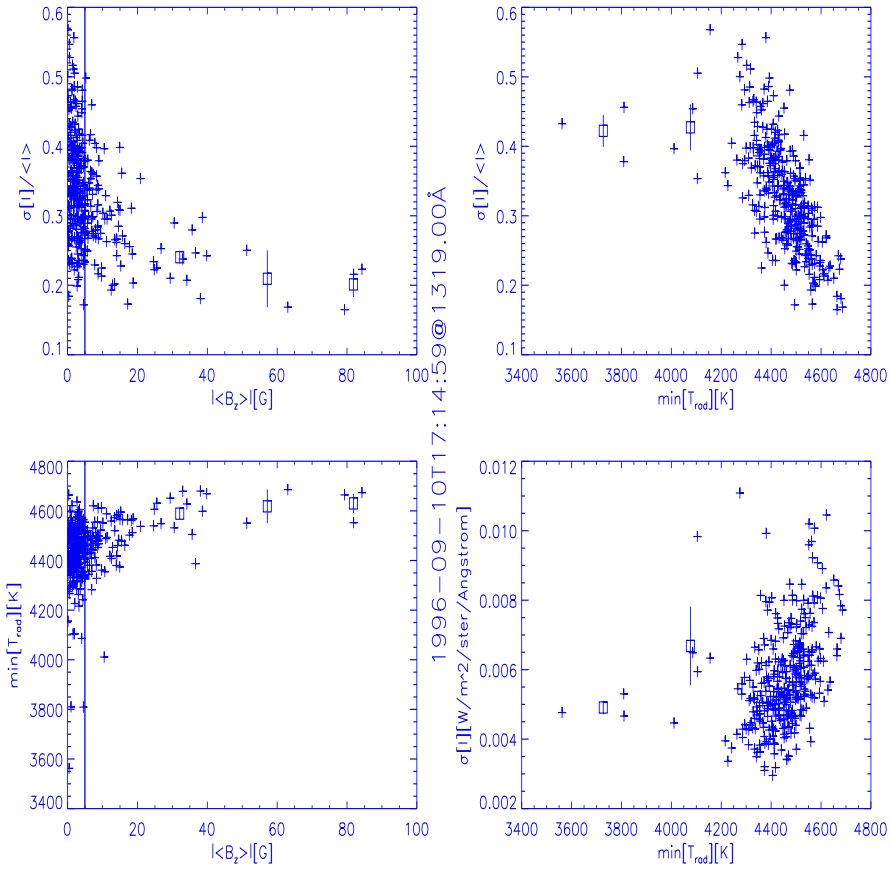

Figure 4.23: **Scatterplots at 1319Å from 10 sep (A).** See the figure text to figure 4.18 for explanations. Since this series does not have rotation compensation, each cross corresponds to 20 minute segments along each slit position.

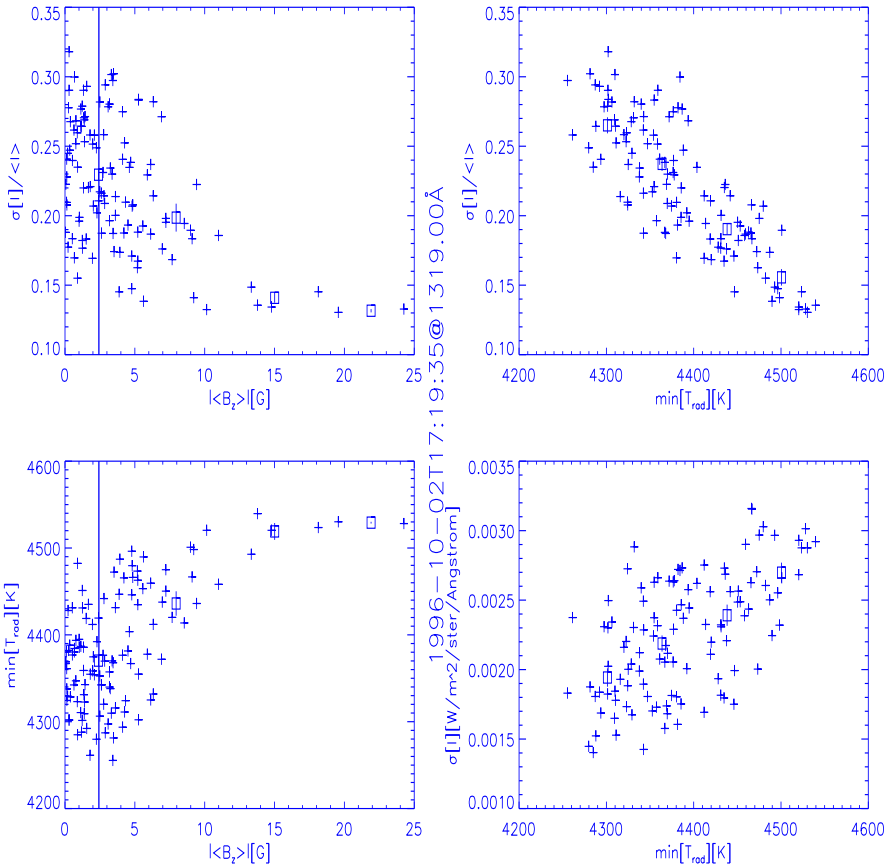

Figure 4.24: **Scatterplots at 1319Å from 02 oct (B).** See the figure text to figure 4.18 for explanations. Each cross corresponds to a slit position.

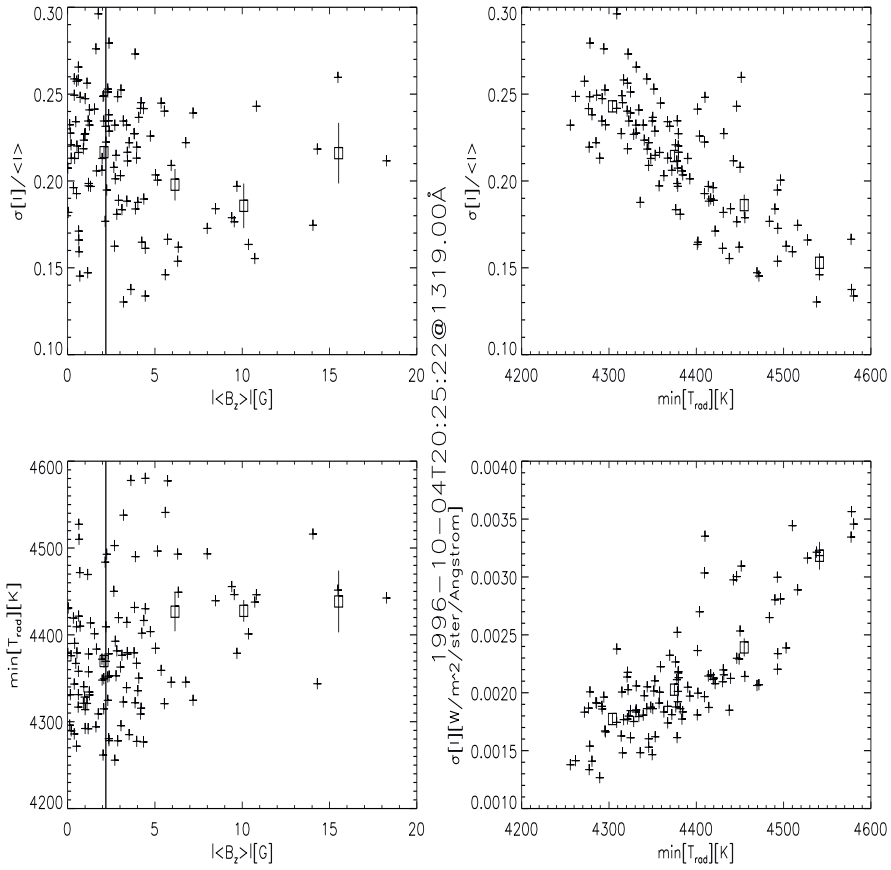

Figure 4.25: **Scatterplots at 1319Å from 04 oct (A).** See the figure text to figure 4.18 for explanations. Each cross corresponds to a slit position.

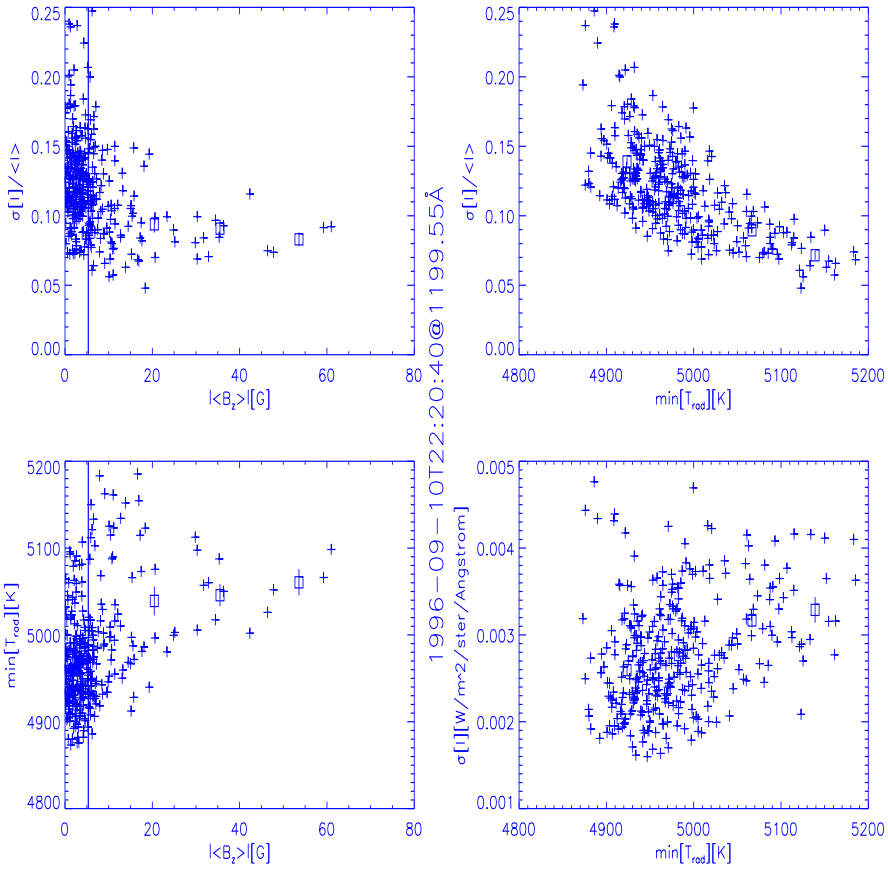

Figure 4.26: **Scatterplots at 1199Å from 10 sep (C).** See the figure text to figure 4.18 for explanations. Since this series does not have rotation compensation, each cross corresponds to 20 minute segments along each slit position.

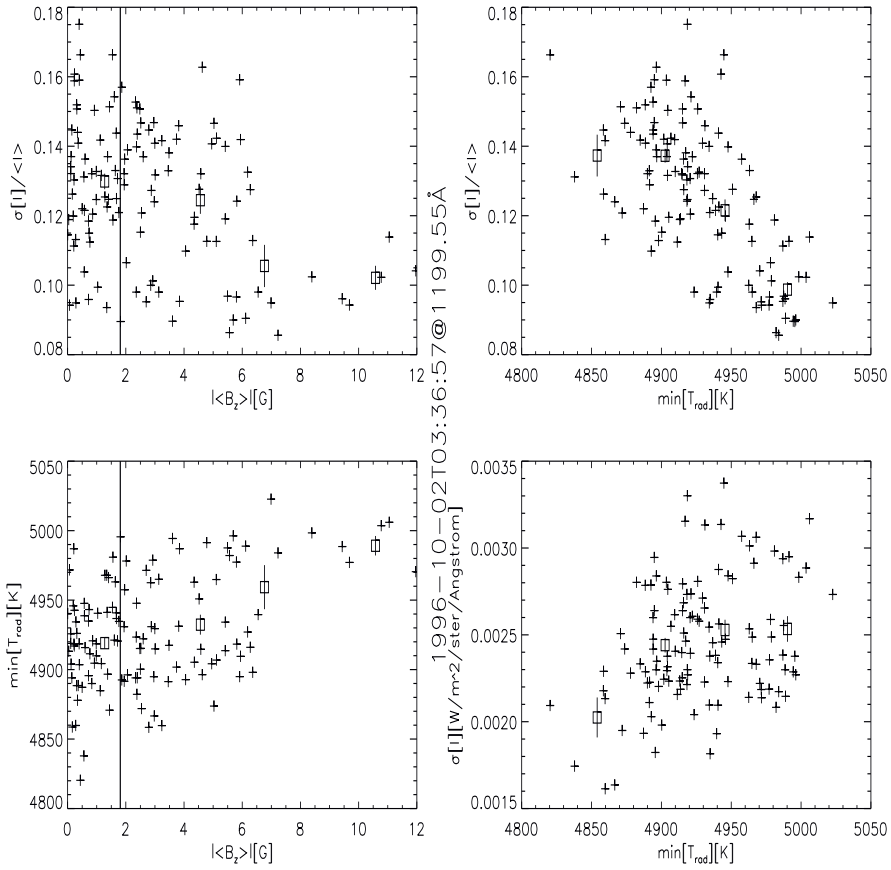

Figure 4.27: **Scatterplots at 1199Å from 02 oct (A).** See the figure text to figure 4.18 for explanations. Each cross corresponds to a slit position.

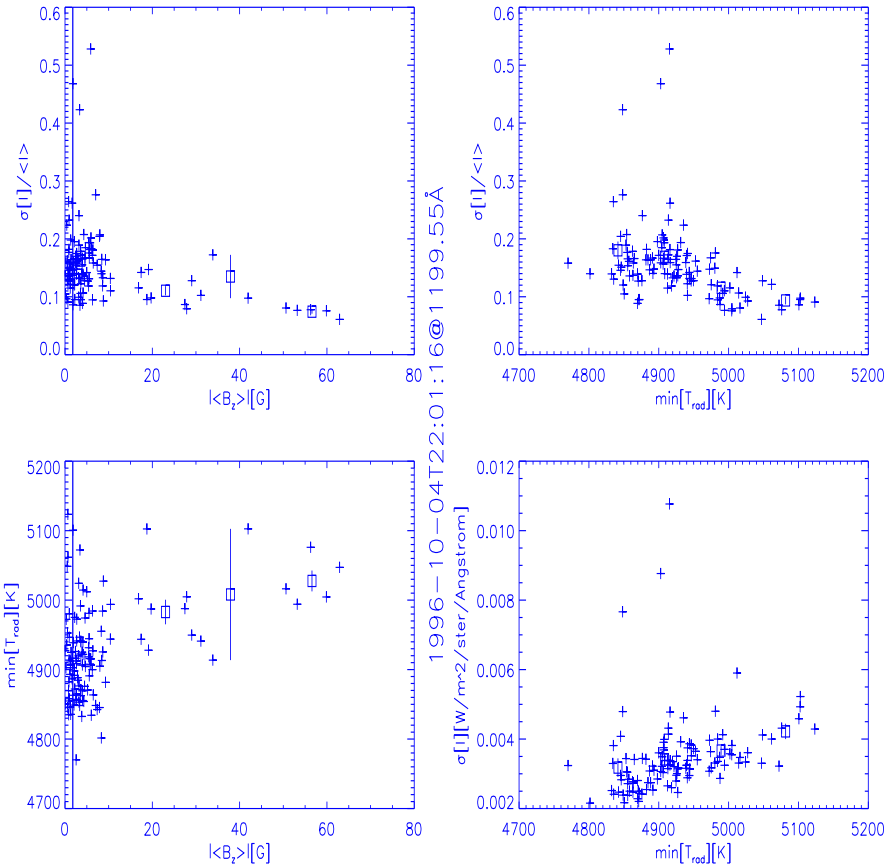

Figure 4.28: **Scatterplots at 1199Å from 04 oct (B).** See the figure text to figure 4.18 for explanations. Each cross corresponds to a slit position.

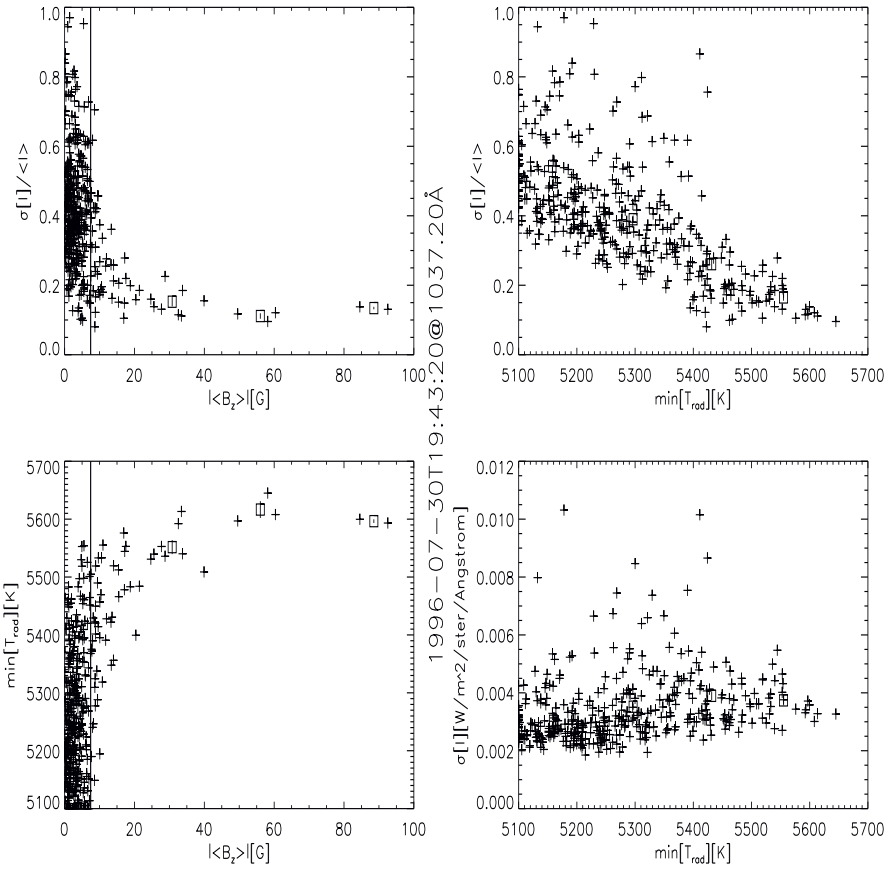

Figure 4.29: **Scatterplots at 1037Å from 30 jul (C).** See the figure text to figure 4.18 for explanations. Since this series does not have rotation compensation, each cross corresponds to 20 minute segments along each slit position.

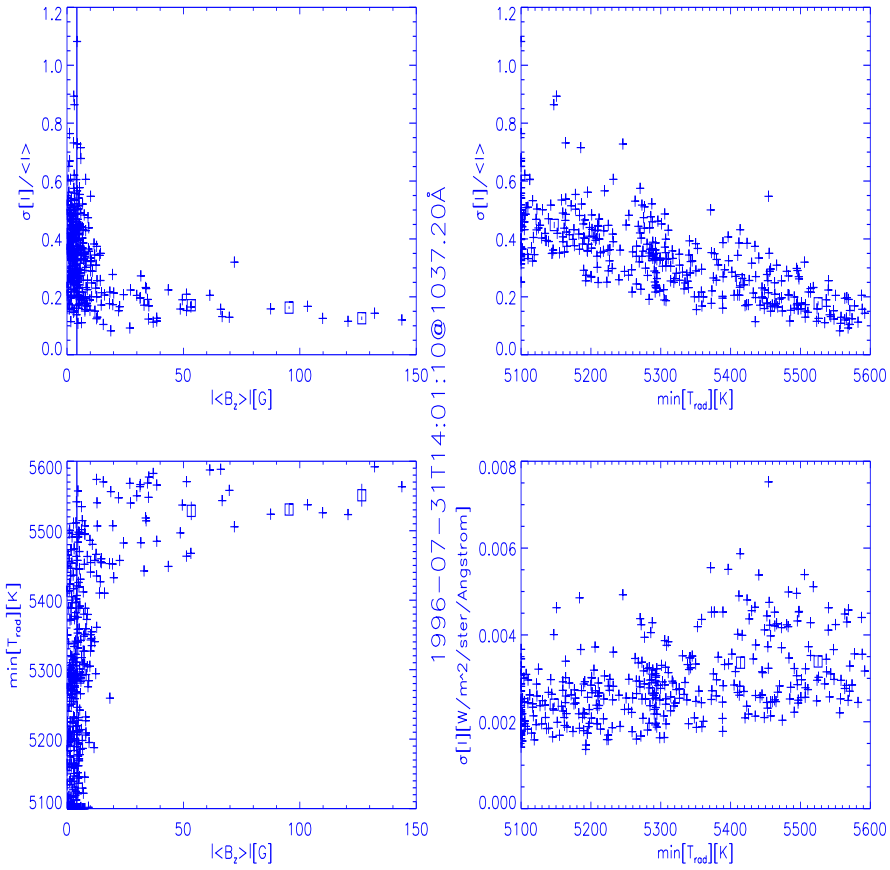

Figure 4.30: **Scatterplots at 1037Å from 31 jul (A).** See the figure text to figure 4.18 for explanations. Since this series does not have rotation compensation, each cross corresponds to 20 minute segments along each slit position.

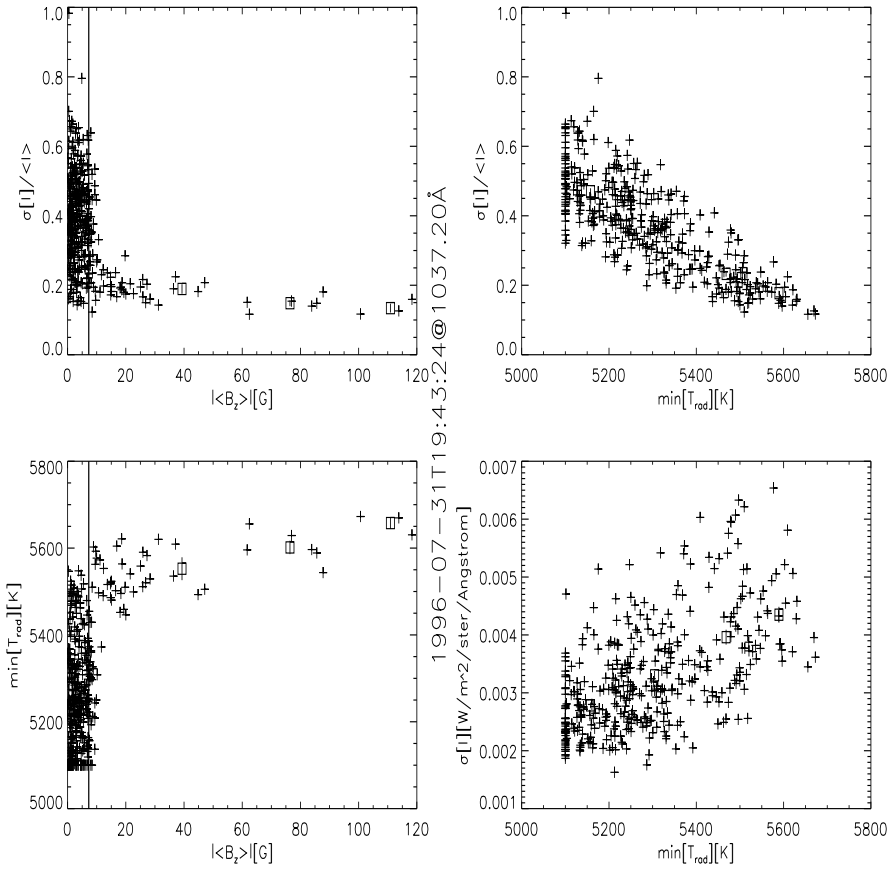

Figure 4.31: **Scatterplots at 1037Å from 31 jul (C).** See the figure text to figure 4.18 for explanations. Since this series does not have rotation compensation, each cross corresponds to 20 minute segments along each slit position.

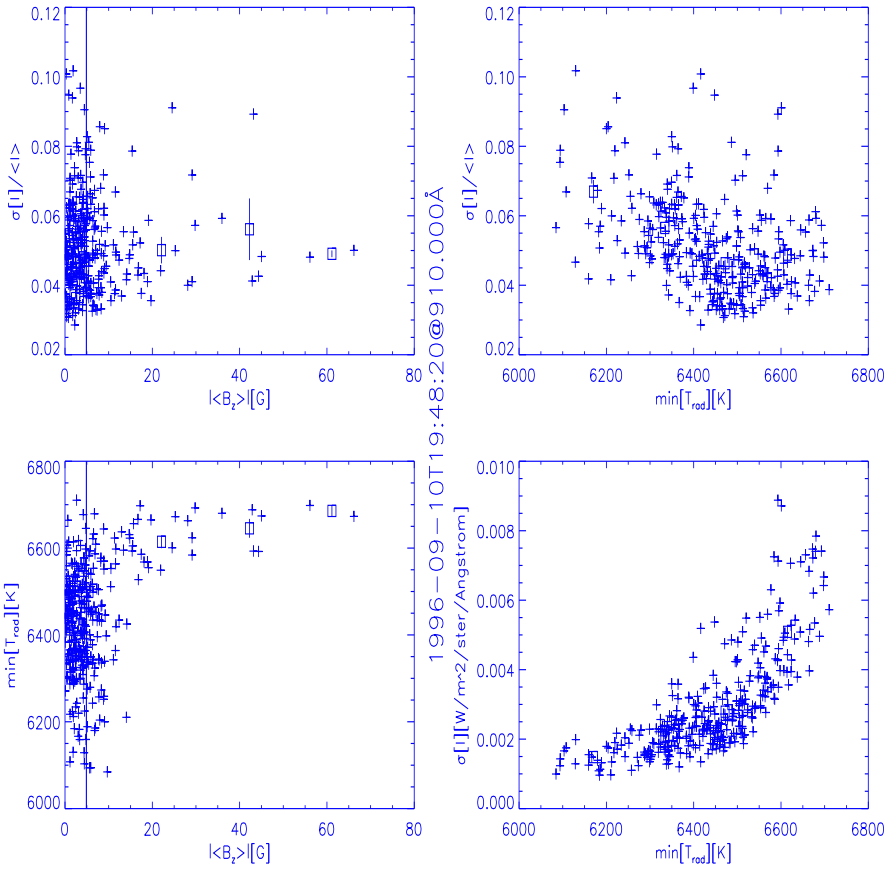

Figure 4.32: **Scatterplots at 910Å from 10 sep (B).** See the figure text to figure 4.18 for explanations. Since this series does not have rotation compensation, each cross corresponds to 20 minute segments along each slit position.

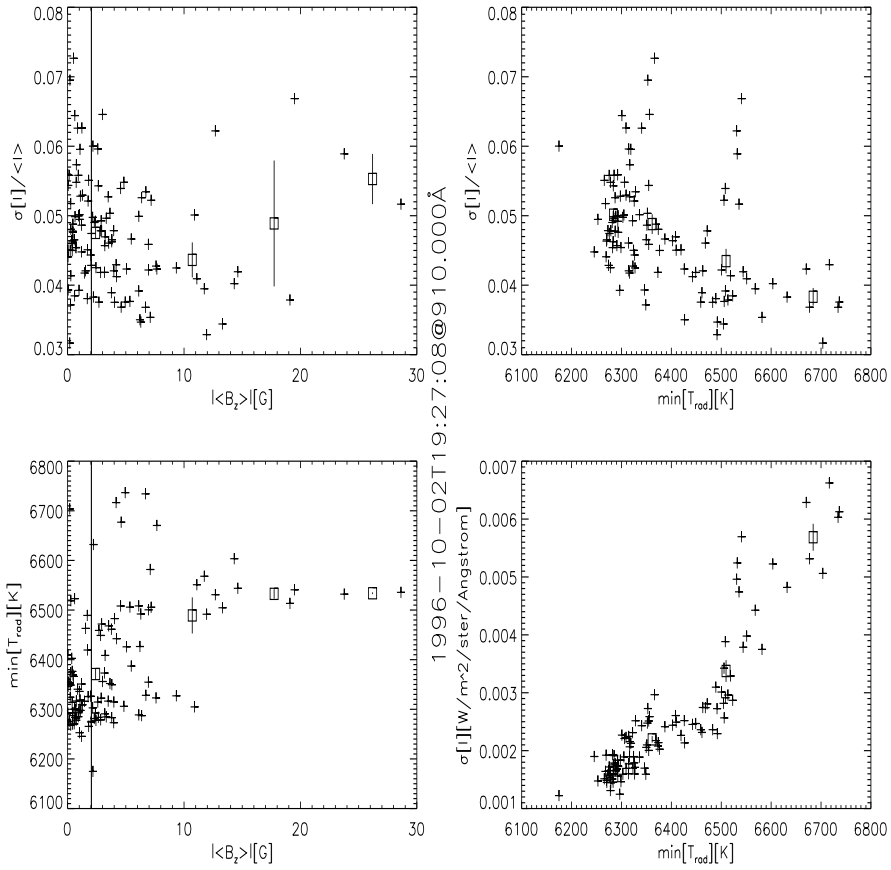

Figure 4.33: **Scatterplots at 910Å from 02 oct (C).** See the figure text to figure 4.18 for explanations. Each cross corresponds to a slit position.

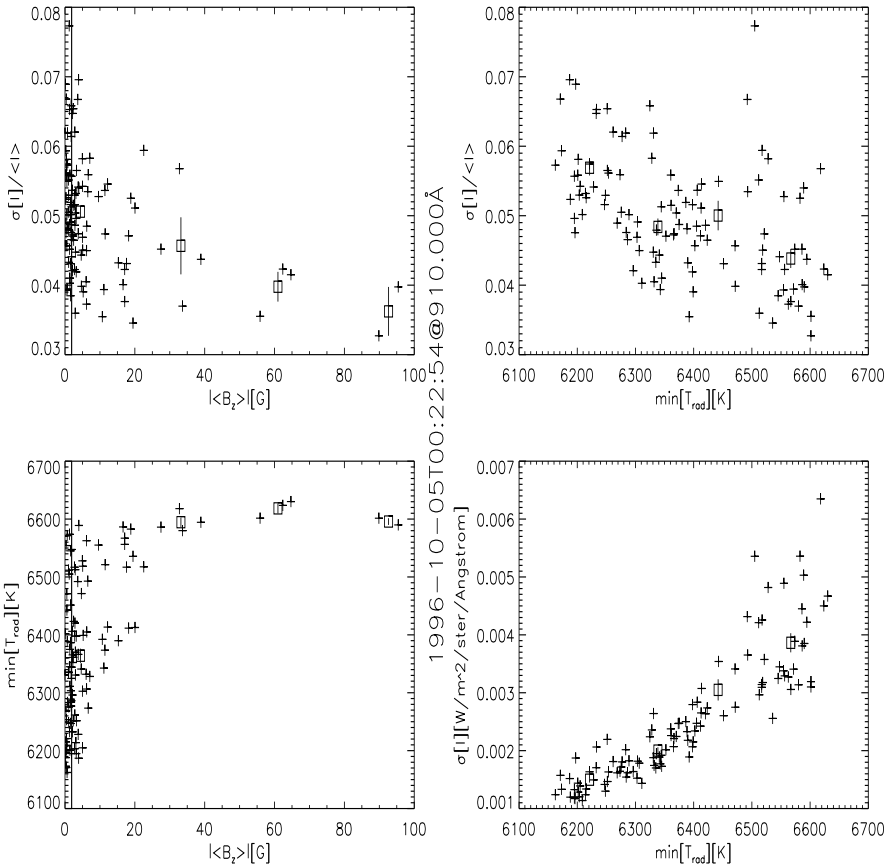

Figure 4.34: **Scatterplots at 910Å from 05 oct (A).** See the figure text to figure 4.18 for explanations. Each cross corresponds to a slit position.

4.3 Frequency and coherency

When I examined the connection between the oscillations in the photosphere, as observed in MDI doppler velocities, and the oscillations in the continuum radiation temperature (sec. 4.1.1, no figure of the doppler velocity available), I noticed that there was not a clear correlation between the two. I could not, just by looking at the data, see the same wave patterns in the chromosphere as I saw in the photosphere. To examine this closer, we decided to do an analysis of frequency and coherency. I described the frequency and coherency analysis method in section 3.2.5. The coherency is used to show phase persistence. The coherency plots are in figures 4.37 - 4.48.

4.3.1 Overview of the frequency and coherency results

1319Å

As I have done in the previous section, I will begin by looking at the data at 1319Å. The first dataset is 30 Jul (B), shown in figure 4.37. The upper left panel shows the summed counts of the intensity as a function of slit position. The intention is to indicate the locations of the network and internetwork. In this plot, I have identified two network elements. These are the spikes at 80-84″ and 183-197″ spatial position. If you compare these two positions, with figure 4.2 (upper left panel), you see that they correspond to the bright streaks at about 80″ spatial position and 0-4000s, and about 190″ spatial position and 2000-6000s in time. There are other bright elements, as you can see, but the summed counts are too low to single them out as network elements. The middle left panel, shows the squared coherency as an indicator of wave conservation. In other words, they show how much of the wave has preserved its shape since it left the photosphere and entered this region of the chromosphere. The brighter elements indicate that a large part of the wave has been preserved. It may also be helpful to compare with the lower left panel, when considering the coherency. The lower left panel shows the averaged squared coherency for the network and internetwork, as identified above. The continuous line is the network, and the dotted line is the internetwork. We notice especially that there is large coherency for frequencies below 2mHz in the network, or as we see in the middle panel, for spatial position 140-190″. We also notice that there is strong coherency, between 3-6mHz at spatial position 140-180″. The right side show the power frequency for the internetwork (upper panel) and network (lower panel). The dotted lines indicate where σ, 2σ and 3σ are, above which there is significant power. In the internetwork we find significant power between 3-7mHz, while in the network there is a power peak at 3mHz.

The next dataset is 30 Jul (D), shown in figure 4.38. In this plot, we see large coherency between spatial positions 60-120″, between 2-5mHz. This set is from approximately the same area on the sun, as 30 Jul (B), but five hours later. The frequency characteristics are the same as in the previous dataset.

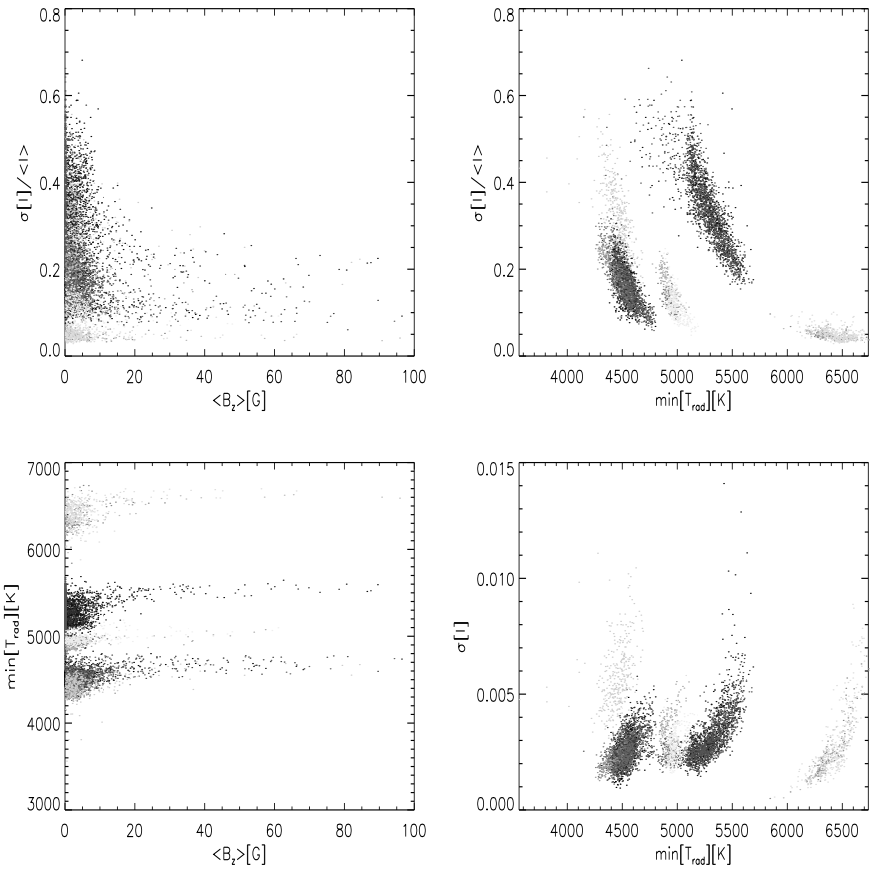

Figure 4.35: **Scatterplots of all datasets** See figure text of figure 4.19 for an explanation. In this figure all the figures 4.19 - 4.34 are plotted together. In the upper right panel the datasets at 1319Å are the points furthest to the left, i.e. around 4500K. The little cluster at 5000K are the points from 1199Å. The larger cluster at 5500K, are the points from 1037Å. The cluster furthest to the right, at 6500K, are the points from 910Å. This distribution is similar in the lower rightmost plot, and using the radiation temperature as an indicator, we recognise the different wavelengths, also in the lower leftmost plot, with 1319Å at the bottom and then 1199Å, 1037Å and 910Å. The different shades are to indicate data points from different timeseries. It is harder to separate the data points in the upper left plot, which is a composite of the upper right and the lower left plots.

The next dataset is 31 Jul (B), shown in figure 4.39. In this set, there are two network elements, which can be seen as the two maxima at 100″ and 170″ spatial position in the upper left side panel. In the coherency plot (middle leftside panel), we notice two dark lanes at about 100″ and 150″, which indicate little coherency between the continuum radiation temperature and doppler velocity.

The final dataset in July, is 31 Jul (D). This set does not show any strong coherency signal, and the frequency characteristics are the same as in the other July observations of the 1319Å continuum.

The next dataset is 10 Sep (A), shown in figure 4.40. In the upper left panel, we see 6 spikes, indicating that there are 6 network elements in the timeseries. The network identification routine says that 3 of these are networks, see lower right panel, at spatial position 0″, 37″ and 100″. If we compare this to figure 4.6, we see that the three network elements mentioned above are present throughout the timeseries, while the three other spikes seen in the summed counts window have shorter durations, which can be seen if you for example compare the spike at spatial position 80″ in the summed counts window with the intensity at the same spatial position at 1000-2000s, in the upper left panel of figure 4.6. If we look at the middle panel (squared coherency), we do not see very high values anywhere, except at spatial position 40-50″ and 65-80″, between 2-5mHz. In the lower left panel, notice that the averaged squared network coherency, is relatively high at 0-2mHz, which we also saw in figure 4.37. This is most likely an artifact of faulty data. The power frequency plots are somewhat different than what we have seen before. Notice that the power is about 1.0, while before it was up to 10.0. This is due to the weak signal. If we consider the upper right panel (internetwork), we see increased power at 0-2mHz and at 3-6mHz, as we saw earlier. The lower right panel shows the network. This is similar to what we have seen before, except that the strong power at about 3mHz is not seen.

We now turn to the October datasets of the 1319Å continuum. First is 02 Oct (B), shown in figure 4.41. We see at once, that this set has strong coherency (middle left panel) between 3-6mHz. The frequency plots, are similar to earlier datasets, except that we now have very strong power in the network, between 2-5mHz. This may be because of a poor identification of the network. If we compare with figure 4.7, we see that what is identified as network, could as well be identified as internetwork.

The final dataset at 1319Å, is 04 Oct (A). This dataset shows about the same characteristics as the other datasets.

1199Å

We now turn to the 1199Å data. The first dataset is 10 Sep (C), shown in figure 4.42. We see very little coherency in this plot (middle left panel). There seems to be some coherency at spatial position 90-100″, between 4-6mHz. The same coherency can be seen in the network, as shown in the lower left panel, which show an increase in coherency at 5-6 mHz, even though they are based on other

pixels (listed in lower right panel). The power frequency is similar to the 1319Å power frequency, except that we do not see the strong 3mHz oscillations in the network (lower right panel).

The next dataset is 02 Oct (A), see figure 4.43. In this dataset there is no clear separation between network and internetwork (upper left panel). We see four maxima, and if we compare with the intensity plot in figure 4.10, we see them as four white bands. The automatic routine selected a few pixels to identify the network and internetwork, spatial position 80-85″ and 106-114″ respectively. If we look at the lower left panel, we see that the coherency is strong for the network at 3-5mHz, and we also see high power in the power frequency for the network (lower right panel) at the same frequencies. The power frequency for the internetwork show strong power at 3-5mHz (upper right panel).

The last dataset is 04 Oct (B), shown in figure 4.44. The data show little coherency (middle left panel). We do see some white blobs at higher frequencies, 6-7mHz, at 15″ and 40″ spatial position, but these frequencies lie almost at the noise level, cf. power frequency plots on the right side.

1037Å

The 1037Å datasets are very noisy, i.e. poor signal-to-noise ratio. The first dataset is 30 Jul (C), shown in figure 4.45. We see little or no coherency for this dataset, see middle left panel. Notice that the power frequency has changed from the previous datasets at 1319Å and 1199Å. The internetwork (upper right panel) has little power above 2mHz, it is all noise, and the network shows a decay in power with increasing frequency, see lower right panel, up to 6mHz where it becomes part of the noise.

The other two datasets at 1037Å are similar (31 Jul (A) and 31 Jul (C)).

910Å

We now compare the coherency between the continuum radiation temperature and the doppler velocity with a separation of 1.8Mm, which means that the waves have passed through most of the chromosphere. If we look at the first dataset, which is 10 Sep (B), shown in figure 4.46, we see a dip in the coherency at 2mHz (lower left panel). This dip is evident if you compare with the other datasets at 910Å (02 Oct (C) and 05 Oct (A), figures 4.47 and 4.48, respectively). I do not see it in any other coherency plot. The power frequency shows some of the same characteristics as the 1037Å data, a decay in power with increasing frequency (right side panels).

The next dataset is 02 Oct (C), shown in figure 4.47. As already mentioned, we have the dip at 2mHz in the squared coherency plots. We also notice that there is relatively strong coherency above this dip, at 5mHz.

The last dataset is 05 Oct (A), shown in figure 4.48. This dataset is similar to the other two 910Å datasets, but notice especially the bright blob at 35″ spatial position and 5mHz in the middle leftside panel.

4.3.2 Summary of the frequency and coherency results

Significant coherency ($C^2 > 0.5$) can be seen in the 1319 and 1199Å data, see e.g. figs. 4.37 and 4.43, but not in the 1037 and 910Å data, see e.g. figs. 4.45 and 4.46.

The frequency characteristics are also different for the two sets of continua. The 1319/1199Å sets show strong power between 2 and 6 mHz, e.g. figures 4.39 and 4.42, but the 1037/910Å datasets show an exponential decay of the power with frequency, see figures 4.45 and 4.48.

λ (Å)	Date	T_{rad} (K)		$\sigma(I)$		$\frac{\sigma(I)}{<I>}$		$\lvert<B_z>\rvert_{max}$ (G)
		min	max	min	max	min	max	
1319	30 Jul (B)	4400	4800	0.001	0.005	0.08	0.25	50
	30 Jul (D)	4400	4700	0.002	0.004	0.10	0.25	80
	31 Jul (B)	4400	4800	0.001	0.004	0.10	0.30	150
	31 Jul (D)	4400	4700	0.001	0.004	0.08	0.25	150
1319	10 Sep (A)	4300	4700	0.003	0.009	0.15	0.50	80
	02 Oct (B)	4350	4500	0.001	0.003	0.15	0.30	20
	04 Oct (A)	4250	4600	0.001	0.003	0.15	0.25	15
1199	10 Sep (C)	4850	5200	0.002	0.004	0.05	0.20	60
	02 Oct (A)	4850	5000	0.002	0.003	0.08	0.16	10
	04 Oct (B)	4850	5100	0.003	0.005	0.10	0.25	50
1037	30 Jul (C)	5100	5600	0.001	0.007	0.15	0.50	70
	31 Jul (A)	5100	5600	0.001	0.006	0.15	0.50	130
	31 Jul (C)	5100	5600	0.001	0.006	0.15	0.60	90
910	10 Sep (B)	6100	6700	0.001	0.007	0.03	0.08	60
	02 Oct (C)	6250	6700	0.001	0.006	0.03	0.07	15
	05 Oct (A)	6200	6600	0.001	0.005	0.03	0.07	60

Table 4.1: **Overview of data values from scatterplots** In this table I have gathered some of the datavalues from the correlation analysis in section 4.2. λ is the observed wavelength. Date is the observation date. T_{rad} is the radiation temperature, given by minimal and maximal value. $\sigma(I)$ is the oscillation amplitude. $\sigma(I)$ is measured in W m^{-2} ster^{-1} Ångström^{-1}. $\frac{\sigma(I)}{<I>}$ is the relative oscillation amplitude. $\lvert<B_z>\rvert_{max}$ is the maximum value of the vertical photospheric magnetic field.

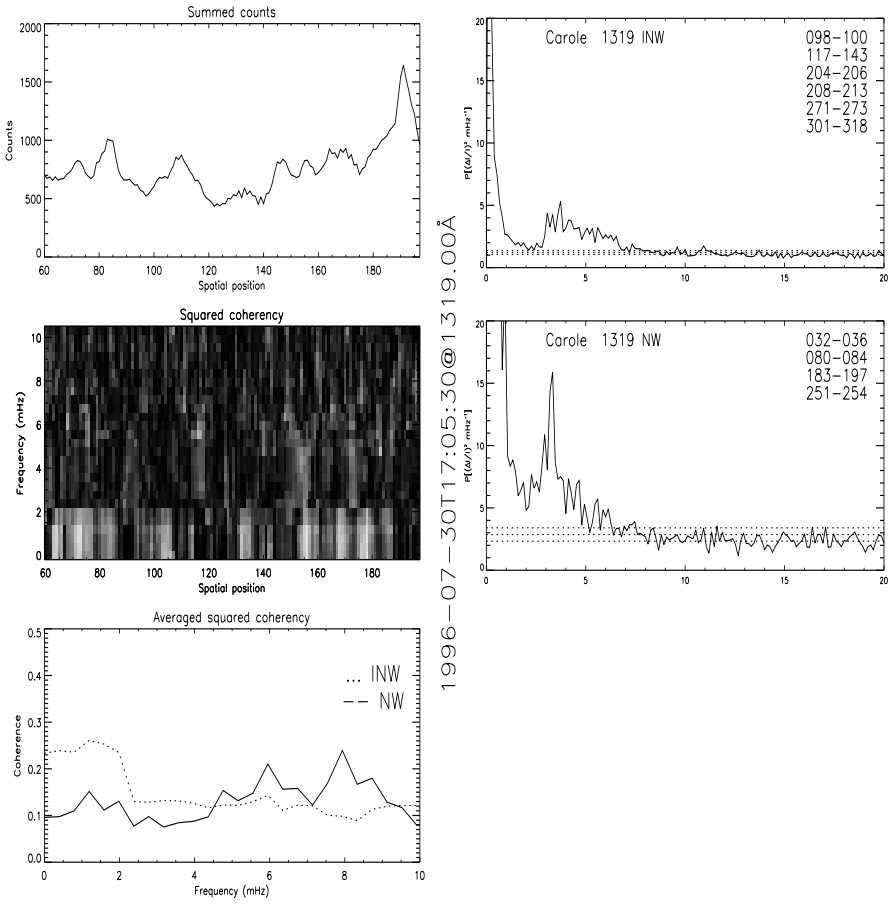

Figure 4.36: **Example of coherency between the photospheric doppler velocities and chromospheric continuum intensities.** (This figure is made from the same dataset as in figure 4.37). The upper left plot is the summed intensity counts as a function of slit position. This is useful to separate between the network and internetwork. The middle left panel shows the coherency squared as a function of slit position. The bright blobs correspond to high coherency (> 0.5). The lower left panel shows the averaged coherency as a function of frequency, split into network (NW) and internetwork (INW). The right side shows the power frequency of the continuum intensity in the network (lower right) and internetwork (upper right). The numbers in the upper right corner of the frequency plots, indicate the spatial pixels used to identify the internetwork and network. The dashed lines indicate σ, 2σ and 3σ, i.e. the noise level. (NW=network, INW=internetwork)

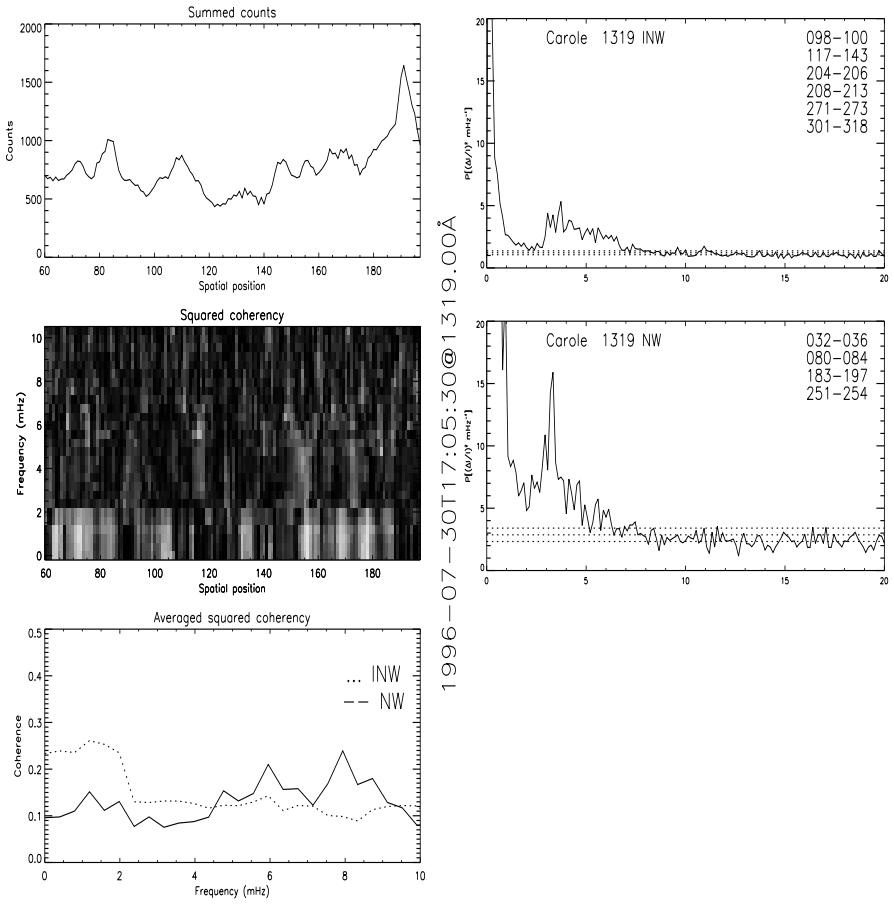

Figure 4.37: **Coherency between the photospheric doppler velocities and chromospheric continuum intensities for 30 Jul (B).** See the figure text to figure 4.36 for explanations.

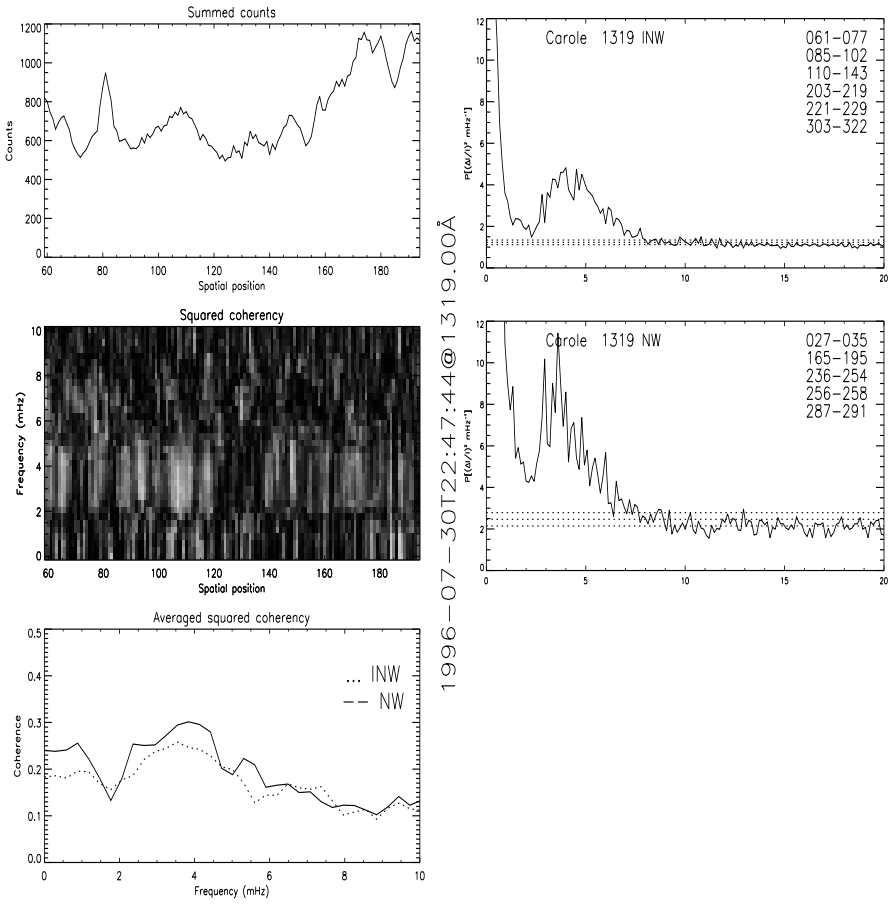

Figure 4.38: **Coherency between the photospheric doppler velocities and chromospheric continuum intensities for 30 Jul (D).** See the figure text to figure 4.36 for explanations.

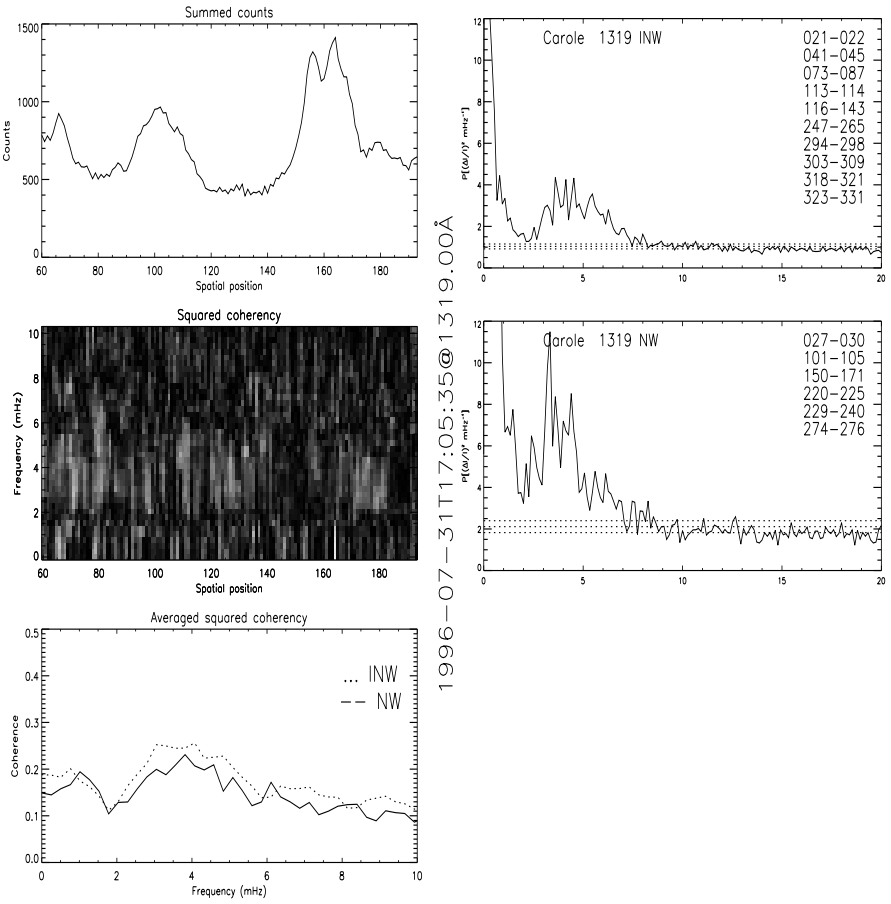

Figure 4.39: **Coherency between the photospheric doppler velocities and chromospheric continuum intensities for 31 Jul (B).** See the figure text to figure 4.36 for explanations.

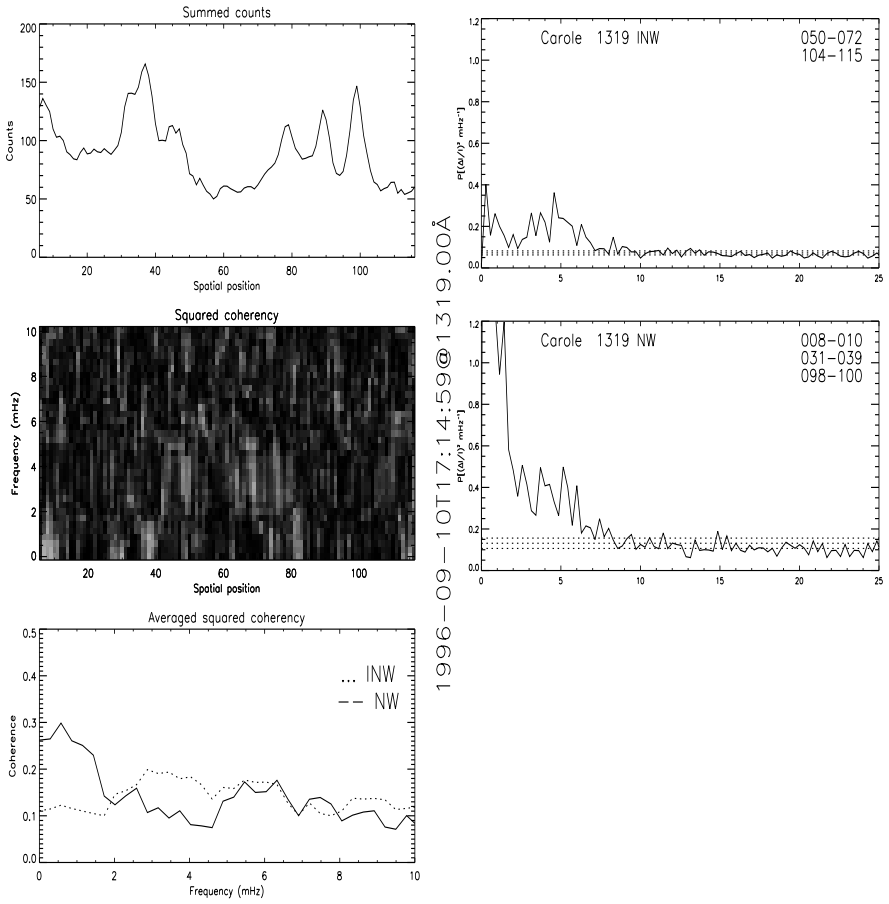

Figure 4.40: **Coherency between the photospheric doppler velocities and chromospheric continuum intensities for 10 Sep (A).** See the figure text to figure 4.36 for explanations.

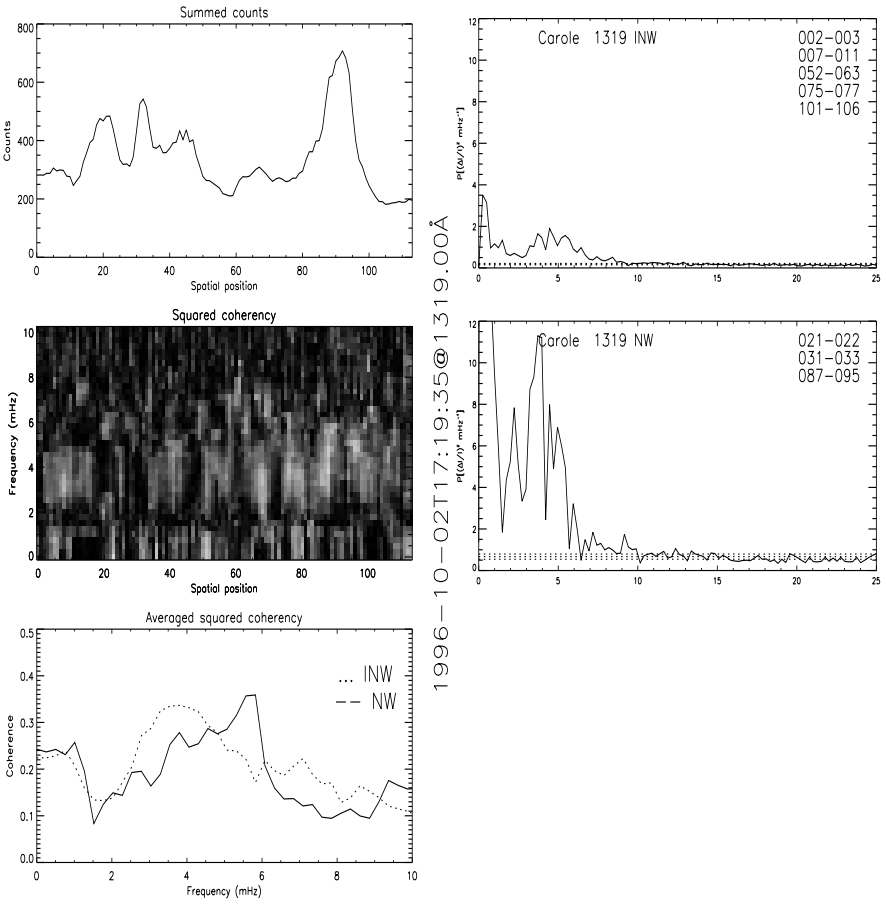

Figure 4.41: **Coherency between the photospheric doppler velocities and chromospheric continuum intensities for 02 Oct (B).** See the figure text to figure 4.36 for explanations.

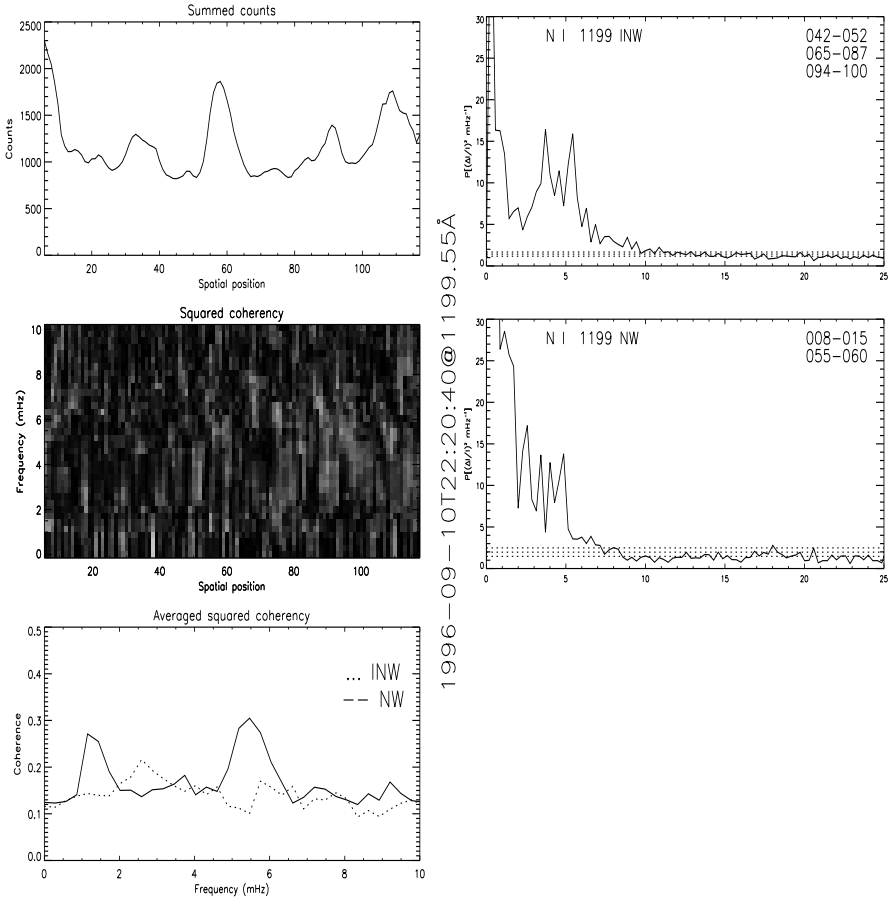

Figure 4.42: **Coherency between the photospheric doppler velocities and chromospheric continuum intensities for 10 Sep (C).** See the figure text to figure 4.36 for explanations.

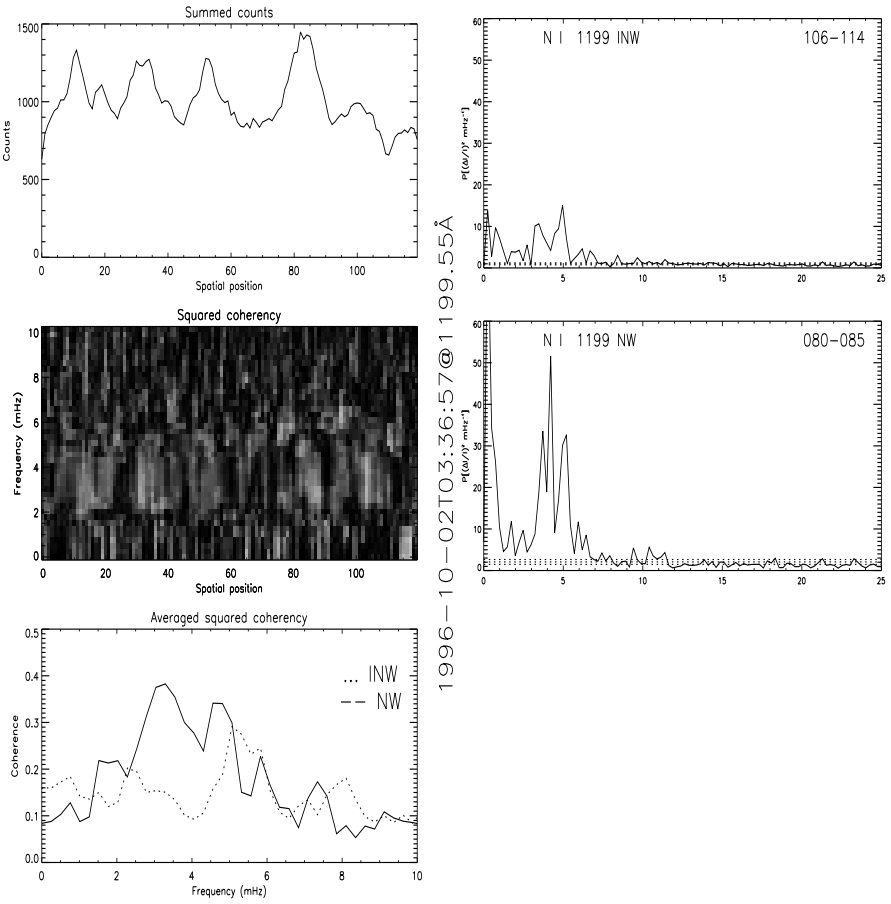

Figure 4.43: **Coherency between the photospheric doppler velocities and chromospheric continuum intensities for 02 Oct (A).** See the figure text to figure 4.36 for explanations.

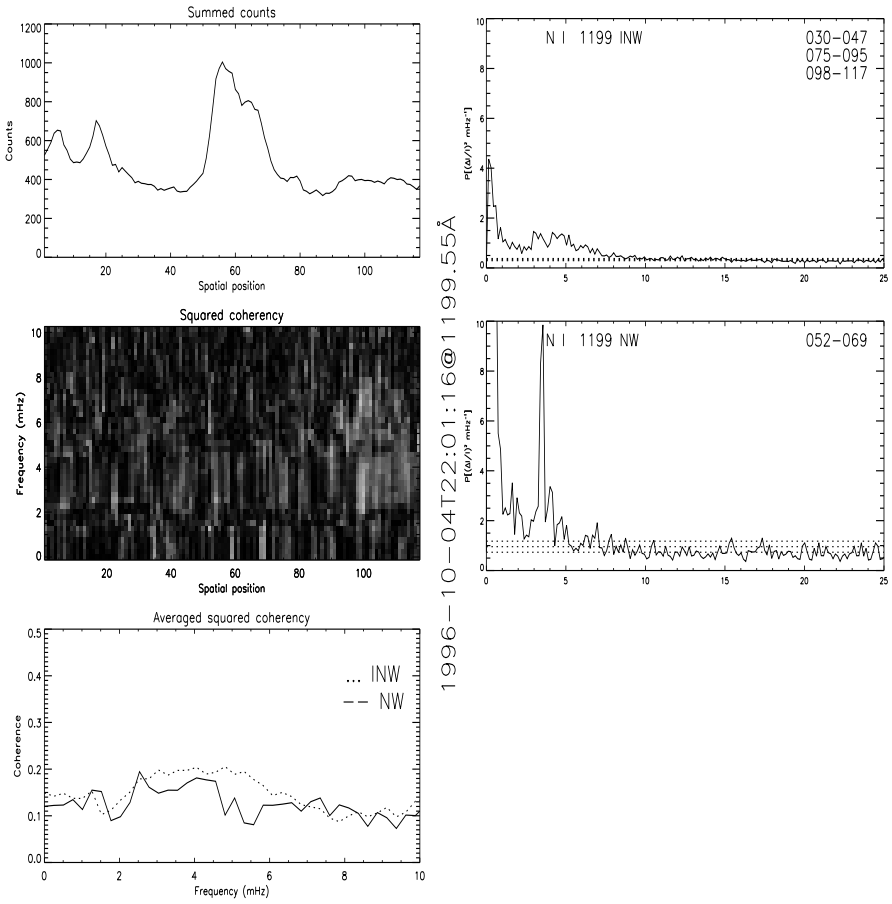

Figure 4.44: **Coherency between the photospheric doppler velocities and chromospheric continuum intensities for 04 Oct (B).** See the figure text to figure 4.36 for explanations.

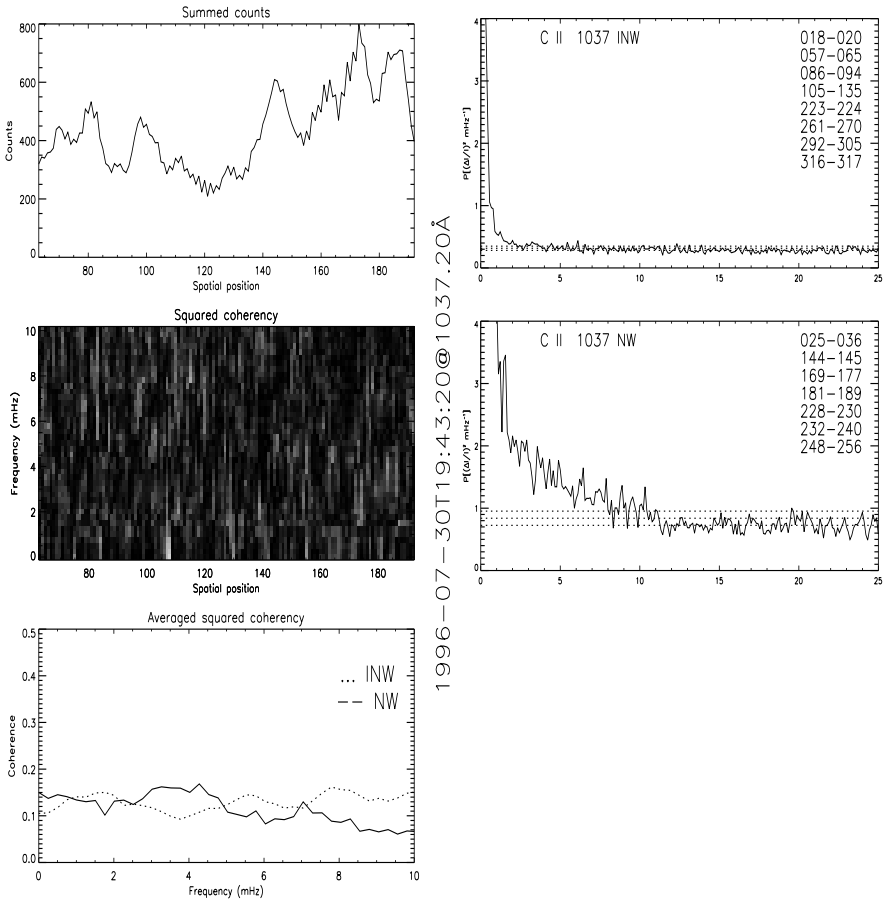

Figure 4.45: **Coherency between the photospheric doppler velocities and chromospheric continuum intensities for 30 Jul (C).** See the figure text to figure 4.36 for explanations.

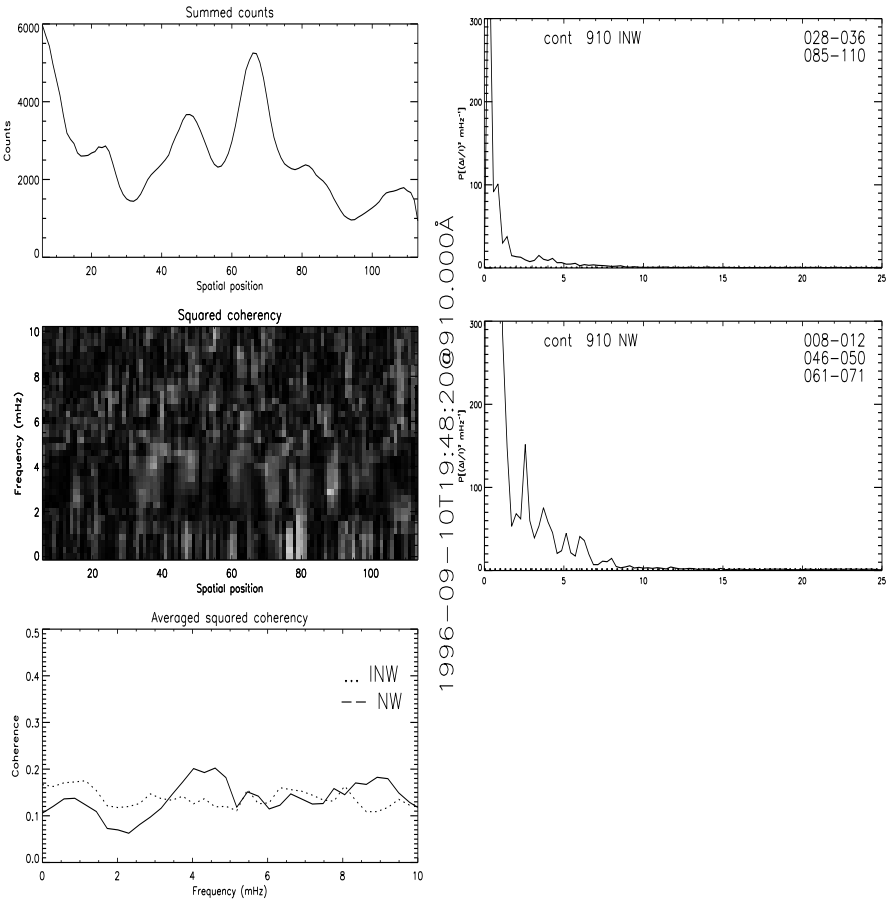

Figure 4.46: **Coherency between the photospheric doppler velocities and chromospheric continuum intensities for 10 Sep (B).** See the figure text to figure 4.36 for explanations.

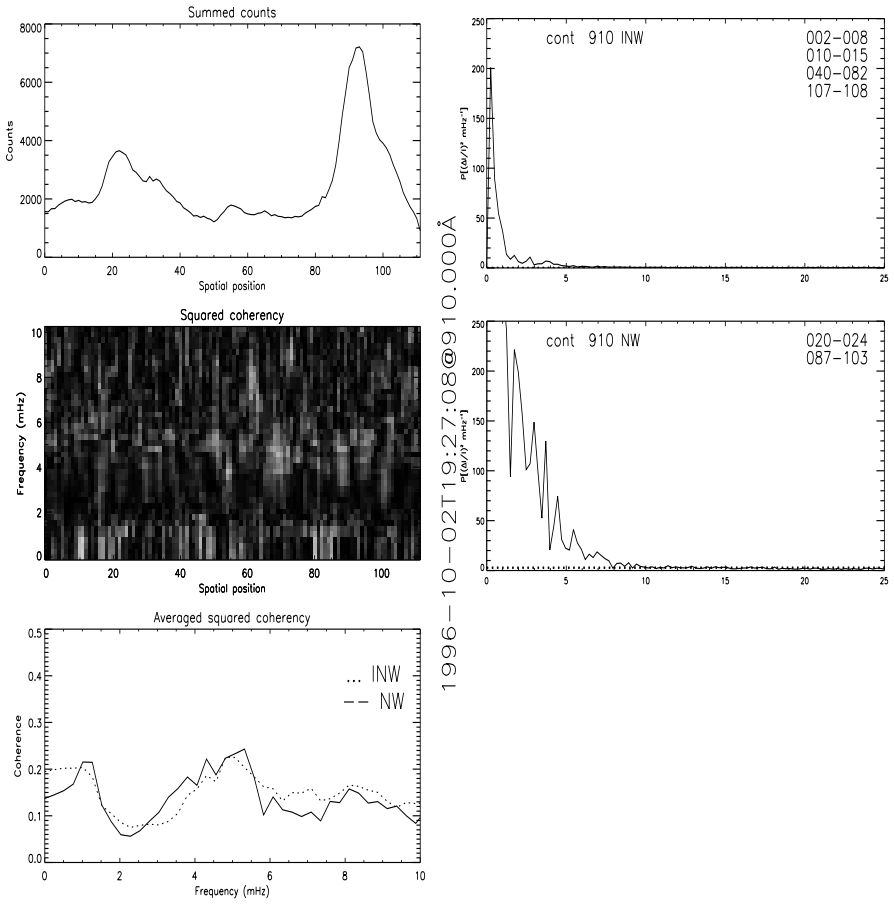

Figure 4.47: **Coherency between the photospheric doppler velocities and chromospheric continuum intensities for 02 Oct (C).** See the figure text to figure 4.36 for explanations.

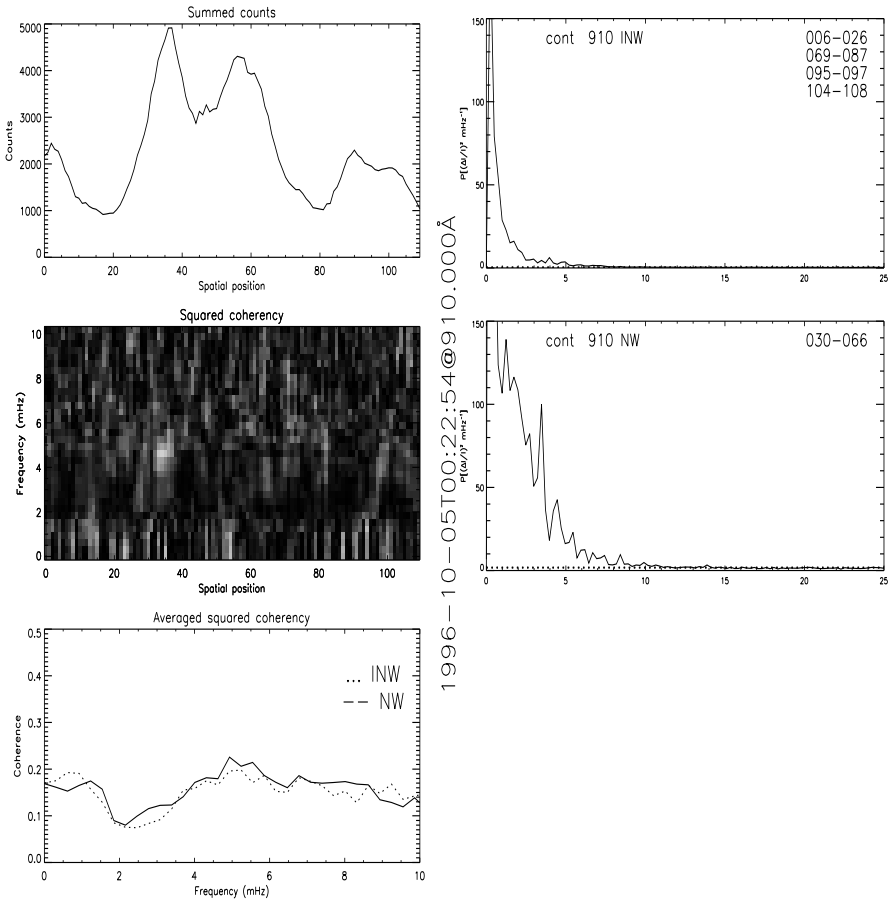

Figure 4.48: **Coherency between the photospheric doppler velocities and chromospheric continuum intensities for 05 Oct (A).** See the figure text to figure 4.36 for explanations.

Chapter 5

Discussion and conclusion

I charge thee [...] that thou observe these things without preferring one before another, doing nothing by partiality.

The First Epistle of Paul the Apostle to Timothy 5,21

In this chapter I will begin by commenting on the copointing method I have used. Then, I will discuss some of the central results obtained in this thesis. Since we also wish to combine this work with numerical simulations, I will show some possibilities on how the results can be used.

5.1 On precision

5.1.1 The copointing method

How successful was the copointing method developed in this thesis? We have at least two indicators of the accuracy of the copointing. The first is the visual impression, does it look like the data from SUMER and MDI are similar? The second is the correlation between the continuum intensity and the magnetic field.

To estimate the copointing visually, we can use the copointing figures, figs. 4.2 - 4.17. The general impression from these figures, is that we have developed a very good copointing method. The right side panels of the figures, all are similar with regards to prominent features, like for example the correlation between the bright intensity elements and the strong magnetic fields. An alternative to using the timeseries to assess the copointing, is to use the rasters together with the magnetograms, as in figure 3.2. This was after all the primary method we used to align the datasets. Some problems with this approach are mentioned in section 3.2.3.

The second method, is to use the scatterplots I have made in figures 4.19 - 4.34. It is only the left side panels which apply, since the right side panels only use the SUMER data, and therefore are not an indicator of the copointing. To measure the impact of uncertainties in the copointing, I varied the coordinate shifts between the SUMER and MDI data. The results indicated that I could vary the coordinates by as much as $\pm 3''$ without affecting the correlation significantly.

The downside with the copoint method we use, is that it requires a raster to align the SUMER and MDI data. A scan through the currently available SUMER data, shows that rasters are available only for March through October in 1996 and three datasets in February and May of 1998.

5.2 The central results

In this thesis, I wanted to study how the magnetic field affects the intensity in the chromosphere. Further, we hope that it may serve as a help to include the magnetic field in the simulation code of the atmosphere of the sun that is being developed at the institute.

The initial approach was to see if we could detect any similar features in the timeseries data of the continuum radiation temperature and the photospheric vertical magnetic field component. We saw in the previous chapter, that the brightness of the intensity was strongly correlated with the magnetic field strength. This is a well known result, see for example Skumanich et al. (1975). We have extended

this correlation down to the detection limit of MDI, that is to say that we see a strong correlation between the continuum intensity and the magnetic field all the way down to about 3G, see for example the lower left panel of figure 4.24.

Further, we tried to analyse the correlation between the intensity oscillations and the radiation temperatures, to see how the grain structure is altered in the presence of strong magnetic fields. We saw an increase in absolute intensity oscillations, and a decrease in relative intensity oscillations, for example as seen in figure 4.24. To study the coupling between the magnetic field and the continuum intensity, numerical simulations are necessary. Simulations would necessarily have to replicate this behaviour to be valid representations of real world situations.

We also tried to connect the grain structure in the continuum intensity with the doppler velocities in the photosphere, through the use of coherency analysis. The results indicate good coherency between the 1319Å continuum and the photospheric doppler velocities, and the 1199Å continuum and the photospheric doppler velocities. It is not clear how the network and internetwork affects the coherency, whereas Lites et al. (1993) observe differences between the network and internetwork with regards to coherency. The frequency analysis showed that the power profiles of the 1319Å and 1199Å continuum were similar, with strong power around 3-6mHz in the internetwork, and around 3mHz in the network. The power profiles of 1037Å and 910Å were also similar, but they showed exponential decay with increasing frequency, without any clear peaks in the signal.

5.2.1 Using the magnetic field at the formation height of the continuum

In the scattergrams, I have used B_z, the photospheric vertical component of the magnetic field. But what if I instead compared with the extrapolated magnetic field, $|\vec{B}|$, at the formation height of the observed continuum? This is what I have done in figure 5.1 (for 02 Oct (C)). This makes the points with high radiation temperature but weak magnetic fields move to areas with stronger magnetic fields, giving a more linear look to the plots. This indicates a better correlation between the magnetic field and the continuum radiation temperature.

To understand this, look at figure 4.17. From the timeseries plots, we see that the continuum radiation temperature is smoothed, and has no sharp boundaries, while the magnetic field is confined to narrow regions. When we instead look at the magnetic field at the formation height of the continuum, it also starts to smooth out, giving a better correlation. Consider for example the continuum radiation temperature at slit position 30, it is rather large. But, the magnetic field is dominated by noise, and does not become significant before reaching slit position 34. This would show up as a point at, e.g. (6650K, 2G), in the upper plot of figure 5.1. But when we use the magnetic field *at formation height*, the magnetic field at slit position 30 has increased in strength, and the point in our plot has moved to the right, i.e. moved to a higher $|\vec{B}|$. This is the reason we get a stronger correlation with the extrapolated magnetic field at formation height.

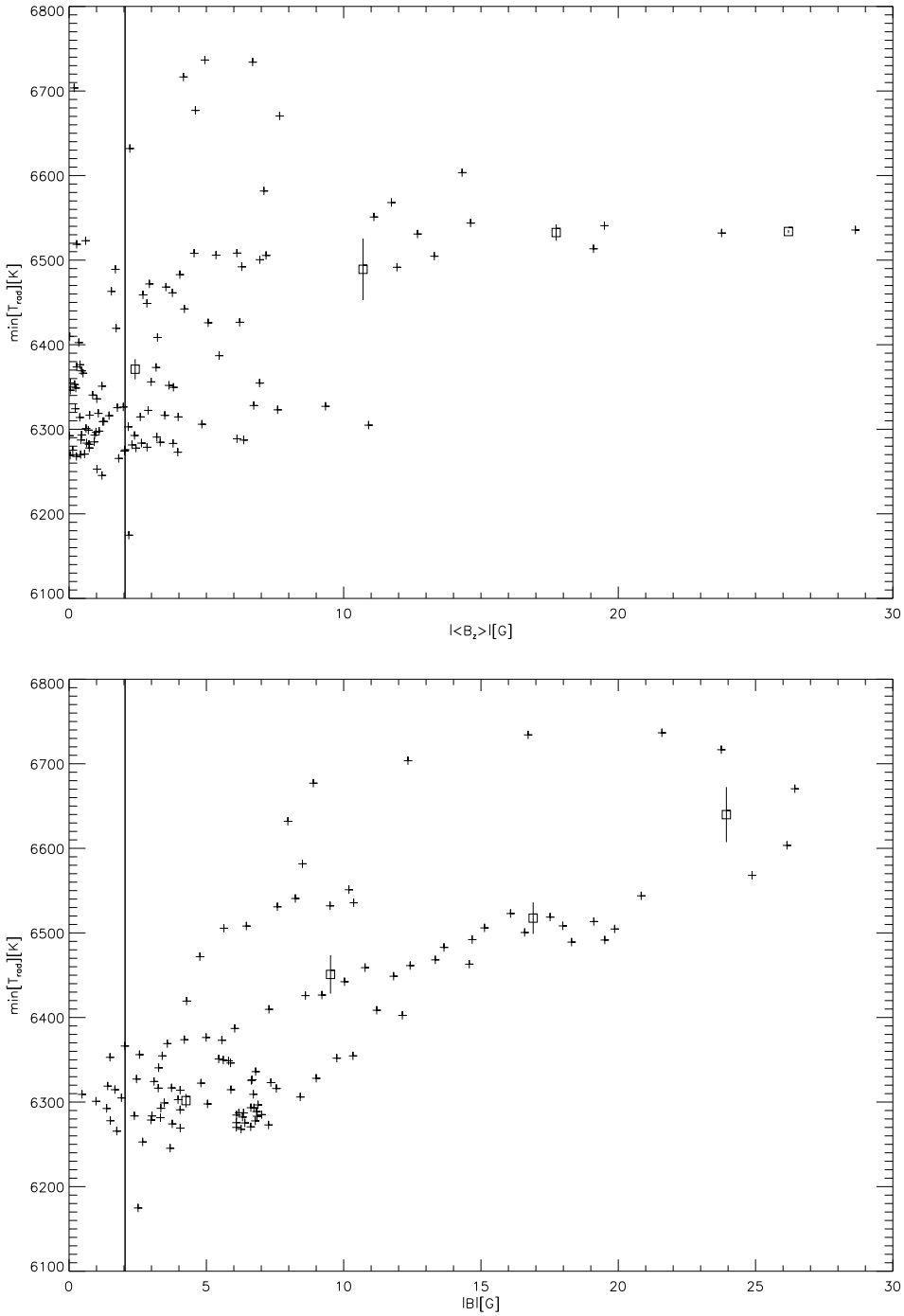

Figure 5.1: **Plots of the radiation temperature as a function of magnetic field strength for 02 Oct (C).** In the upper plot the magnetic field is given at the photosphere as observed by MDI. In the lower plot the potential field extrapolated magnetic field is given at the formation height of the 910Å continua, at about 1.8Mm. *Note the differences in scatter.*

5.3 Future work

5.3.1 The potential for comparisons with numerical simulations

I mentioned that some of the rationale for this thesis, was to create a basis for extending the numerical simulation code created by Carlsson and Stein (1992, 1996 & 1997) to include magnetic fields.

To compare the current numerical simulations without magnetic fields to the observations with magnetic fields, I have plotted the histograms of the radiation temperatures at the locations where the MDI measured magnetic field is below the detector limit, i.e. below 5G, which is equivalent to no magnetic field, or a low filling factor (Judge et al. 2001). The plot is shown in figure 5.2. This will enable us to do a statistical analysis of the numerical data, which can be compared with the observational data.

Inclusion of the magnetic fields in the numerical code?

What can be said about how to include the magnetic field in the numerical code? The results indicate, that we may include the magnetic field in two ways. The first is as a heating factor. The presence of a magnetic field, seems to increase the radiation temperature in the chromosphere. The second is some kind of coupling to the intensity oscillations. It is unclear how to do this.

5.4 Conclusion

5.4.1 Does the magnetic field contribute to the dynamics of the chromosphere?

I set out at the beginning of this thesis to investigate the connection between the magnetic field and the chromosphere. Based on magnetic field extrapolations from the photospheric line of sight magnetic field component, and observations of the intensity in the chromosphere at different heights. Careful analysis of these data, showed how the radiation temperature of the chromosphere is strongly correlated to the magnetic field. Even weak fields seem to result in an increase in radiation temperature. It is not clear how or indeed if the magnetic field has some influence on the wave motions, other than the wave mode conversion at the $\beta = 1$ magnetic field canopy. There is a clear observational difference in wave characteristics, below and above this level.

Further study with numerical simulations are necessary for an understanding of the physics behind and an interpretation of the observations. This thesis may serve as a help for focusing that research, since it contains an analysis of a considerable amount of data sampled from several strategically, with regards to the relevance of the processes it samples, selected heights in the chromosphere.

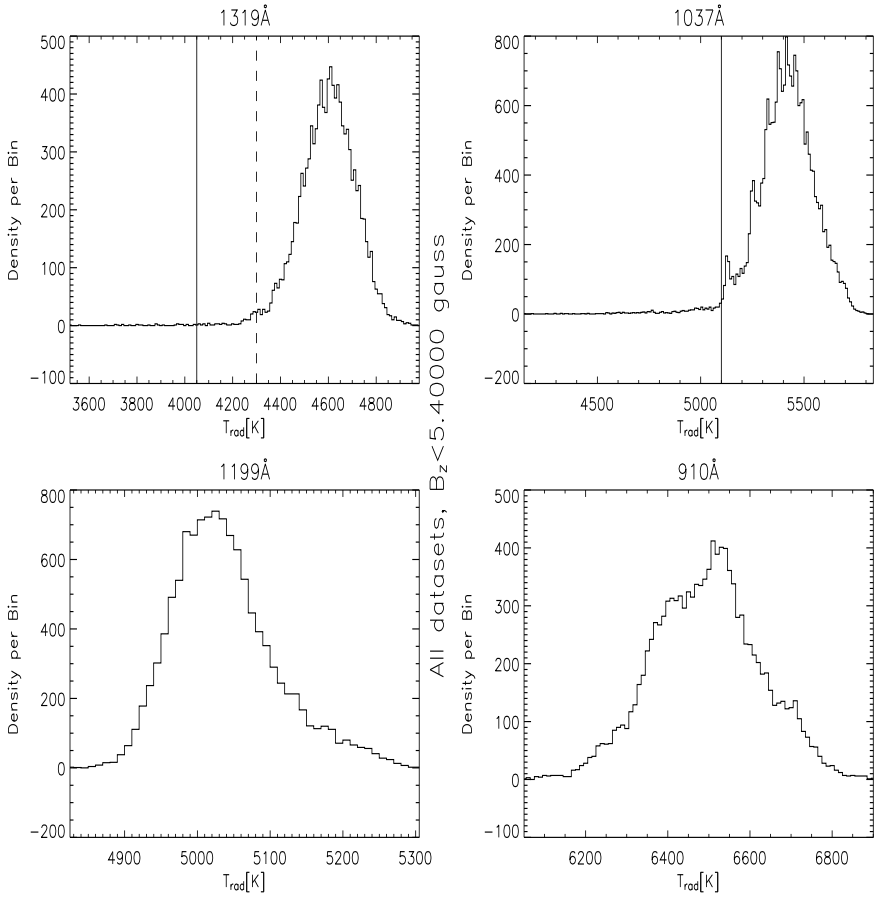

Figure 5.2: **Histogram plots of the radiation temperature** where B_z is lower than 5.4G. This is calculated from all the datasets. The vertical lines indicate the lowest detectable radiation temperature with the SUMER detector with the 1.0″ slit. The dotted line in the 1319Å panel is for the 0.3″ slit.

Bogart, R. 2002, SOI Data Sets, http://soi.stanford.edu/sssc/progs/mdi/calib.html [read: 00.06.2002]

Brekke, P. 2002, The Solar EUV Spectrum, http://folk.uio.no/paalb/sumer_atlas.html [read: 00.06.2002]

Carlsson, M. 1986, A Computer Program for Solving Multi-Level Non-LTE Radiative Transfer Problems in Moving or Static Atmospheres, Report No. 33, Uppsala Astronomical Observatory

Carlsson, M. 1999, in Ninth European Meeting on Solar Physics: Magnetic Fields and Solar Processes. Ninth Meeting of the Solar Physics Section of the Joint Astrophysics Division of the European Physical Society (EPS) and of the European Astronomical Society (EAS). Florence, Italy, 12-18 September, 1999. Proceedings published in ESA SP Series (SP-448), ed. A. Wilson.

Carlsson, M. 2002, SUMER reduction software, http://folk.uio.no/matsc/sumer/index.html [read: 00.06.2002]

Carlsson, M., Judge, P. G., Wilhelm, K. 1997, Astrophys. J. Lett., 486, L63

Carlsson, M., Stein, R. F. 1992, Astrophys. J., 397, L59

Carlsson, M., Stein, R. F. 1996, in R. Pallavicini, A. Dupree (eds.), Cool Stars, Stellar Systems and the Sun, Proc. Nineth Cambridge Workshop, Astron. Soc. Pac. Conf. Series 109, p. 119

Carlsson, M., Stein, R. F. 1997, Astrophys. J., 481, 500

Dammasch, I. E. 2001, The SUMER Investigation, Online, http://sohowww.nascom.nasa.gov/descriptions/experiments/sumer/investigation.html [read: 00.08.2001]

Gonzalez, R. C., Woods, R. E. 1993, Digital Image Processing, Addison Wesley

jeneen@quiver.stanford.edu 2001, MDI Science & Proposals, http://soi.stanford.edu/science/ [read: 00.12.2001]

Judge, P. G., Tarbell, T. D., Wilhelm, K. 2001, Astrophys. J., 554, 424

Karlsen, N. 2003, SUMER and MDI analysis, Online, http://folk.uio.no/kkarlsen/personlig/smitools.html [read: 7.1.2003]

Lites, B. W., Rutten, R. J., Kalkofen, W. 1993, Astrophys. J., 414, 345

McIntosh, S. W., Bogdan, T. J., Cally, P. S., Carlsson, M., Hansteen, V. H., Judge, P. G., Lites, B. W., Peter, H., Rosenthal, C. S., Tarbell, T. D. 2001, Astrophys. J., 548, L237

McIntosh, S. W., Judge, P. G. 2001, Astrophys. J., 561, 420

Rutten, R. 1992, The Generation and Transport of Radiation, fourth edition, Sterrekundig Instuut Utrecht, the Netherlands

Rutten, R. 2000, Radiative Transfer in Stellar Atmospheres, 7th edition, lecture notes, online, http://www.astro.uu.nl/~rutten/tmr/ [read: 00.00.2002]

Scherrer, P. H., Bogart, R. S., Bush, R. I., Hoeksema, J. T., Kosovichev, A. G., Schou, J., Rosenberg, W., Springer, L., Tarbell, T. D., Title, A., Wolfson, C. J., Zayer, I., MDI Engineering Team 1995, Solar Phys., 162, 129

Skumanich, A., Smythe, C., Frazier, E. N. 1975, Astrophys. J., 200, 747

Vernazza, J., Avrett, E., Loeser, R. 1981, Astrophys. J. Suppl. Ser., 45, 635

Wilhelm, K., Curdt, W., Schuehle, E. M. U., Lemaire, P., Gabriel, A. H., Vial, J. C., Grewing, M., Huber, M. C. E., Jordan, S. D., Poland, A. I., Thomas, R. J., Kühne, M., Timothy, J. G., Hassler, D. M., Siegmund, O. H. W. 1995, Solar Phys., 162, 189

ypop@mithra.physics.montana.edu 2002, YPOP Solar Classroom: A Slow Means of Energy Transport, Online, `http://solar.physics.montana.edu/YPOP/Spotlight/SunInfo/Radzone.html` [read: 00.11.2002]